Effect of urban development on local albedo

A Study based on LiDAR data

Shreedatta Marathe

Delft University of Technology

TU Delft

Effect of urban development on local albedo

A Study based on LiDAR data

by

Shreedatta Marathe

to obtain the degree of Master of Science
in Sustainable Energy Technology at the Delft University of Technology,
to be defended publicly on Wednesday, 31 August, 2022 at 9:30 AM.

Student number:	5359627	
Project duration:	December 1, 2021 to August 31, 2022	
Thesis committee:	Prof. Dr. O. Isabella	TU Delft, Head of the PVMD group
	Dr. H. Ziar	Assistant Professor, PVMD Group (Main supervisor)
	Dr. S. de Roode	Assistant Professor (Civil Engineering and Geosciences)
	Ir. Y. Zhou	TU Delft, Daily supervisor

TU Delft

Preface

This report is written for the accomplishment of Master's thesis project under MSc Sustainable Energy Technology under Electrical Engineering, Mathematics and Computer Science Department at Delft University of Technology. The project will be defended in front of a defence committee with Prof. dr.ir. Olindo Isabella (Head, PVMD Group), Dr. Hesan Ziar (Main Supervisor) and Dr. Stephan de Roode (External committee member: Geosciences and Remote Sensing). The work was done under the guidance of Ir. Yilong Zhou as the daily supervisor and Dr. Hesan Ziar as the main supervisor for the project.

The objective of the project was to understand how the urban albedo has been affected throughout the course of modern urban development. The municipality of Delft, The Netherlands, was chosen as the location of the case study. The report delves deeper into implementing a comprehensive albedo model called the Geometric Spectral Albedo (GSA) model developed preceding this project. The reader is expected to know the working physics behind technical nomenclature related to spectral reflectance, solar irradiance, photovoltaic effect, optics etc. Hence the report only focuses on their contribution in the albedo model and does not go beyond their definitions. The study is based on open source Light Detection and Ranging (LiDAR) data available on open source platform by the Dutch government called Actueel Hoogtebestand Nederland (AHN).

The achieved work is also a part of the collective research knowledge base of the professors, researchers and my peers at the Photo-Voltaic Materials Department (PVMD) in the faculty of Electrical Engineering, Mathematics and Computer Science Department at Delft University of Technology.

Shreedatta Marathe
Delft, 31 August 2022.

Acknowledgement

After working and studying from home for the first year of my master's course, I was very excited to work on campus with my peers and colleagues in the PVMD group. This thesis project allowed me to improve my knowledge base and skills. I would be remiss if I didn't acknowledge the constant support and motivation I have received from the people around me.

Firstly, I wish to thank my daily supervisor, Ir.Yilong Zhou, who brought me on-board this project. Yilong was always available to solve my doubts, explain concepts and help me with coding. He always appreciated my efforts and motivated me when the situation seemed dire. I would also like to thank my primary supervisor Dr.Hesan Ziar to whom I owe a great deal for his guidance and motivation throughout the duration of this project. Hesan always gave me highly nuanced advice about improving my work. My special thanks to Yilong and Hesan for creating a supportive and jolly work environment. I would also like to thank Prof.Dr.Olindo Isabella (Head, PVMD Group) and Dr.Stephan de Roode for taking time out of their schedule to attend my defence as thesis committee members.

My peers and colleagues at the PVMD research group also showed continued support and valuable feedback during all the group meetings. I want to extend my utmost gratitude to my friends in Delft and India for their companionship, which got me through all the ups and downs. Finally, none of this would be possible if not for the efforts and wishes of my family. I am eternally grateful to all these people who have impacted my life!

Summary

Changes in social, cultural, and economic paradigms have resulted in a collective shift from rural to urban areas over the last few decades. Cities are expanding to accommodate the ever-increasing population influx in urban areas. New buildings, roads, airports, and harbours are only a tiny part of urban development. It also includes the use of new agricultural lands and changes to water resources surrounding urban areas. These new developments invariably introduce complex geometry into surfaces and a plethora of new materials into the mix, which leads to the change in local albedo. Albedo indicates how well a surface reflects incident solar irradiation, and it is defined as the ratio of total reflected irradiation from a surface to total incident irradiation on the surface. Albedo has a wide range of applications, such as estimating the total heat content of an area and assessing the global warming potential.

The objective of this project was to study the effect of urban development on local albedo using open-source LiDAR data collected in the Netherlands over 25 years. This was accomplished by developing a functional MATLAB platform based on the Geometric Spectral Albedo Model (GSA) to generate gridded albedomaps over the area encompassing Delft. GSA is a comprehensive albedo model that considers influencing factors like geometry of the area, reflectance of material and the incident irradiation. After calculating every influencing factor, the platform calculates albedo and plots a gridded albedomap over the area encompassing Delft. After analysis of the results, it was found that the roughness of the urban fabric is an indicator of its local albedo, where higher roughness indicates lower albedo. The range of albedo values is influenced by the range of reflectance values. On the other hand, it can also be inferred that the variation pattern of albedo is influenced by the geometry of the area. As incident irradiation influences the albedo and the reflectance of materials, it contributes to both the range of albedo values and its variation pattern. Results indicate that change in albedo for Delft was a holistic combination of change in geometry and reflectance values.

The platform has a spatial resolution of $1250\ m \times 1250\ m$, a temporal resolution of 1 hour and temporal coverage of 1 day per month. Modifications like automatic material allocation, a working variable albedometer height algorithm and improved processing speed with parallel computing can enhance the platform's overall performance. This platform can be scaled-up to map albedo for the Netherlands, and it has the potential to guide urban developers in strategic urban planning

List of Figures

List of Tables

Contents

1

Introduction

In the last few decades, a social, cultural and economic shift in moving from rural to urban areas was observed among the collective. According to an annual study at the United Nations Conference for Trade and Development (UNCTAD) in 2021, the world population went from 5.3 billion 30 years ago to 7.8 billion today [1]. On a global scale, upwards of 50% of the population resides in urban environments like cities and towns. In the developed and high-income nations like Western Europe, Japan, North America, Australia and the Middle-east this ratio is more than 80 % of the population [2]. To meet the growing urban population, towns are merging to become cities, while smaller cities are growing in size. Urban areas are also expanding in the vertical domain where towers, sky-scrappers and other such mega structures are signatures of modern cities. Despite this rapid expansion, however, urban areas are still considerably dense, as the 'built-up area' in the world only occupies about 1% of the total global land area available [2].

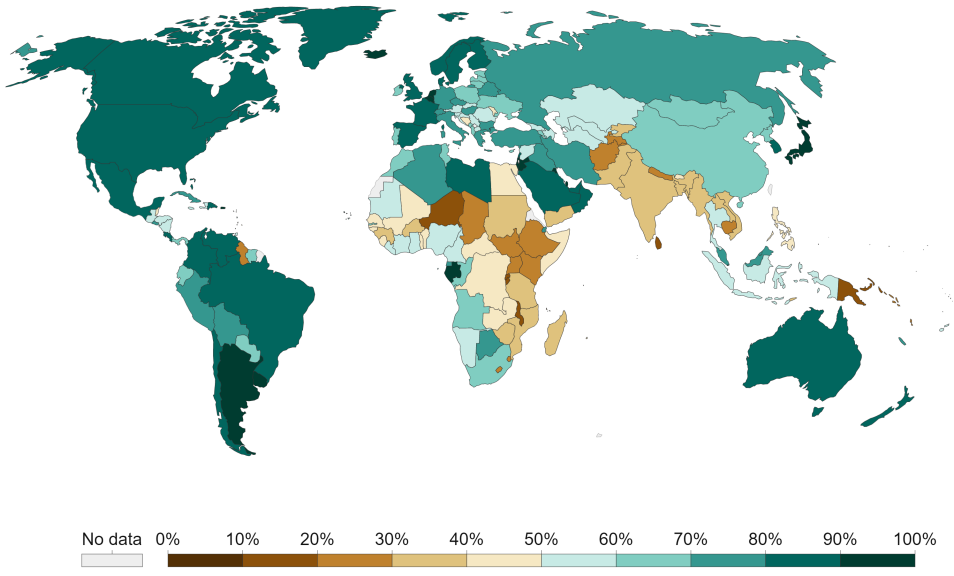

Figure 1.1: A color map of ratio of population living in urban areas for different countries around the world. The statistics considers national standards for what constitutes an urban area [2].

Vertical growth of the urban infrastructure is convenient in terms of managing transport and logistics. With taller structures, everything can be brought closer to reduce the use of longer transport and ease in managing a smaller area. Figure 1.2 depicts the incredible change in Dubai's skyline which took place in the past two decades.

Figure 1.2: Comparative photograph depicting change in Dubai's skyline from the year 2000 (Top) to 2021 (Bottom) [3]

The horizontal expansion of cities is also inevitable. Figure 1.3 shows the growth in the metropolitan areas of New Delhi from December 5, 1989 (left) to June 5, 2018 (right). Although most developments were seen in the outskirts and suburbs of New Delhi, the geographic area has grown nearly twice from 1991 to 2011 [4].

Modern cities are like economic engines that run our world and, while doing so, consume about 75% of the global energy demand. Carbon-intensive urban activities such as transport and energy generation, and manufacturing are responsible for about 75% of total global CO_2 emissions [6]. Global Gridded Model of Carbon Footprints (GGMCF) is a database of carbon footprint on an absolute and per capita basis across 189 countries with high spatial resolution. Only about 100 highly dense and

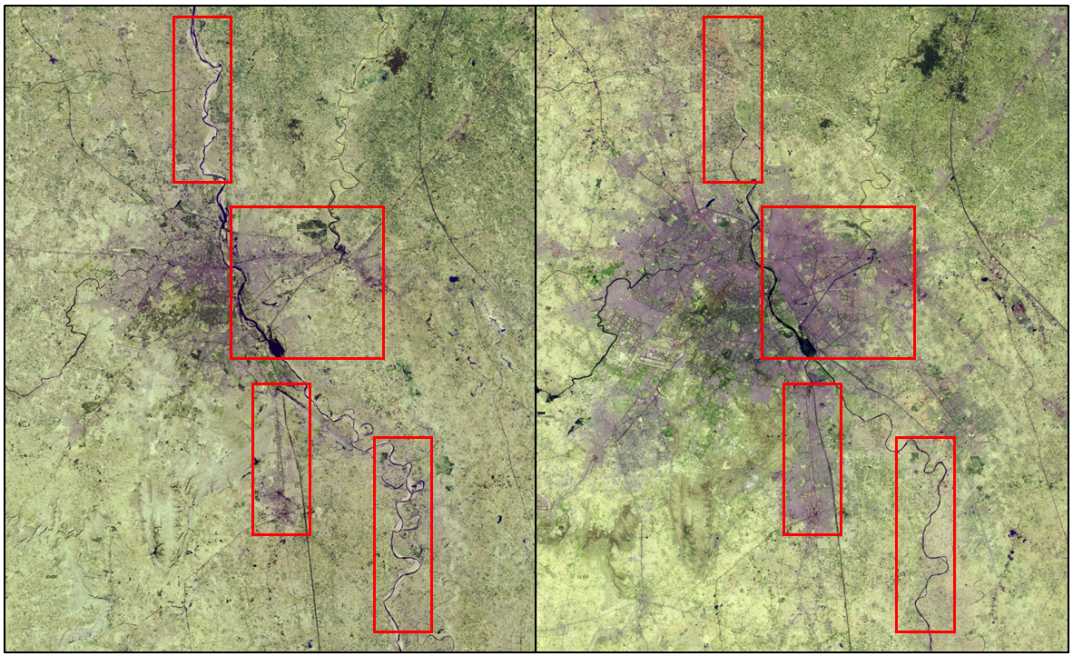

Figure 1.3: Comparative photograph depicting urban growth for the metropolitan area of New Delhi from December 5, 1989 (left) to June 5, 2018 (right) [5]

economically affluent cities and suburbs are responsible for about 18% of the global emissions [7]. Apart from the active contribution towards global emissions and ultimately to climate change, modern urbanscapes also passively contribute to global warming.

With the increase in urban development and expansion, more man-made structures are being added to the existing urban area. If multiple tall structures such as towers, sky-crappers etc., are present in a considerably dense urban neighbourhood, they induce complexity in the urban fabric and create complex shading patterns. An increase in atmospheric CO_2 concentrations in an area can result in a higher global warming potential of that area. A similar effect can be observed if an area only reflects a small fraction of irradiation incident on it. The amount of irradiation that is not reflected from a surface is absorbed and converted to heat. If more the Earth's surface absorbs more irradiation than it reflects back, it experiences positive radiative forcing. As the urban morphology becomes 'rougher' with the addition of new structures, incident irradiation during the day is effectively trapped in the area, causing a heat islanding effect. Authors in [8] found that the local temperatures of developed parts of Delhi are $7 - 9^oC$ warmer in winters than the undeveloped areas. Therefore, monitoring the amount of reflected irradiation from a surface is especially significant in the strategic planning of modern urban areas, which includes encouraging residents to visit and move to urban areas, improving their overall quality of life & the habitability of urban areas.

1.1. Project Objectives

The primary objective of this project is to study the effect of urban development on local albedo using open-source LiDAR data collected over the span of 25 years in the Netherlands. Delft was chosen as the location of case study as this work comes under the umbrella of collective research under the PVMD research group at Technical University of Delft. One of the central objectives of this project is to develop a functional MATLAB platform based on an analytical albedo model. If the performance of this platform for albedo estimation of Delft is valid and credible, the platform can be used for analysis throughout the Netherlands and eventually the world.

As the central objective is far too complex and involves multiple variables simultaneously, it is logical to divide them into smaller parts. This ensures individual attention towards each of the factors influencing the system. Thus, the research objectives for this project are expressed as follows:

1. *Which model should be used to calculate albedo of the selected area?*

- What is albedo?
- What are the applications of albedo?
- What parameters influence the change in the albedo values?
- What is the influence of change in albedo?
- What are the advantages and disadvantages of current methods of albedo estimation?
- What is the significance of the change in albedo values?
- What are the limitations of using a Geometric Spectral Albedo (GSA) model for this analysis?

2. *How are urban areas represented and compared?*
    - Which data can be used to track urban development throughout its course?
    - Which parameter can be used as a metric to quantify urban morphology?
    - What are the characteristic features of modern urban areas?
3. *How to acquire and process the input data for this analysis?*
    - How can the LiDAR data for Delft be retrieved and modified for analysis?
    - How to retrieve the meteorological data for Delft?
    - How to identify materials of different surfaces in an area?
    - What is the spatial resolution and temporal coverage of this input data?
    - How to retrieve reflectivity data of different materials in the area?
4. *How to develop the methodology for urban albedo estimation?*
    - How to calculate individual parameters included in the GSA model?
    - How to simplify view factor algebra for this analysis?
    - How to identify illuminated and shaded parts in the area?
    - How to combine individually calculated parameters to calculate albedo?
5. *How to compare albedo results of an area through different phases of development?*
    - What is the relation between the albedo and the metric for quantifying urban morphology?
    - Does this metric affect albedo alone or in conjunction with other parameters?
    - Was this a correct and fair metric for quantifying the urban morphology and comparing albedo values?

1.2. Overview

The report will be broken down into the following chapters: In chapter 2, we will define albedo and its significance in various applications. Numerous methods and models for albedo calculation are also discussed, including their effectiveness and shortcomings; In chapter 3, we will dive deeper and learn about the GSA model developed in the PVMD group. Development of the model and the influencing factors to determine albedo are also discussed; chapter 5 outlines how the Geometric spectral albedo model is implemented into a functional MATLAB program.

In chapter 6, the constraint imposed on the algorithm and the platform and the techniques used for optimising the performance of the platform will be discussed; In chapter 7, simulation results will be discussed, and salient observations will be noted; In chapter 8 further improvements to the methodology, MATLAB platform, results derived from simulations will be suggested; Finally, in chapter 9, important conclusions will be drawn based on the results obtained from the simulations.

2

Background

Albedo (α), a unitless quantity, is the ratio of the total irradiation reflected from the surface to the total irradiation incident on the ground surface. It is measured by an albedometer depicted in Figure 2.1, which consists of two parameters mounted back to back. Albedo can be expressed as:

$$\alpha = \frac{\phi_{up}}{\phi_{down}} \tag{2.1}$$

Where ϕ_{down} and ϕ_{up} are the total radiant flux incident on and reflected from the ground's surface, respectively. Albedo value has a range of 0 to 1, where 0 value represents perfect black-body absorption, and 1 value represents total reflection.

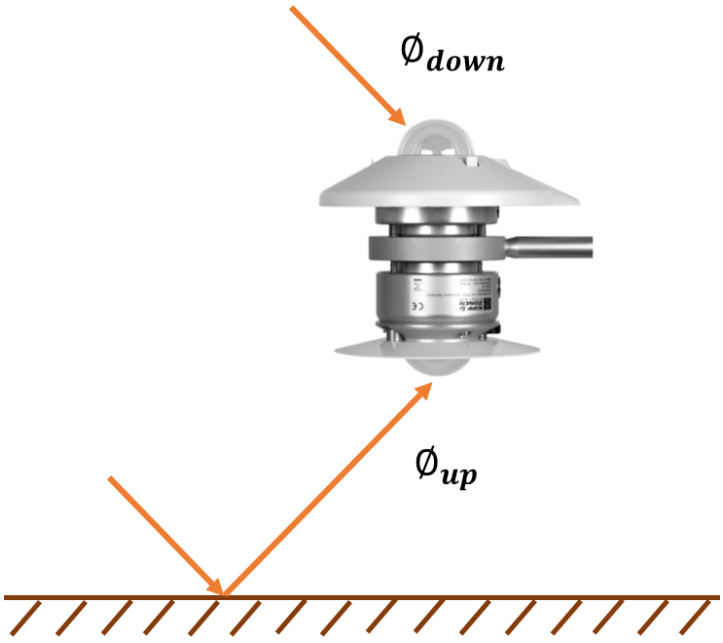

Figure 2.1: Albedometer measurement setup depicts an albedometer manufactured by Kipp and Zonnen b.v. [9]

During albedo measurement, the albedometer is usually mounted 1.5-2 meters above the ground surface [10]. The average albedo of various natural surfaces is shown in Table 2.1. Albedo is observed to be highest near polar regions with extensive snow cover, followed by regions with vast deserts as sand also has higher albedo. The least albedo is observed in tropical regions and open oceans. From Figure 2.3, it can also be observed that in Winters, albedo values are generally higher than albedo values in summer. Interestingly, as the polar ice cap near Antarctica melts in summer, the overall

albedo of the region reduces during summer. The same is true for polar ice caps in the Arctic region during the winters. An average albedo of 0.29 can also be assigned to the Earth's surface which is called global albedo or planetary albedo [11]. Black-sky albedo is defined as the albedo when only direct irradiation is considered. Thus, it is also called directional hemispherical albedo. White-sky albedo, on the other hand, is calculated assuming only diffuse component of sunlight and is also called bi-hemispherical albedo. Diffuse irradiation is assumed to be isotropic. In reality, apparent surface albedo is interpolated between pure black-sky and white-sky albedo values as some function of the fraction of diffuse irradiation [12, 13].

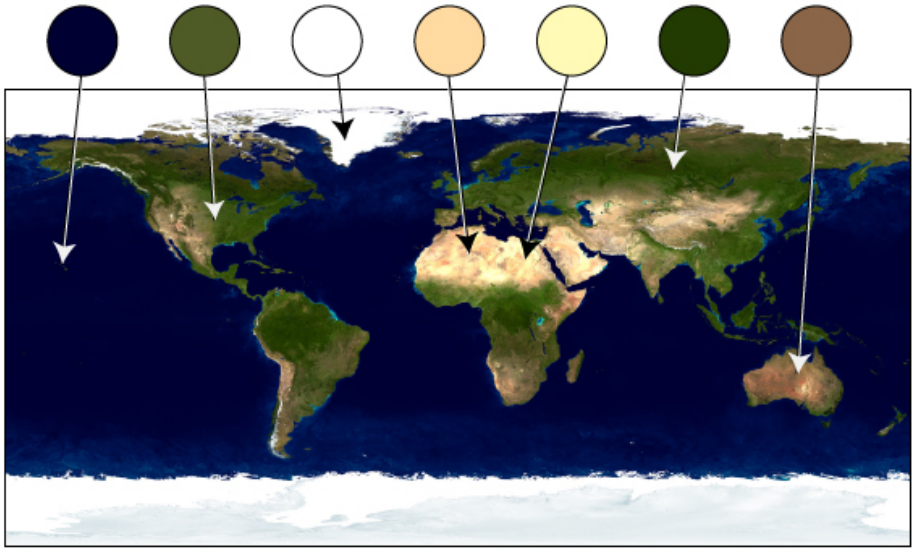

Figure 2.2: A depiction of different colours of Earth's surface. They are the results of the unique geographical and topographical features of these environments. As a convention, darker areas have lower albedo values, and lighter areas have higher albedo values. [14]

Surface	Range of Albedo
Fresh Snow	0.80 to 0.90
Old/Melting Snow	0.40 to 0.80
Desert Sand	0.40
Grassland	0.25
Deciduous Trees	0.15 to 0.18
Coniferous Forest	0.08 to 0.15
Tundra	0.2
Ocean	0.07 to 0.10
Fresh Asphalt	0.04
Bare Soil	0.17
Fresh Concrete	0.55

Table 2.1: Albedo range for different naturally occurring and man-made surfaces [15]. Albedo values for represented in the table are consistent with Figure 2.2 and Figure 2.3

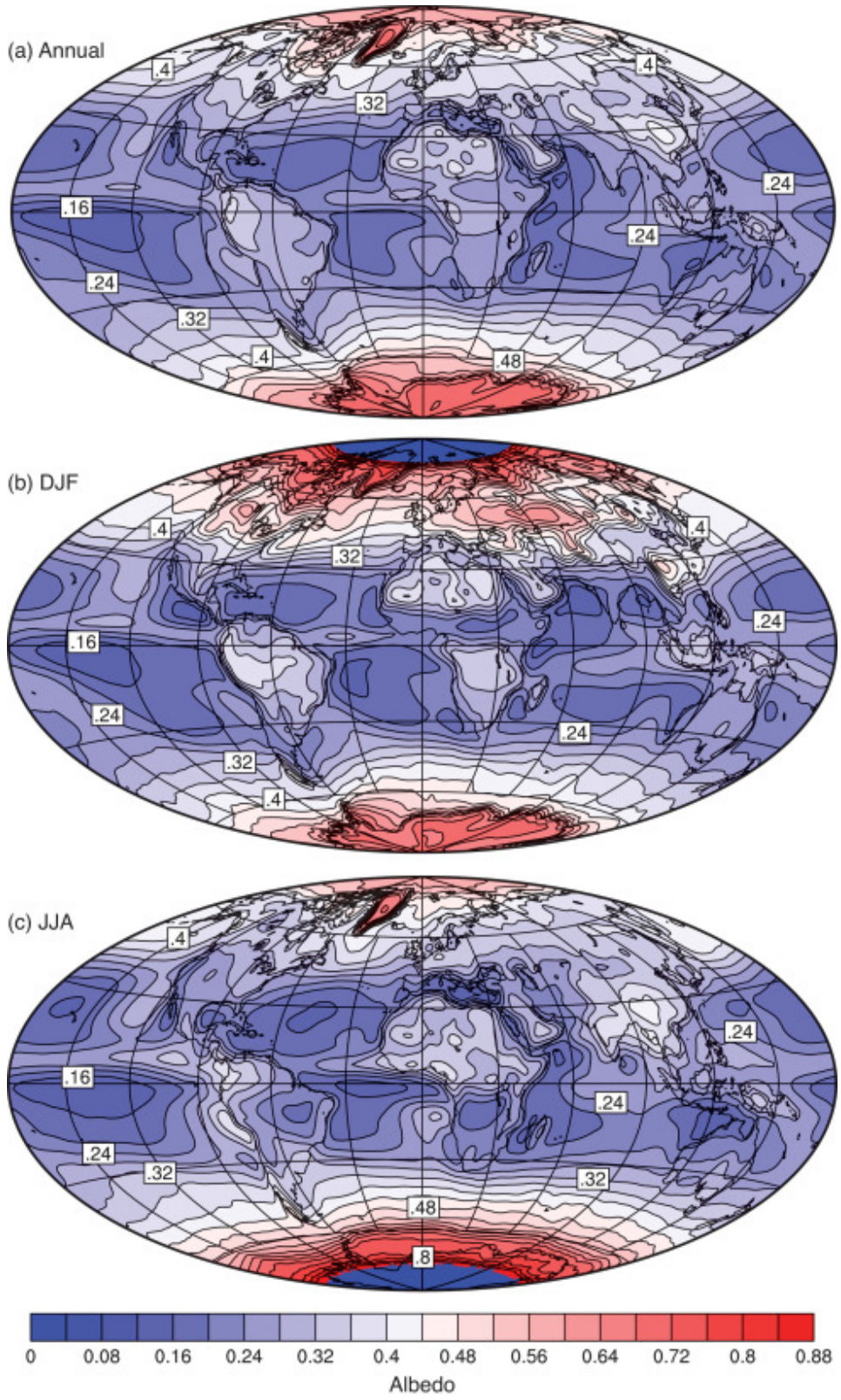

Figure 2.3: Average broad spectrum global albedo map (a) Annual (b) Winter (c) Summer. Data is taken from CERES 2000-2013 and published in [11]

2.1. Changes in albedo values

Since the local albedo of an area is the ratio of total reflected irradiation to the total incident irradiation, any factor that influences the reflected irradiation can influence albedo. The local albedo of an area is highly dynamic and depends broadly on solar irradiation, the reflectivity of materials and the geometrical arrangement of surfaces in the surrounding.

The amount of solar irradiation incident by the Earth's surface depends on the solar position and sky conditions. Changes in solar position and sky conditions change influence the amount of direct normal and diffuse solar irradiation incident on the surface. Sky conditions vary throughout the year. In the monsoon or fall, the sky is usually overcast and cloudy, whereas, in the spring and summer, the sky is usually clear with few clouds. The sky conditions also change throughout the day. Similarly, solar position varies throughout the day and throughout the year. During dawn and dusk, for example, solar altitude is lower compared to the solar position at noon. Authors Hartman et.al. also deduced a relation between average albedo values of a location and latitude of the location [11] which is depicted in Figure 2.4. It can be observed that albedo values are higher for higher latitude locations. As solar altitudes for high latitude locations are generally lower, we can infer that average albedo values are higher for lower solar altitudes.

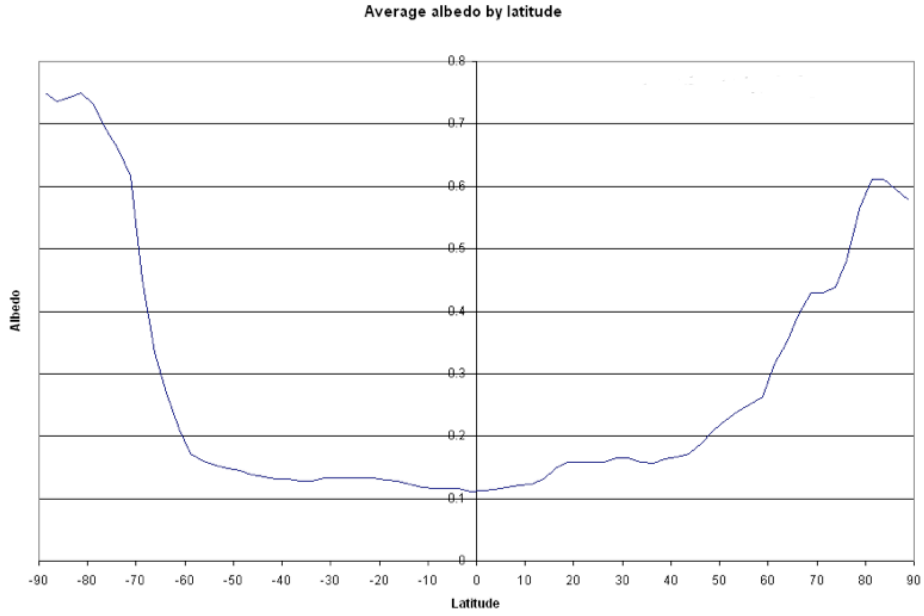

Figure 2.4: Average broad spectrum global albedo vs. Latitude [15]

The presence of different materials in the surroundings influences the reflection of light from these surfaces. As reflectivity of materials varies with the wavelength of the incident light, albedo also has spectral dependence. Figure 2.5 shows the spectral reflectivity variation of alfisol soil. Materials of surfaces sometimes change periodically. This is especially true for natural surfaces where a full cover of green leaves can be observed on vegetation in Spring and Summer. This is contrasted by the dark-coloured leaves (often red, ochre and orange) or lack thereof in Autumn. Snow-covered surfaces in winter and water-covered surfaces in monsoon are a few more examples of such an effect.

The surface roughness and the complex arrangement of surfaces in the surrounding also has an impact on albedo. This takes into account both macroscopic and microscopic roughness of surfaces. One example is the rapidly changing urban morphology of modern cities. As discussed before, the 'roughness' of the urban fabric effectively traps heat and creates localised heat islands. Apart from that, changes in natural resources due to deforestation, reduction in water resources, and use of land for agriculture also change the geometry of the location.

The aforementioned factors have the potential to affect the albedo values individually. However, in practice, change in albedo is a cumulative effect of change in multiple parameters. As albedo is affected by parameters that change with both space and time, long-term albedo monitoring is a chal-

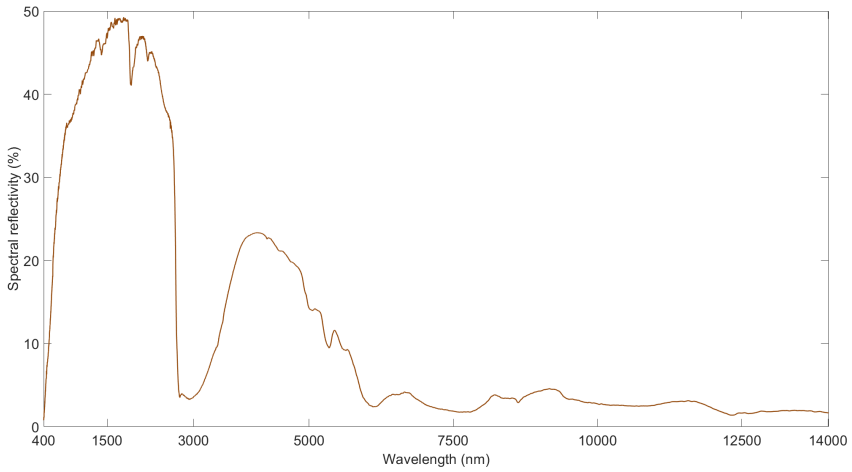

Figure 2.5: Spectral reflectivity in (%) vs the wavelength (nm) for 'alfisol' soil

lenging process. It is infeasible to implement long-term physical albedo measurements for any given location due to the unavailability of measurement equipment and the excessive time and manual efforts needed. Apart from that, it is also infeasible to physically measure albedo everywhere for a longer duration as the same physical set-up needs to be maintained for an extended duration. Additionally, local albedo measurement with instruments is difficult at places like water bodies, steeply sloped surfaces and outright impossible on many naturally inaccessible places such as tree tops, mountain peaks etc.

2.2. Applications of albedo

Albedo value calculated for an area can be used for a plethora of applications which include estimating the global warming potential of the area, PV system yield calculation, agriculture etc.

As discussed before, albedo is indicative of the heat content of the area. In 2010, authors Akbari et.al. simulated an increase in albedo by 0.1 of all urban areas and found the global temperature would reduce by 0.01 to 0.07 K [16]. Climate Data Information, a climate change data service, indicate that if forests in the northern region have snow cover, their albedo is higher compared to a bare forest canopy. An average albedo reduction of 0.017 due to the loss of snow cover in these forests can lead to a local temperature increase of about $3.8^{o}C$. Long-term broadband albedo estimation of an urban area can be linked with its global warming potential. Researchers in [17] showed that an albedo increase of 0.1 for all urban areas is equivalent to offsetting 44 Gt of CO_2 emissions. Authors also mention that increase in albedo of rooftops can lower energy consumption for cooling of urban areas significantly. Global Warming Potential (GWP) of different products in the measure of global warming caused by that product throughout its life-cycle compared with the global warming caused by 1 ton of CO_2 emissions. Authors in [18] found that increase in albedo due to using a reflective plastic cover over greenhouses resulted in a reduction in GWP of per ton of tomatoes from 303 kg to 108 kg $CO_2\,eq$.

Albedo is also very crucial for agriculture. A study in [19] showed that albedo is closely linked to the average water content of the soil. Using the surface energy balance equation [20], the author in [21] established a relation between the temperature coefficient of soil with the roughness of the soil. The author also proposed the use of such temperature models to ensure the optimum conditions of soil for cultivation. Since heat is the basis of many of the biochemical reactions common in nature, local albedo is also linked with the germination time of seeds, growth cycle of crops etc.

PV yield calculation involves the use of albedo as well. Incident solar irradiation is divided into direct, diffuse and reflected components. The reflected component of irradiance is expressed as:

$$G^{albedo} = GHI \times \alpha \times (1 - SVF) \tag{2.2}$$

where Global Horizontal Irradiance is denoted by GHI, albedo by α and the Sky View Factor by SVF of the area [22]. Authors in [21] indicate that macroscopic change in the roughness of the area,

such as with PV installation, inevitably changes the geometry of the surrounding surfaces and causes a drop in albedo. Authors found that introduction of a single LG Neon2 bifacial PV module in Amsterdam resulted in a drop in albedo by 3.6%, which resulted in a drop in actual PV yield. Evidently, accurate albedo estimation is also important for accurate PV yield estimation, especially with the Bifacial PV and Building integrated PV systems gaining considerable mainstream appeal.

Apart from this, albedo is used for remote sensing and guiding satellite platforms for Earth observations and in computer graphics and animation for rendering rough surfaces.

2.3. Satellite data based albedo estimation

2.3.1. Copernicus

Copernicus is an observatory monitoring Earth using a collection of satellite and ground-situated measurement platforms on behalf of the European Union. It provides a dataset for global surface albedo with a temporal resolution of 10 days. The spatial resolution of this dataset can vary from $1/30^o (\approx 4km)$ to $1/336^o (\approx 300m)$, depending on the measurement platforms used. The output dataset includes Spectral Directional Surface Albedo (SDSA) and Spectral Hemispherical Surface Albedo (SHSA) which compute albedo as a function of wavelength. The former only considers direct component while the later considers only diffuse component of sunlight. By integrating the spectral albedo over different wavelength bands, Broadband Directional Surface Albedo (BDSA) and Broadband Hemispherical Surface Albedo (BHSA) can be obtained. Currently, three spectral bands are available, namely, visible band (400 nm to 700 nm), near infra-red (NIR) (700 nm to 4000 nm) and broadband spectrum (400 nm to 4000nm). The data is available for download on the official website of Copernicus Climate Change Service [23].

2.3.2. Tropospheric Emission Monitoring Internet Service (TEMIS)

TEMIS is a platform associated with the European Space Agency (ESA) that also provides surface albedo climatological databases. These databases are computed as Lambertian Equivalent Reflectivity (LER) for wavelengths ranging from UV to near infrared band. Lambertian reflectance model assumes perfect diffuse surface that reflects irradiation equally in all directions. These databases have varied spatial and spectral resolution as well as wide temporal coverage. They are available for download on the official website of TEMIS [24]. Authors in [25] introduced and compared the two new LER databases computed on Global Ozone Monitoring Experiment(GOME-2) and Scanning Imaging Absorption Spectrometer for Atmospheric Cartography (SCIAMACHY) instruments. These two databases have improved spatial and spectral resolution than some of the previous databases. The two databases are created on a monthly interval with spatial resolution of $1^o\ Lat \times 1^o\ Lon$ In real life scenarios, assumption of lambertian reflectance can not be justified on most occasions. Therefore authors have also suggested including viewing angle dependence of LER in the database will enable the database to capture a more realistic dependence of LER on geometry. Since then, resolution of GOME-2 LER has improved significantly from $1^o\ Lat \times 1^o\ Lon$ to $0.25^o\ Lat \times 0.25^o\ Lon$ with highest resolution available for coastlines, snow covered areas and deserts [24]. Most recently launched instrument platform called TROPOspheric Monitoring Instrument (TROPOMI) instrument database has even higher resolution of $0.125^o\ Lat \times 0.125^o\ Lon$ [24].

2.3.3. Moderate-Resolution Imaging Spectroradiometer (MODIS)

MODIS and Multiangle Imaging Spectroradiometer (MISR) are two research projects ongoing at University of Massachusetts, Boston. MODIS albedo product database is available for download on the official web-page of NASA Earth Observations (NEO) [26]. The albedo product offered gives an albedo map of a 16-day top-of-atmosphere (TOA) reflectance data with a spatial resolution of $1\ km \times 1\ km$ grid. It includes both white-sky and black sky spectral albedo for visible band, near-infrared band and short wave broadband (0.3-0.7 µm, 0.7-5.0 µm, and 0.3-5.0 µm respectively). Total reflected irradiance from Earth's surface is then calculated considering the short wave broadband domain (0.3-5.0 µm). Qu Y., et al developed an algorithm to establish relationship with top-of-atmosphere (TOA) reflectances and land surface broadband albedos using angular bin regression method [27]. Results showed that the land surface albedo values calculated by their algorithm are consistent with the standard MODIS alebdo

product. This allowed the authors to map daily land surface albedos using one single set of MODIS data and mapping rapidly changing albedo with improved temporal coverage. Liang S. et.al. proposed another algorithm to retrieve land surface broadband albedo from top-of-atmosphere (TOA) narrowband albedos available from MODIS albedo product using a neural network [28]. Narrowband albedo refers to three spectral bands are available, namely, visible, near infra-red and shortwave spectrum. Authors have defined three TOA albedos which are independent of atmospheric conditions. Since total shortwave broadband (land surface) albedo values are significantly different than the TOA shortwave albedos, authors have proposed two methods of retrieving land surface albedos from TOA narrowband albedo from satellite based albedo products. One of the methods being linear relation between the two and the other method is establishing a relation using polynomial regression of a neural network. Because of the unavailability of sufficient information for the visible band in MODIS / MISR database, authors have reported difficulty in retrieving the broadband visible albedo.

Although satellite data based albedo estimation methods bypass the complexities of physical measurement and inaccuracy induced due to simpler albedo models, the albedo products offered by these platforms are top-of-atmosphere or black-sky spectral albedo values. However, apparent broadband surface albedo values, which are needed for most practical purposes, are interpolated between pure black-sky and white-sky albedos. Moreover, without correct regression methods, albedo values retrieved from satellite based methods can not be reliably used as the apparent broadband surface albedo. Apart from that, most albedo products offered do not have enough spatial resolution (limited to $\approx$ km) or temporal coverage (limited to $\approx$ days a month). Due to highly dynamic nature of atmospheric conditions, broadband surface albedo under one atmospheric condition might not well suited for other conditions.

2.4. Existing numerical albedo models

Similar to satellite based albedo estimation, numerical albedo models also receive specialised input data to retrieve albedo. Some of these models are very rudimentary like the Isotropic Albedo Model, while others are fairly complex and intricate.

2.4.1. isotropic constant albedo model

One of the simplest albedo models is the isotropic constant albedo model proposed by authors in [29]. Here, the ground albedo is assumed to be at a constant value of 0.2 for ground free of snow. This is a generally accepted practice when actual measurement is not feasible or available. Authors in [30, 31], however, found the isotropic albedo value of 0.2 to be too high for the city of Athens, Greece and Geneva, Switzerland. In a study on investigating the impact of ground albedo on PV systems [32], authors state that when considering the constant albedo value of 0.2 can lead to underestimation in ground reflected irradiance by more than 31%.

Authors in [33] suggested that constant albedo assumption based on isotropic reflection assumption should be replaced by a constant mean albedo value specific to the geographical location. This approach is satisfactory and suitable on most occasions. However, this indicates that mean albedo values have to be measured for all geo-locations in question. The authors also suggested that introducing anisotropic considerations in the equation will require more site-dependent parameters which would negatively skew the utility to complexity ratio of the approach.

2.4.2. Isotropic seasonal model

This model was first introduced by [34] where the albedo is dependent on the latitude of the location denoted by ϕ. In the proposed equation, albedo can be calculated as:

$$\alpha = \sum_{i=1}^{i=3} a_i \phi^i \tag{2.3}$$

where, the latitude ϕ ranges from 20^o to 30^o and from 30^o to 60^o. The coefficients $a_1, a_2 \& a_3$ of this polynomial albedo equation can be found in [34] as monthly averages. For lower latitude values, the

albedo is essentially function of latitude only and another equation fit is suggested by the authors,

$$\alpha = -0.18 + 0.024\phi - 0.0004\phi^2 \tag{2.4}$$

However, the modelling and data measurement was for the continent of North America for various latitudes. This approach can't encapsulate the complex variations of 'zonal albedo' on a continental scale.

Another model developed implemented in [35] is also based on the isotropic sky assumption. The approach describes reflected solar radiation as a function of global solar radiation incident on the horizontal surface and the surface albedo. This relation is expressed as:

$$E_{rs} = E_g \alpha_s (1 - \cos\alpha) \tag{2.5}$$

where, E_g is the combination of direct and diffuse radiation, α_s is the surface albedo and α is the slope of the surface. Sandia National Laboratories (SNL) has also developed a transposition model which was obtained by curve fitting on empirical data from Albuquerque, New Mexico [36]. the equation is expressed as:

$$\alpha = 0.012\theta_z - 0.04 \tag{2.6}$$

where, θ_z is the solar zenith angle. Evidently, this relation is valid for a specific geo-location and can not be used globally.

2.4.3. Nkemdirim model

This model was developed by authors in [37] was to determine the effect of solar elevation on the ground albedo values measured for different sky conditions and for land surfaces with different levels irrigation and cultivation. The model was generalized by the authors as follows:

$$\alpha = a \exp b\theta_z \tag{2.7}$$

where, θ_z is the zenith angle of the geo-location and a & b are constants specific to the geo-location. Measurements were taken for four different types of cultivated and irrigated soils and for different times of the day. Suitable standard relations were found using regressions for these four types of soils and for forenoon and afternoon of the day. The findings suggest strong relation between solar elevation angles and albedo. Authors also observed that average albedo variation with zenith angle was not consistent with different sky conditions but the average albedo values in the afternoon period showed similar variations with zenith angles for all sky conditions.

2.4.4. Nearly isotropic reflectance model

This model introduces anisotropic consideration in reflected radiation. Author in [38] introduces two coefficients f_{ab} and f_{af} signifying backward and forward increase of reflectance to indicate anisotropic reflectance. The direct/beam reflectance and diffuse reflectance are expressed as the function of normal reflectance as:

$$\rho_b = \rho_n + F(f_{ab}, f_{af}) G(\alpha) H(h) \rho_d = \rho_n + 0.023(f_{ab} + f_{af}) \tag{2.8}$$

where, ρ_n is the normal reflectance attributed to pure isotropic reflection and $F(f_{ab}, f_{af})$ is the function of the two anisotropic coefficients. Author surmised that the resultant albedo is the combination of direct/beam and the diffuse reflectance. This model is one of the advanced and complex methods of albedo modelling developed and shows merit for various sky conditions and spatial orientations. However, the limitation of this approach is that the coefficients are specific to the chosen location and need to be re-calibrated for other locations.

2.4.5. Temps and Coulson model

Authors in [39] describe the component of radiation incident on any surface as a combination of direct (F_D) and diffuse (F_d) component of radiation and diffuse components of radiation and the surface albedo.

Thus ground surface albedo derived from this relation is:

$$\alpha = A[1 - \cos^2 \frac{\epsilon}{2}] \tag{2.9}$$

where, A is constant albedo co-efficient and ϵ is the angle surface normal makes with solar zenith. Anisotropy is introduced in this equation by adding a correction factor to the equation as:

$$\alpha = A\left[1 - \cos^2(\frac{\epsilon}{2})\right]\left[1 + \sin^2(\frac{Z}{2})\right](|\cos a|) \tag{2.10}$$

where, Z is solar zenith angle and a is the azimuth angle with respect to the sun. Authors have expressed that the applicability of this model for different atmospheric and geographical conditions needs to be studied further.

A comparative study of different albedo models was performed for the city of Athens, Greece. Authors of this study had compared four albedo models like constant albedo assumption, Isotropic Seasonal Model, Nkemdirim Model, Nearly Isotropic Reflectance Model from international publications and four albedo models developed for the city of Athens. Authors found that the 'Nearly Isotropic Reflectance Model' was one of the most sophisticated model and had albedo values most closely matching actually measured albedo values in Athens [31]. Apart from the internationally published albedo models, the models developed by authors also performed just as well as or better than the Nearly Isotropic Reflectance Model. Authors found that two of these models which use geometric mean period analysis performed the best among all scenarios for the area of Athens [31].

Many of the models discussed before rely on the isotropic assumption and horizontal ground assumption. However, the Nearly isotropic reflectance and the Temps & Coulson model are much more intricate and also take into account the inclination of surfaces and anisotropic reflections. These models are also useful for calculating reflected radiation incident on a surface. It is essential to note that most of the literature discussed here have concluded that location specific mean measured albedo values are far more accurate and reliable.

3

Geometric spectral albedo model

Previously, various methods of retrieving albedo from analytical and satellite-based methods were discussed. Their advantages and disadvantages were also discussed. While albedo retrieval from satellite data based methods and analytical methods like nearly isotropic model developed in [38] is arguably more complex and involves more factors that influence the system. Despite of that, these methods provide a more accurate picture of the broadband local albedo. Geometric Spectral Albedo Model (GSA) was developed at PVMD research group, TU Delft [21]. It is one of the newly developed albedo models that considers the influence of factors like geometry of the surfaces, reflectance of surfaces and the irradiance available at that time and location on the local albedo.

3.1. Simplified model

As discussed earlier, albedo is highly dynamic quantity and depends on a lot of parameters. Thus, we begin to build the model with a fundamental case envisioned by the author. A smooth, lambertian surface is assumed to have simple planar geometry as shown in Figure 3.1.

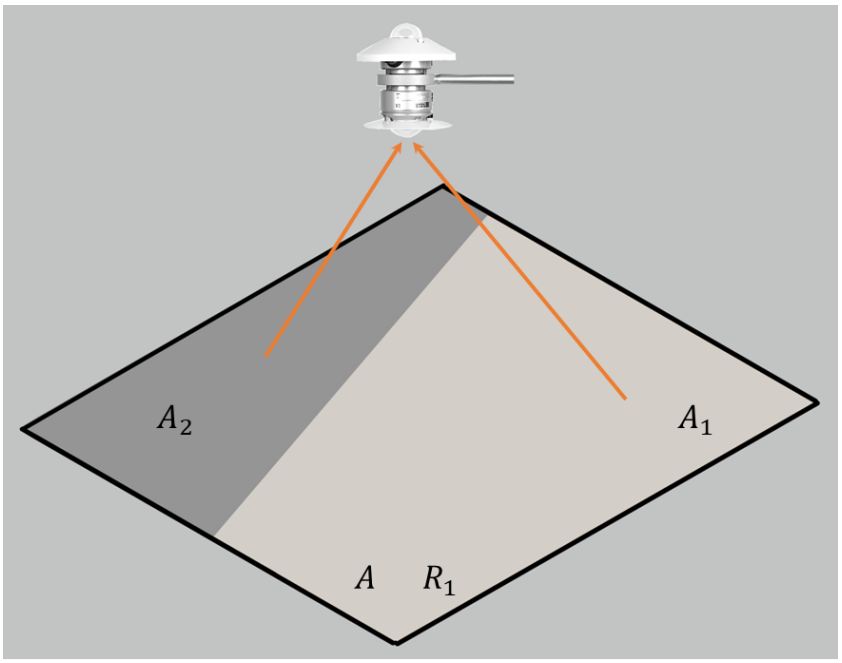

Figure 3.1: Simplified case setup for Geometric Spectral Albedo model developed in [21]. Albedo is to be calculated for area A. A_1 and A_2 are illuminated and shaded parts of area A respectively.

An albedometer is mounted horizontally in the centre of this area A at an height of 1.7 meters.

Surface S denotes the albedometer surface. The surface is assumed to be homogeneous and has only one material. This is analogous to mounting an albedometer at a certain height on an infinitely spread open grass field. Area A is selected such that the albedometer only has area A in its field of view precisely. Now, parts of area A are illuminated by sunlight (A_1) and the remaining parts are shaded (A_2). Area A_1 receives both Direct Normal Irradiance (DNI) and Diffuse Horizontal Irradiance (DHI) while Area A_2 receives only diffuse irradiance (DHI). Thus, albedo for area A can be expressed as:

$$\alpha = R\left(F_{S\to A_1} + \frac{1}{H+1}F_{S\to A_2}\right) \tag{3.1}$$

$$where,\ \ R = \frac{\int R(\lambda)G(\lambda)d\lambda}{\int G(\lambda)d\lambda} \tag{3.2}$$

$$H = \frac{DNI_M}{DHI_m}\cos\theta_M \tag{3.3}$$

In Equation 3.2, R is defined as the reflectance of the surface A, $G(\lambda)$ is the spectral irradiance incident on the surface of area A and $R(\lambda)$ is defined as the spectral reflectivity of the material. Thus, R is essentially irradiance weighted reflectance of the material. $F_{S\to A_1}$ and $F_{S\to A_2}$ are the view factors of area A_1 and A_2 with respect to the albedometer. View factor ($F_{S\to A_1}$) of area A_1 with respect to the albedometer surface (S) is defined as the measure of albedometer's field of view occupied by area A_1. In Equation 3.3, DNI_M and DHI_M (in W/m^2) are the Direct Normal Irradiance and Diffuse Horizontal Irradiance measured at surface M which near the albedometer measurement setup or located at a nearby meteorological station. θ_M is the angle between the surface normal of surface M and the radiant flux incident on surface M. The quantity $1/(H+1)$ in Equation 3.1 is a parameter unique to this albedo model called as the relative shade brightness. On days with higher amount of DNI, such as summer days with clear skies, value of H is higher compared to days with overcast and/or cloudy skies with higher DHI than DNI. Higher values of H indicates lower value of $1/(H+1)$ which indicates that shadows on such days are darker. On days with higher values of $1/(H+1)$, shadows are generally lighter (brighter). This is corroborated by simple observation of shadows on days with clear sky and cloudy sky respectively. A few important observations can be noted for Equation 3.1:

1. Albedo depends on quantities that can be broadly categorized as reflectivity of the material(R), geometry of the surfaces ($F_{S\to A_1}$ & $F_{S\to A_2}$) and solar position and sky conditions ($1/(H+1)$)

2. Both illuminated and shaded parts of area A contribute to the albedo.

3. Albedo variation is subject to both spatial and temporal changes.

4. Albedo of a surface at given location and time is always lower than the reflectance of the material since $(F_{S\to A_1} + F_{S\to A_2}) = 1$ and $0 \le 1/(H+1) \le 1$.

3.2. Complex geometry and rough surfaces

Now, we move from the hypothetical smooth, lambertian and homogeneous surface with simple planar geometry to a real life setting with complex geometry, macroscopic roughness and consisting of many different materials. To begin, assume an area A with N different materials and with shaded and illuminated parts. Such an arrangement is depicted in Figure 3.2. When the surface is assumed to be smooth and homogeneous, it can be assumed that all the illuminated part (A_1) of area A receives both DNI and DHI uniformly. However, the same can not be assumed for rough surfaces with complex geometry. There are parts of the illuminated surface that do not receive direct irradiation but receive diffuse irradiation. This can be due to macroscopic or microscopic variations in the surface, for example, the self shadowing caused on the insides of a crack or a gap in a concrete wall. The concrete wall might receive uniform illumination however, some parts of the surface might still be shaded due to the arrangement of surfaces. Albedo for area A with complex geometry, macroscopic roughness and N different materials is expressed as:

$$\alpha = \sum_{i=1}^{i=N} R_i \left(C_i F_{S \to dA_{i1}} + \frac{1}{H+1} \left(C_i' F_{S \to dA_{i1}} + F_{S \to dA_{i2}} \right) \right) \tag{3.4}$$

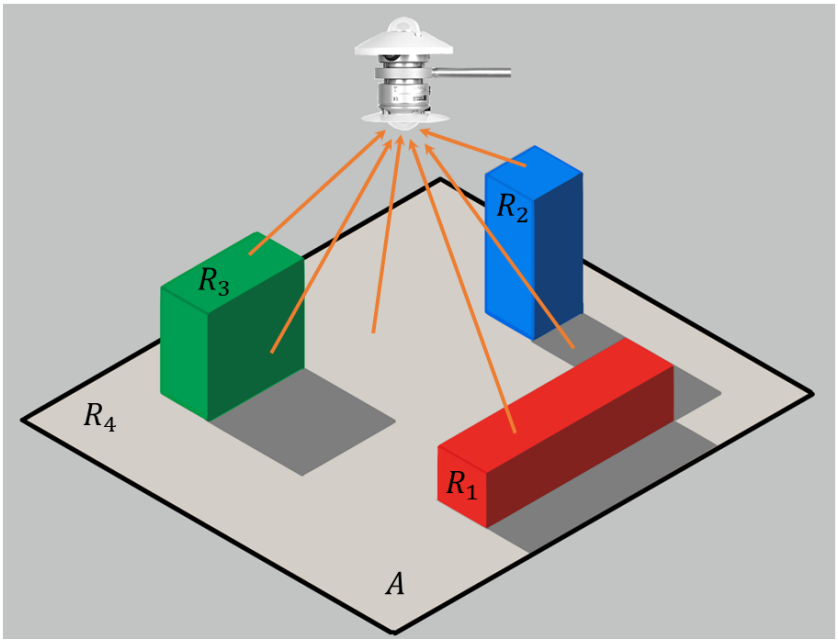

Figure 3.2: Setup envisioned for Geometric Spectral Albedo modelling for complex geometry and rough surfaces [21]. Here, an albedometer views area A. There are four reflective surfaces. R_1,R_2,R_3 are the artifacts situated on ground and R_4 is ground itself. Albedometer views both shaded and illuminated areas of surfaces with different materials

3.2.1. View Factor

To extend the simplified version of the GSA, we first consider a small differential area element located on surface A and analyse its contribution to albedo. Differential area 'dA' is chosen arbitrarily (dA « A). As this area element is very small compared with the area A, we can assume dA to be a homogeneous surface (only one material), either uniformly illuminated or shaded and parallel to the ground located at certain elevation. Apart from that, dA can be visible or not visible from the albedometer. Area element dA can contribute to the albedo if it is illuminated or shaded and visible from albedometer. To compute the total amount of irradiation incident on the albedometer surface which is reflected from area element dA, we have to compute the view factor of dA with respect to surface S. In radiative heat transfer, view factor or shape factor ($F_{A_1 \to A_2}$) is defined as the ratio of total diffuse radiative energy emitted from first area element (A_1) which is received by second area element (A_2) when there are no intermediate reflections [40]. Figure 3.3 depicts the view factor algebra for two surfaces A_1 and A_2.

Authors in [41] express the integral of view factor as:

$$A_2 F_{A_2 \to A_1} = A_1 F_{A_1 \to A_2} = \int_{A_2} \int_{A_1} \frac{\cos\beta_1 \cos\beta_2}{\pi d^2} dA_1 dA_2 \tag{3.5}$$

where β_1 and β_2 are the angles between the line joining centres of two areas and the surface normal of area A_1 and A_2 respectively. Similarly, the view factor for area element dA with respect to albedometer S can be expressed as:

$$SF_{S \to A_1} = A_1 F_{A_1 \to S} = \int_{S} \int_{A_1} \frac{\cos\beta_1 \cos\beta_2}{\pi d^2} dA_1 dS \tag{3.6}$$

3.2.2. Roughness

To avoid unintentional bias towards any particular direction of reflection, the height data of reflective surfaces was assumed to be normally distributed. However, in reality, reflective surfaces in urban areas

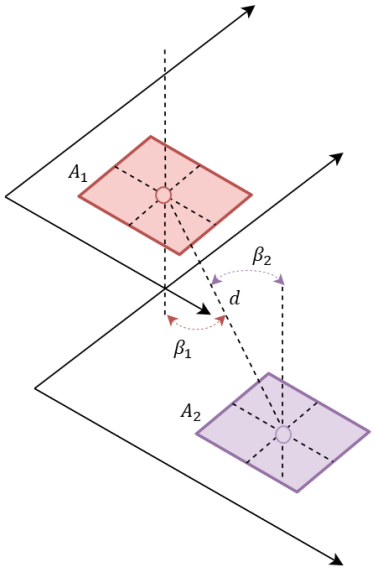

Figure 3.3: View Factor algebra for two parallel planes A_1 and A_2 denoted as $F_{A_1 \to A_2}$

are arranged in complex geometrical arrangements. Also, spatial distribution of high and low elevation points is not really uniform. Thus the distribution of heights with high variations is quantified as the 'roughness' of reflective surfaces. Roughness, in this case, is the root mean square of mean slopes of all the points present in the given area [21]. Authors in [42] define Δ_q as the root mean square of mean slopes and is expressed as:

$$\Delta_q = \sqrt{\frac{1}{n-1}\sum_{i=1}^{n-1}\left(\frac{\delta_{yi}}{\delta_{xi}} - \theta_m\right)^2} \tag{3.7}$$

$$where, \theta_m = \frac{1}{n-1}\sum_{i=1}^{n-1}\left(\frac{y_i - y_{i-1}}{x_i - x_{i-1}}\right) \tag{3.8}$$

The equation for the root mean square of mean slopes expressed before is applicable for a uni-dimensional system. To extend it to a two dimensional system, we can modify Equation 3.7 and Equation 3.8 as follows:

$$\Delta_q = \sqrt{\frac{1}{area(A)^2}\sum_{i=1}^{n-1}\left(\left(\frac{\delta_{zi}}{\delta_{xi}} - \dot{\theta_x}\right)^2 + \left(\frac{\delta_{zi}}{\delta_{yi}} - \dot{\theta_y}\right)^2\right)} \tag{3.9}$$

$$where,\ \dot{\theta_d} = \frac{1}{n-1}\sum_{i=1}^{n-1}\left(\frac{z_i - z_{i-1}}{d_i - d_{i-1}}\right), d \in [x\ ,\ y] \tag{3.10}$$

3.2.3. Probability Factor

As mentioned in the previous section, area A does not have a uniform distribution of shaded and illuminated parts. To take into account this non-uniformity, authors have defined a probability associated with each area element dA located on surface A. Probability that a randomly selected differential area element dA is illuminated by sunlight and visible from the albedometer is expressed in [43] as:

$$P_{ill+vis} = \frac{1}{1 + \Lambda[r, max(\theta_i, \theta_v)] + \kappa\Lambda[r, min(\theta_i, \theta_v)]} \tag{3.11}$$

Here, κ is an empirical relation developed by authors in [43] and is expressed as:

$$\kappa = \frac{4.41\phi_v}{4.41\phi_v + 1} \tag{3.12}$$

and, $\Lambda(r, \theta)$ is expressed as:

$$\Lambda(r,\theta) = \frac{r}{\cot|\theta|\sqrt{2\pi}} \exp\left(\frac{-\cot^2\theta}{2r^2}\right) - \frac{1}{2} erfc\left(\frac{\cot|\theta|}{r\sqrt{2}}\right) \tag{3.13}$$

In Equation 3.11 and Equation 3.13, r is rms of mean slopes of the surface as defined in [42] or the 'roughness' of the area, erfc is the complement of error function and θ_i & θ_v are the illumination angle and viewing angle respectively while, ϕ_v is angle between the projections of the illumination and viewing angle called as the projected viewing angle. These angles are depicted in Figure 3.4.

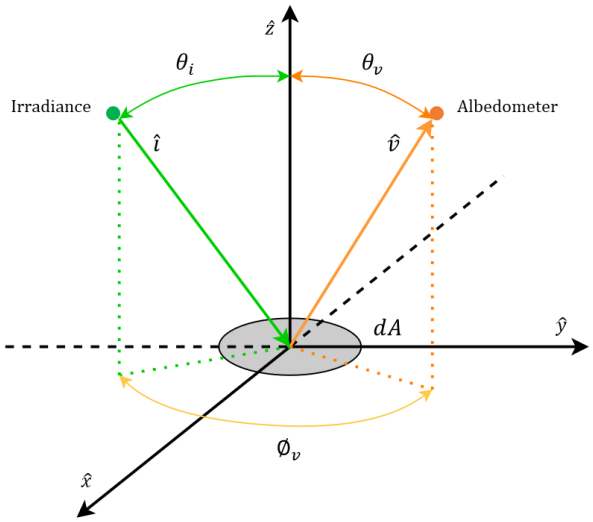

Figure 3.4: Coordinate system to visualize illumination angle θ_i, viewing angle θ_v and projected viewing angle ϕ_v for differential area dA

There are parts of area A_1 which do not receive direct light but can still contribute to the albedo value if it is visible from albedometer. The probability that a small area dA_1 is visible from albedometer is given as:

$$P_{vis} = \frac{1}{1 + \Lambda(r, \theta_v)} \tag{3.14}$$

As this probability factor P_{vis} only considers the visibility of the area element, it has no dependence with the angle of incidence like $P_{ill+vis}$. The inclusion of 'r' in the probability factor ensures correct representation the actual morphology of the area. Over the area A, the instantaneous illumination angle (or angle of incidence), θ_i is constant for an arbitrarily chosen differential area dA. However, viewing angle θ_v and projected viewing angle ϕ_v are different for each differential area dA throughout surface of area A. This is depicted in an illustration in Figure 3.5. Hence the distribution of probability $P_{ill+vis}$ and P_{vis} is not uniform throughout area A.

3.2.4. Chance Factor

As discussed earlier, the probability $P_{ill+vis}$ is not uniformly distributed throughout the surface of area A. Hence, the probability distribution is normalised over area A_1. Chance factor C, is defined as the weighted probability of $P_{ill+vis}$ over area A_1 which is expressed as:

$$C_i = \frac{\int\int_{A_{i1}} F_{S\to dA_{i1}} P_{ill+vis} dA_{i1}}{\int\int_{A_{i1}} F_{S\to dA_{i1}} dA_{i1}} \tag{3.15}$$

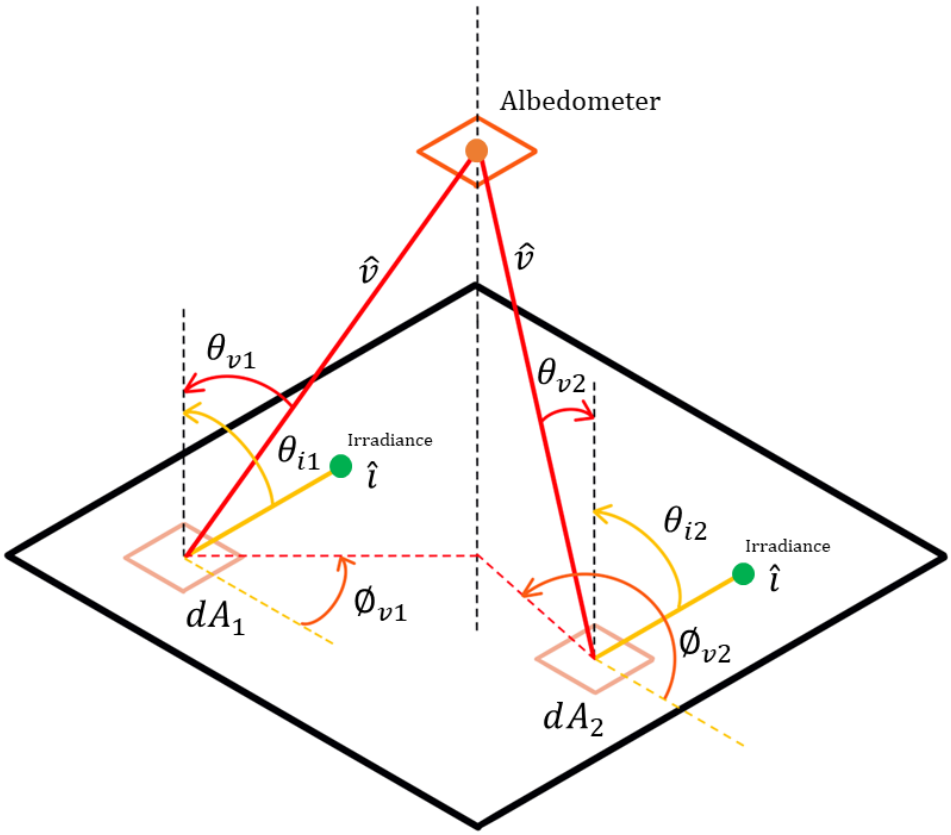

Figure 3.5: Viewing angle and projected viewing angle for different DSM cells in area A. Here, $\theta_{i1} = \theta_{i2}$, however, $\theta_{v1} \neq \theta_{v2}$.

where, the suffix i refers to the material of the surface. Similarly, P_{vis} for i^{th} materials from illuminated part (A_1) of area A is given as:

$$C_i' = \frac{\int\int_{A_{i1}} F_{S \to dA_{i1}} (P_{vis} - P_{ill+vis}) dA_{i1}}{\int\int_{A_{i1}} F_{S \to dA_{i1}} dA_{i1}} \tag{3.16}$$

Author in [21] has noted following important observations from Equation 3.4:

1. As the surface roughness in lower, $C_i \to 1$ and $C_i' \to 0$ and the surface is homogeneous with only one material, Equation 3.4 converges to Equation 3.1.
2. Instead of using irradiance weighted values of R and H, using wavelength dependent values $R(\lambda)$ and $H(\lambda)$, albedo values for a specific wavelength can be calculated .
3. The proposed equation holds true as long as:
   - the differential area dA_{i1} is isothermal, opaque and lambertian in nature
   - the incident wavelength is very small compared to the differential area ($\lambda^2 \ll dA_{i1}$)

4

Data Acquisition and Processing

Before converting the geometric albedo model into a functional MATLAB platform, appropriate input data needs to be acquired. This input data is often available in formats not directly compatible with the algorithm or has some discrepancies that need to be resolved before the data is made usable for the analysis. The input data required by the geometric spectral albedo can be classified into three broad categories. LiDAR data are used as the basis of all geometrical parameters, reflectance of materials is retrieved from spectral reflectivity data library and irradiance data are taken from Meteonorm.

4.1. Geometric Data

To analyse the local albedo of area with high spatial variations like modern cities, we first need a way to capture the geometrical arrangement of surfaces in the given area. Earth's surface can be mapped using Light Detection and Ranging (LiDAR) technology. Here, an aerial vehicle such as an aeroplane flies in sequential passes over the area. The aerial vehicle emits light pulse towards the ground surface. Light pulses are reflected differently from different surfaces dependent on the height of the object and its material. The time taken by the pulse to return to the aeroplane is used to calculate the elevation of different surfaces. Intensity of the returning light pulse is used to differentiate surfaces based on their average reflectivity values [44]. Figure 4.1 depicts the LiDAR data collection process using an aeroplane. The elevation data its corresponding geo-location data in combination is called a point cloud. Figure 4.2 depicts the LiDAR point cloud for the TU Campus in Delft.

After recording LiDAR data, a Digital Elevation Model (DEM) is created from the obtained point cloud for the area. DEM represents raster-grid of elevation data of surfaces above the 'bare ground' compared to the theoretical mean sea level ($0\,m$) [44]. DEMs are classified as Digital Surface Models (DSM) and Digital Terrain Models (DTM). A Digital Surface Model (DSM) represents the elevation data of all surface points above the bare-ground including vegetation, water resources, buildings and other municipal infrastructure located in the given area. Effectively on a global scale, it represents a continuous surface of the Earth. A Digital Terrain Model (DTM) on the other hand, represents the elevation data of the bare-ground surface when all the natural and man-made surface points are filtered out from a DEM. Figure 4.3 visualizes the difference between a DSM and a DTM. DSMs are recorded

In the Netherlands, LiDAR data is available as an open source platform called 'AHN'. AHN data is a highly detailed and accurate height map data of above ground surfaces throughout the Netherlands. The 3D altitude data is measured in meters with respect to the Mean Sea Level ($0\,m$) and has a tolerance of 5 centimeters in elevation values per m^2 area for the latest version of AHN dataset (AHN 4) [47]. Point cloud data of an area can be visualized using various GIS software like ArcGIS Pro. First set of AHN data was collected from 1997 to 2004. Thus, AHN1 data has varied point cloud density depending on when it was collected. It can vary from 1 point per $16\,m^2$ (for earliest collected AHN 1 data) to 1 point per m^2. The latest version of AHN dataset (AHN 4) in existence was collected from 2019-2022 with substantially higher point cloud density of 8 points per m^2 [48]. More information about AHN data can be found in Appendix A.

This point cloud may also contain some noise such as arbitrarily high or low elevation values, no data values and non-uniform point cloud density, for example, if the aeroplane capturing the LiDAR

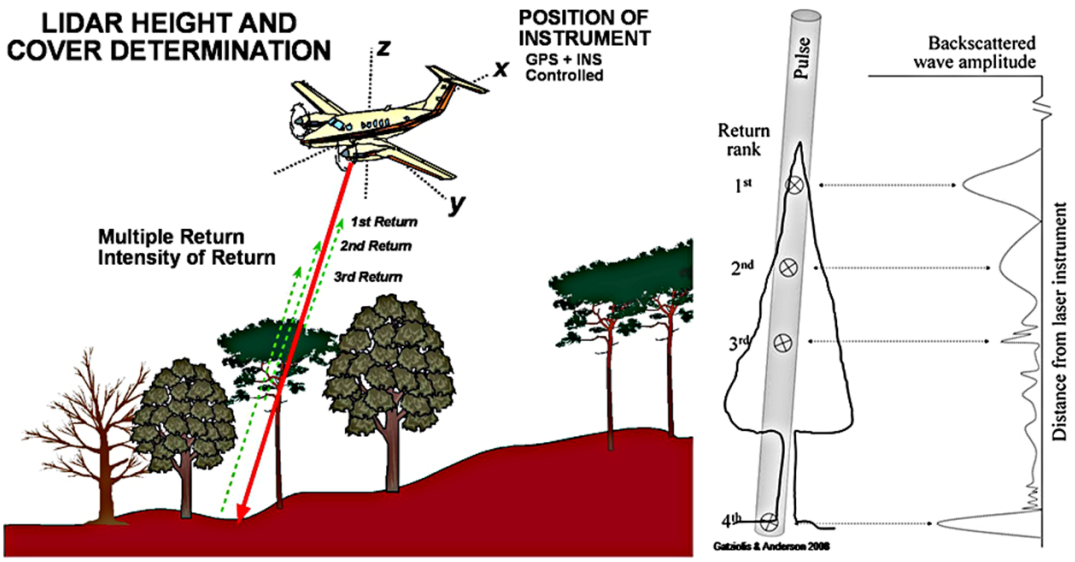

Figure 4.1: Taller objects (objects closer to the albedometer) reflects light the fastest and thus the light returning from these objects gets detected the first [45](Left). Based on the order in which light pulses return to the aeroplane, bare-ground and objects existing above the ground are identified. The most significant returns are 1 and 4 which are used for bare-ground terrain model and 1st return is used to model natural and man-made surfaces above the ground surface.[46] (Right)

Figure 4.2: LiDAR point cloud for TU Campus in Delft for AHN3 dataset. High-Rise of the EEMCS department is highlighted in purple square

data flies over vehicle and mistakenly records the elevation of vehicle and associates it with ground surface. Sometimes the returning light pulse does not get detected properly, so no data is recorded for that small area. Apart from that, the non-uniform distribution of point clouds can be addressed by converting the point cloud data into a DSM using various GIS softwares such as QGIS, ArcGIS Pro etc. The smallest unit of a DSM is called a cell. The size of this cell is indicative of the resolution of

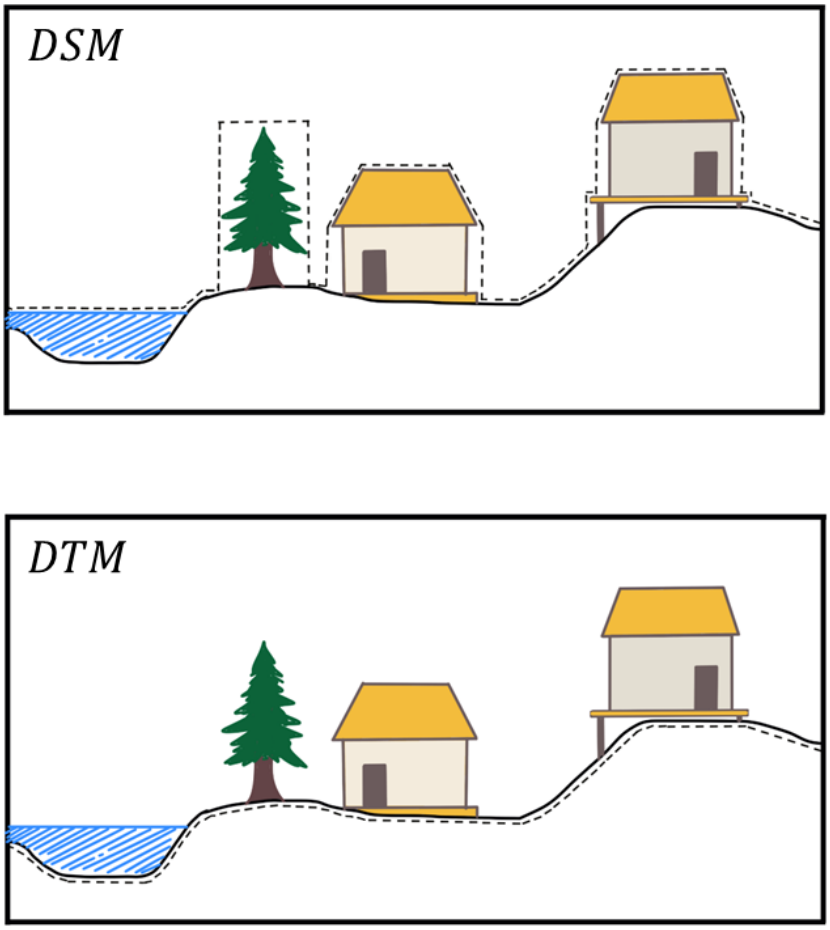

Figure 4.3: (Top) Dotted line represents a Digital Surface Model (DSM) of the location. (Bottom) Dotted line represents a Digital Terrain Model (DTM) of the location.

the DSM. Smaller the dimension of this cell, higher is the resolution. All LiDAR points contained in this unit cell, are aggregated under the cell. The centre of this DSM cell has real world geo-location (X and Y co-ordinates). The elevation of this cell (Z co-ordinate) is some function elevation of all the points contained in the cell. Generally average elevation or maximum elevation of all the points is assigned as the elevation of the DSM cell for ground surface points. The maximum elevation of all the points is assigned as the elevation mainly for generating a DEM.

For AHN1, due to low point cloud density, the selected DSM cell size is $5\ m \times 5\ m$. For AHN2, AHN3 and AHN4, DSM cell can be selected as $0.5\ m \times 0.5\ m$. As AHN1 is older than other datasets, (for South Holland AHN 1 was recorded from 2001 to 2003), the data has a lot of irregularities and inconsistencies. For example, water resource data is not collected at many places and point cloud density is very low in some areas. The collected data is also not directly classified into buildings, vegetation and water. Although, AHN2 data has improved point cloud density than AHN1, it is also not directly segmented into different material classes. Hence, the datasets were run through a manual custom filter on ArcGIS pro to separate building points. Then, another manual filter was used to separate vegetation points and the no data points were associated with water resources with an average height $-2.9\,m$. This is further explored upon in chapter 6.

Once we have the DSM ready for all the datasets, it is essential to segment the DSM into operable units. These segmented units are called 'sub-tiles' in all future instances. These sub-tiles essentially represent the area A in the geometric spectral albedo model discussed in the previous section. These dimensions of these sub-tiles are not decided arbitrarily. The sub-tile was chosen to be square for simplifying roughness calculation and the view factor algebra. Using square shaped sub-tiles also lets us segment the area of Delft uniformly and allows comparing albedo values for same sub-tile for

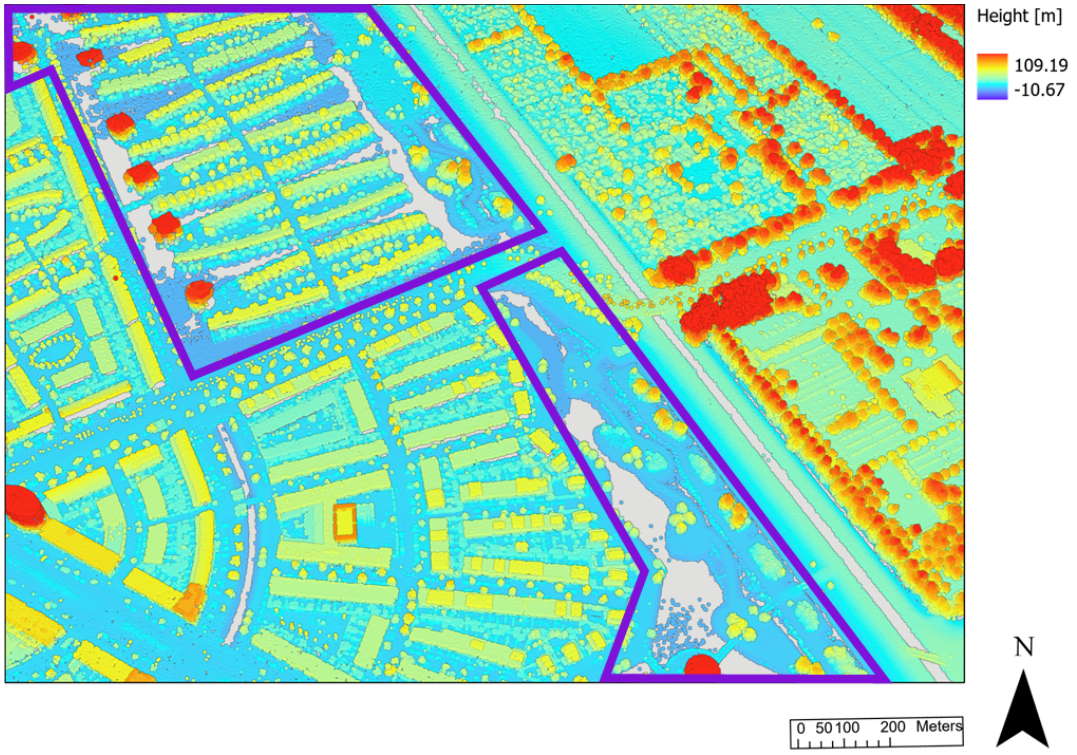

Figure 4.4: Point cloud for outskirts of Delft for AHN3 dataset. Areas highlighted by purple shapes shows inconsistency in LiDAR point cloud. Commonly, these inconsistencies are No data points and uneven point cloud density.

different AHN datasets. The height of the albedometer is what drives the size of the sub-tiles. This is because, the area viewed by the albedometer is a function of the height of the albedometer. To explain this, consider the albedometer surface to be a square of $1\,m^2$ area. The albedometer is assumed to be located at the centre of this sub-tile at height 'Ha'. View factor of two co-axial square surfaces is simplified by author in [49]. Using this simplified view factor algebra we can calculate the relation between the height of albedometer (Ha), dimension of the sub-tile and the view factor ($F_{S\to A}$) of the sub-tile (A) with respect to the albedometer surface (S).

Now, for Delft, the maximum height of any point is 108 m. The height of the albedometer should be higher than the highest point in the area. Thus, the sub-tile which contains the highest point in Delft, should have the albedometer height greater than 108 m. However, not all sub-tiles have buildings, taller trees or other tall objects. The albedometer height for such areas can be reduced. However, in doing so, we do not have uniform distribution of area in Delft. Apart from that, the landscape of Delft has changed throughout the past two decades. Thus, it might not be possible to divide the area of Delft in the same way for different AHN datasets. With this, it might not be possible to compare the albedo values for same part of Delft if the sub-tile distribution for different AHN datasets is different. For this reason, we decided to keep the height of the albedometer constant throughout the area of Delft and for different AHN datasets at $110\,m$.

With the height of albedometer decided, the dimension of a sub-tile is calculated such that the view factor of the entire sub-tile from an albedometer located $110\,m$ above the centre of this sub-tile converges to one ($F_{S\to A} \to 1$). This ensures that the albedometer only views the area under a sub-tile being analysed and areas in the surrounding sub-tiles do not contribute to the view factor of the central sub-tile. Using height of albedometer as $110\,m$ and the simplified view factor algebra in [49], the dimension of sub-tile was found to be $1250\,m \times 1250\,m$. Thus, AHN datasets for Delft can be divided into 40 sub-tiles. The size of the DSM cell (0.25 m^2 for AHN2, AHN3 and AHN4 and $25\,m^2$ for AHN1), when compared with the size of the sub-tile ($1.56 \times 10^6\,m^2$), amounts to a very small fraction of the sub-tile. Thus, we can attribute area A in the geometric spectral albedo model as the area of sub-tile and each DSM cell can be associated as the small differential area element dA located in area A.

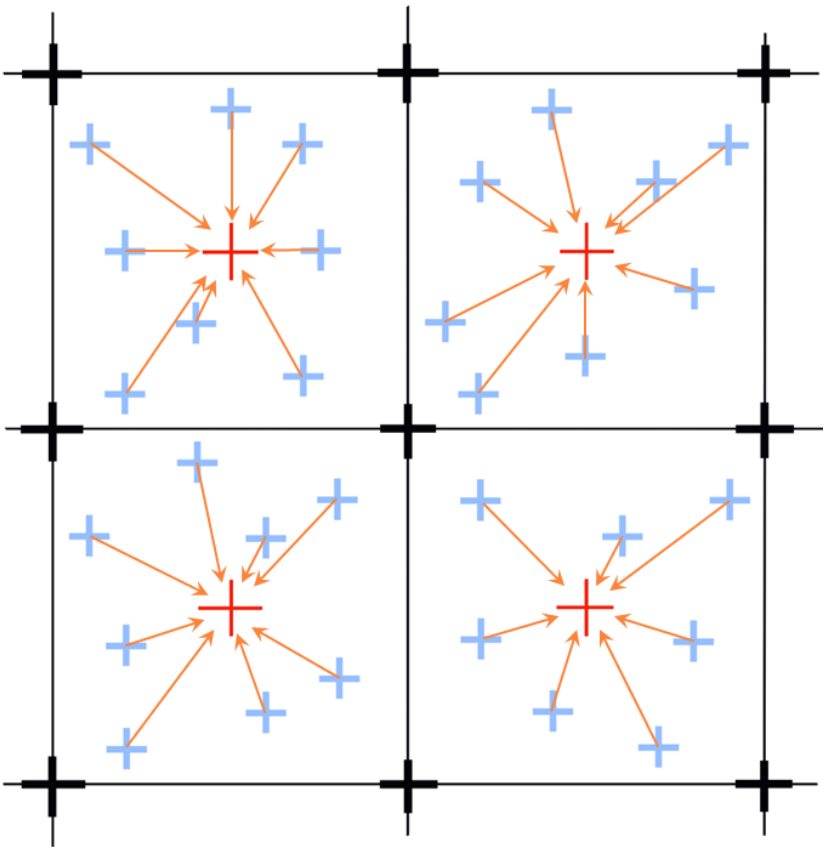

Figure 4.5: Algorithm depicting the creation of DSM from a point cloud. Here, maximum height of all the points is assigned to the centre of the DSM cell (red cross)

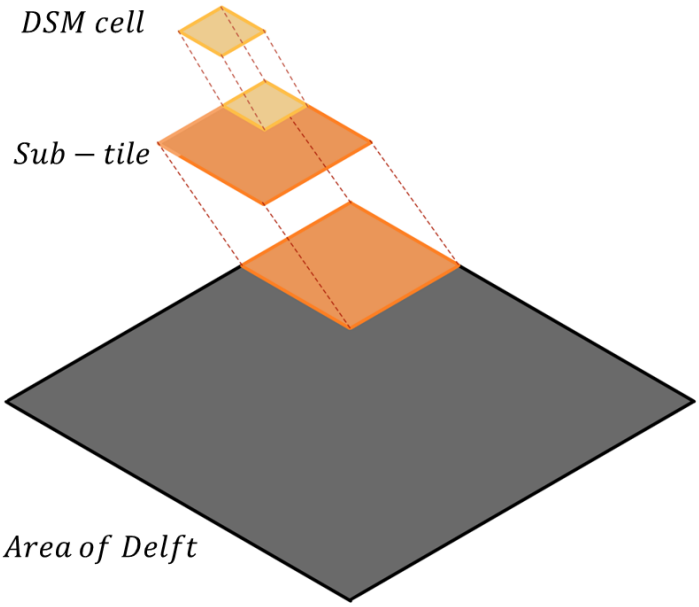

Figure 4.6: Visual depiction of DSM cells which are sub-set of a sub-tile which is in-turn a sub-set of total area of Delft (figure is not to scale)

4.1.1. Reflectance Data

Urban environments have a variety of natural and man-made reflective surfaces. This includes leaves, grass, bark and water (natural) and concrete, paints, asphalt, glass, plastic and various metallic surfaces (man-made). These surfaces have different spectral reflectivity values. The reflectivity values for some of these surfaces change periodically with seasons. For example, wilting of leaves, flowers and other such organic matter changes its reflectivity. Not only that, weather can induce change in reflectivity values of surfaces. For example, presence of water/ snow on surfaces changes its reflectivity. Due to presence of several reflective surfaces with changing reflectivity values, analysing the reflection of light has become more complex for modern urbanscapes. The reflectivity values for different materials are available as spectral reflectivity vs wavelength data in the ASTER spectral Library. Image below depicts the reflectivity spectrum for concrete.

The spectral reflectivity data for material is also a function of spectral GHI incident on the surface. It is possible to change only the material of surface without changing its geometry, for example, painting a wall, influences its reflectivity but does not affect its geometry. Spectral irradiation data (GHI vs wavelength) based on the reference AM1.5 spectrum is developed by [50, 51]. This data is generated using Simple Model of the Atmospheric Radioactive Transfer of Sunshine (SMARTS2 : version 2.9.2) and it is published on the official website of National Renewable Energy Laboratories(NREL) [52]. Figure 4.7 depicts the spectral irradiance for the reference AM1.5 spectrum modelled using SMARTS2. However, the spectral irradiation incident on the surface of the Earth changes with location and time. Thus the hourly spectral GHI data from $50.77^o\ N\ 3.57^o\ E$ to $53.36^o\ N\ 7.11^o\ E$ for 2005 were retrieved. These coordinates encompass the Netherlands. This data was normalized using the average hourly GHI values obtained for Delft from Meteonorm. Equation 4.1 represents the expression used for normalizing the spectral GHI data for the Netherlands with the GHI data from Meteonorm. In this expression, $G(\lambda)$ is the spectral irradiance used for calculating reflectance 'R'. GHI_S is the spectral GHI data. GHI_H and GHI_D are the hourly broadband GHI data for the Netherlands collected using the SMARTS2 model for 2005 and the hourly GHI data from Meteonorm respectively. As, the hourly GHI spectra for the specified latitude and longitude range and the reference AM1.5 spectrum have the same spectral coverage of 280 nm to 4000 nm, λ varies from 280 nm to 4000 nm and n varies from the first hourly GHI value to the last GHI value in the selected sample size.

$$G(\lambda) = GHI_S(\lambda) \times \frac{GHI_D(n)}{GHI_H(n)} \tag{4.1}$$

However, the spectral coverage and resolution of reflectivity values for different materials might be different than the reference AM1.5 spectrum. Hence, individual wavelength values for both reflectivity and AM1.5 spectrum were matched. Common wavelength values shared between the two spectra are considered in the analysis. After the spectral matching, Equation 3.2 is used to calculate reflectance value for a specific material.

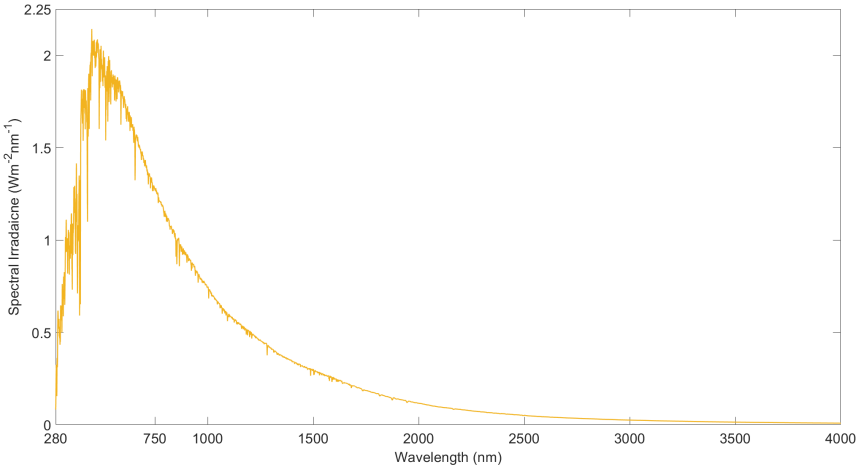

Figure 4.7: Spectral irradiance in ($Wm^{-2}nm^{-1}$) vs the wavelength (nm) for AM1.5 spectrum

The ASTER library is scanned to find the best possible match between materials available in the library and the materials of classified DSMs. Specifically, from the ASTER library, reflectance data for construction concrete were selected for points belonging to the buildings class in DSM. Figure B.1 depicts the spectral reflectivity of concrete. Similarly, reflectance data for pine trees was selected for points belonging to the vegetation class, reflectance data for 'alfisol fragiboralf' soil was used for ground points and tap water reflectance data was used for water resources. Figure 2.5 and Figure B.3 depicts the spectral reflectivity of alfisol soil and water respectively. As for vegetation, the ASTER library contains multiple samples for pine trees from the genus *pinus*. Out of all, the species *pinus strobus* or 'Eastern White Pine' is chosen. Figure B.2 depicts the spectral reflectivity of pine trees. All these samples were first averaged to obtain a single spectrum of reflectivity values for Pine trees.

4.1.2. Irradiance Parameters

Influence of solar irradiation on albedo is quantified by the Relative Shade Brightness (RSB), as the name suggests, indicates the brightness or darkness of shadows and it can be expressed as:

$$RSB = \frac{1}{H+1} \tag{4.2}$$

At first, input data is obtained from Meteonorm as the hourly irradiance and solar position data for a typical meteorological year in Delft. In this data, solar azimuth is measured by assuming South direction as 0^o azimuth. Thus 180^o is added to the solar azimuth values to match the convention of measuring solar azimuth from North. Firstly, solar azimuth and solar altitude data is used for find hourly values of angle of incidence (AOI). Cosine of angle of incidence is expressed in [22] as:

$$\cos(AOI) = \cos a_M \cos a_S \cos(A_M - A_S) + \sin a_M \sin a_S \tag{4.3}$$

where, a_M and A_M are the altitude and azimuth of investigated surface and a_S and A_S are the altitude and azimuth of the sun. In this case, we are assuming that the surface of the module is analogous to the small differential area dA and it is parallel to the ground surface. Thus the altitude of this surface $a_M = 90^o$, which simplifies Equation 4.3 as follows:

$$\cos(AOI) = \sin a_S \tag{4.4}$$

Then, DNI, DHI and and AOI values are used to calculate the factor H as expressed in Equation 3.3 followed by the relative shade brightness expressed in Equation 4.2. Figure 4.8 and Figure 4.9 represent variation of direct normal irradiance, diffuse horizontal irradiance and relative shade brightness for one day. It is important to note that, relative shade brightness does not have defined values when diffuse irradiance is zero. This indicates that hourly values for nigh-time as irrelevant for this analysis. Thus, we can discount hourly values of all the irradiance parameters that belong to night-time.

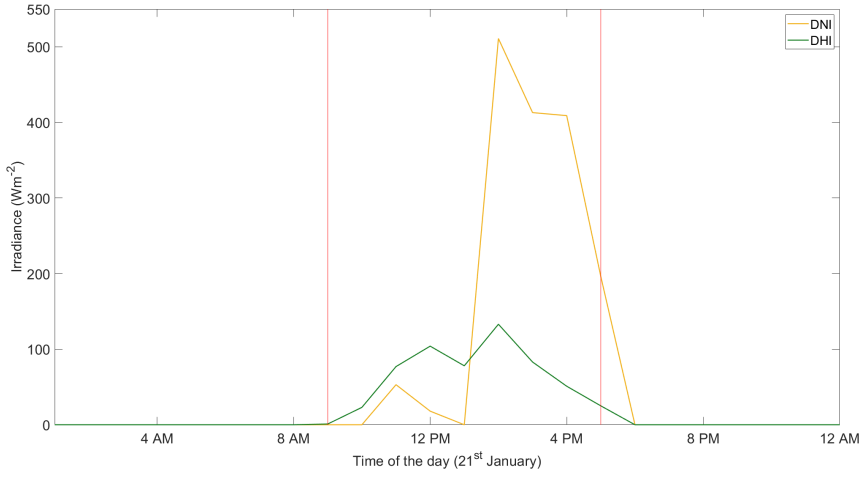

Figure 4.8: Direct normal irradiance (DNI) and Diffuse horizontal irradiance distribution for 21^{st} January. (the reason behind selecting this day is discussed later in **??** and section 6.1)

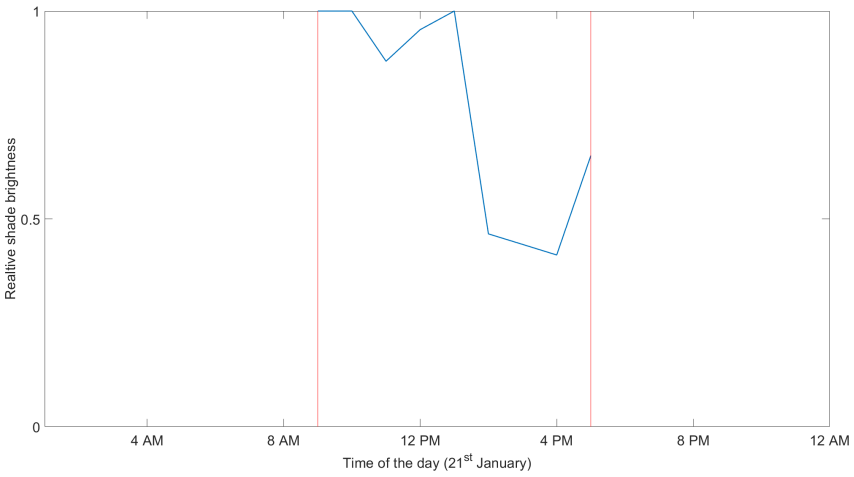

Figure 4.9: Relative shade brightness distribution for 21^{st} January.

5

Methodology

In the simplified version of the GSA model, area A is assumed as a smooth homogeneous surface with just one material. With the addition of complex geometry, roughness and different materials in the area into consideration, the GSA model can be used to calculate albedo for real life natural and man-made surfaces. From Equation 3.4, it can be inferred that contribution of parts of area A with different materials ($R_1,\ R_2,\ R_3,\ \ldots.\ R_N$) is calculated individually, then the individual albedo components are integrated over the total illuminated and shaded area (A_{i1} and A_{i2},where i ranges from 1 to N) occupied by that particular material. This integration yields the total albedo of area A. However, Only 'R' values in Equation 3.4 have material dependence, which means that other parameters like view factors, probability factor, chance factor, and illumination profile An alternative methodology is suggested in the following sections

5.1. Sequential processing on data

As discussed in the last chapter, the acquired DSM data needs to be processed further. Figure 5.1 depicts the algorithm used for segmenting the DSM into 40 sub-tiles. Thus, this segmented data can be sequentially processed to calculate geometrical parameters like view factors and roughness. Some parameters are calculated based on both the sequential input of DSM data and hourly input of irradiance parameters like solar position and irradiation. Parameters like probability factor, reflectance profile, illumination profile, chance factor are calculated this the algorithm depicted in Figure 5.2. Finally, the aforementioned parameters are combined to calculate albedo value for one sub-tile and one hourly value.

5.2. Geometrical parameters calculation

As discussed in the previous chapter, view factor and roughness of a sub-tile can be calculated sequentially. Before calculating view factor, geometrical dimensions 'Da' and 'd' need to be calculated. 'Da' and 'd' represent the horizontal and diagonal distance between the centre of DSM cell and the albedometer position. As, height of the alebdometer is 110m , Ha=110 m. Height of an arbitrarily selected DSM cell the the sub-tile is denoted by 'h_{dA}'. These dimensions are depicted in Figure 5.3. As a DSM cell (dA) and albedometer (S) are parallel to each other, the angles β_1 and β_2 are equal. Thus, we can simplify the view factor algebra as expressed in Equation 5.2. Thus, view factor for each DSM cell in the selected sub-tile can be calculated sequentially.

$$F_{S\rightarrow dA} = \frac{\cos\beta_1 \times \cos\beta_2}{\pi\, d^2} \times \int dA \tag{5.1}$$

As, $\cos\beta_1$ and $\cos\beta_2$ can be expressed as ratios of 'Da', '$Ha - h_{dA}$' and 'd', this relation can be further simplified as,

$$F_{S\rightarrow dA} = \frac{(Ha - h_{dA})^2}{\pi\, d^4} \times dA \tag{5.2}$$

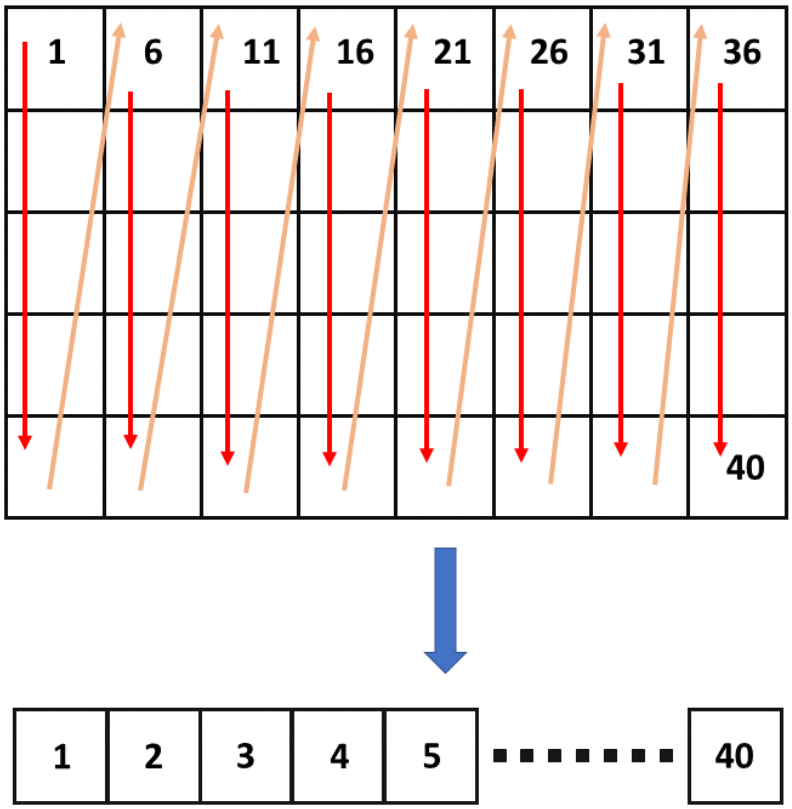

Figure 5.1: A depiction of algorithm used for segmenting the DSM dataset into the sub-tiles.

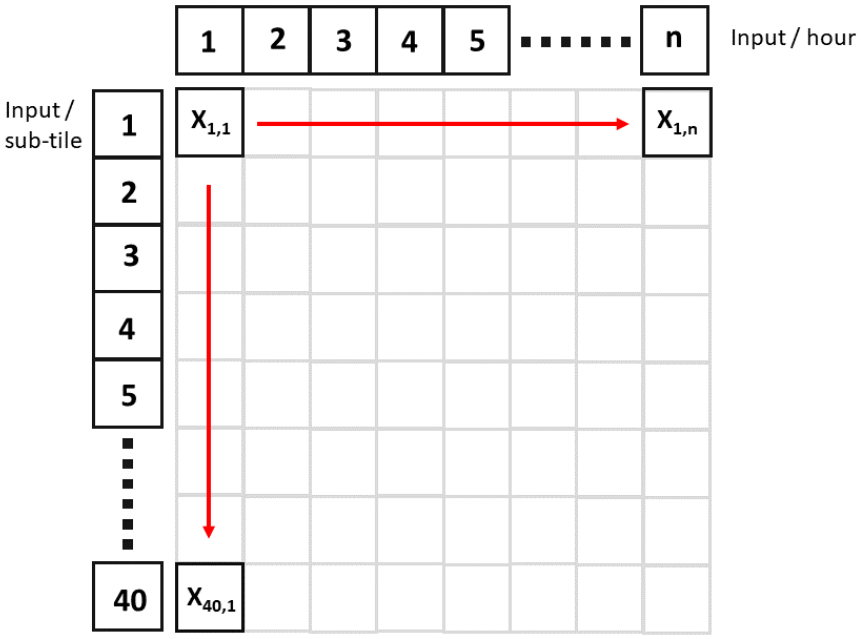

Figure 5.2: A depiction of algorithm used for calculating parameters that vary per sub-tile and per hour. 'x' denotes parameters like probability factor, reflectance profile, illumination profile, chance factor and albedo.'n' is the total number of hourly values selected for analysis

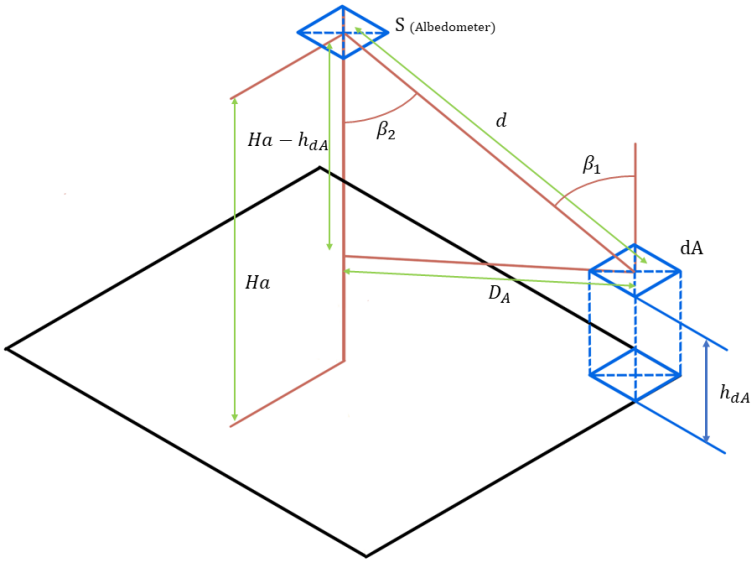

Figure 5.3: Figure depicting different geometrical dimensions of the sub-tile for simplifying view factor algebra for the sub-tile

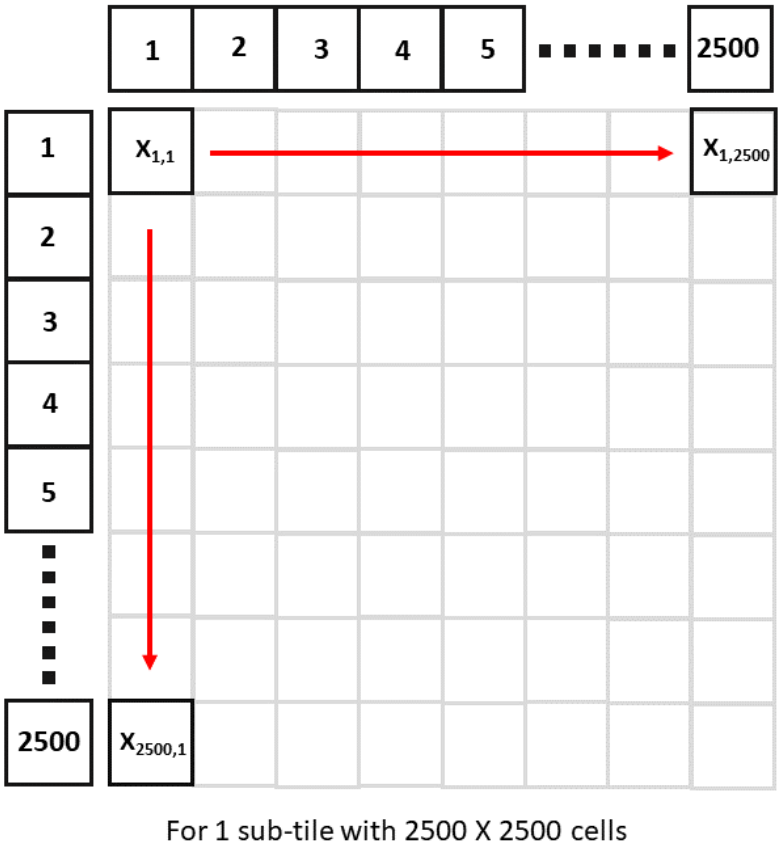

Figure 5.4: A depiction of algorithm used for calculating parameters that vary per sub-tile and per hour. 'x' denotes parameters like Da, d, and the view factor $F_{S \to dA}$

To calculate roughness of the sub-tile, the mean slope in x and y direction are calculated for the entire

sub-tile using Equation 5.4. Then, 'r' is calculated for each sub-tile sequentially using Equation 5.3.

$$\Delta_q = \sqrt{\frac{1}{area(A)^2}\sum_{i=1}^{n-1}\left(\left(\frac{\delta_{zi}}{\delta_{xi}} - \dot{\theta_x}\right)^2 + \left(\frac{\delta_{zi}}{\delta_{yi}} - \dot{\theta_y}\right)^2\right)} \tag{5.3}$$

$$where,\ \dot{\theta_d} = \frac{1}{n-1}\sum_{i=1}^{n-1}\left(\frac{z_i - z_{i-1}}{d_i - d_{i-1}}\right), d \in [x\ ,\ y] \tag{5.4}$$

Before calculating the probability factor, the angle of incidence, viewing angle and the projected viewing angle for all DSM cells in a sub-tile need to be calculated. Angle of incidence is calculated with irradiance parameters. Angle β_1 can be equated with the viewing angle shown in Figure 5.3. Figure 3.4 depicts the angles and their relationship with each other. To find the projected viewing angle, unit vectors $\hat{i_u}$ and $\hat{v_u}$ along the angle of incidence and viewing angle respectively are projected on the horizontal plane. Then, scalar product of these two unit vectors can be used to calculate the angle ϕ_v between them.

$$\hat{i_u} \cdot \hat{v_u} = |i_u||v_u| \cos\phi_v \tag{5.5}$$

Angle of incidence is constant for all DSM cells at a given hour. However, the viewing angle and projected viewing angle change with the position of the DSM cell in the sub-tile. So, the lambda function and the empirical constant κ expressed in Equation 3.13 and Equation 3.12 are calculated for each DSM cell in the sub-tile. Finally, probability factor $P_{ill+vis}$ is calculated using Equation 3.11 and probability factor P_{vis} is calculated from using expression in Equation 3.14. These aforementioned parameters are calculated according to the algorithm depicted in Figure 5.2 and Figure 5.4, where, angle of incidence is the input per hour. viewing angle is the input per sub-tile. Thus, projected viewing angle, lambda function and probability factors are calculated for every sub-tile and for every hour sequentially.

In GSA model, chance factor C and C' are expressed in Equation 3.15. The notations in the equation indicate that the chance factors are different for different materials. However, there is no parameter in the equation that is material dependent. Thus, chance factors C and C' are integrated over total area of the illuminated DSM cells in the sub-tile. Much alike roughness, C and C' values are calculated for each sub-tile sequentially.

5.3. Reflectance assignment to surfaces

In the previous chapter, reflectance values were calculated from spectral reflectivity data. These reflectance values are computed for each hour. The DSM files divided into four material classes are also segmented into sub-tiles as depicted in Figure 5.1. In combination, a reflectance profile is generated for every sub-tile and every hour sequentially.

The DSM for different material classes are modified such that each index will have a value of '1' or '0'. For example, in DSM for building class, all surfaces corresponding to man mad structures have a '1' value while the rest have a'0' value. Figure 5.5 depicts the algorithm used for the creation of a matrix that contains Reflectance 'R' values.

5.4. Illumination profile generation

Illumination profile of the sub-tile is a dataset indicating binary values based on in illumination condition of each DSM cell in the sub-tile. This can be achieved by implementing line-of-sight assessment. A MATLAB function 'los2' can be used for this purpose. Figure 5.6 depicts the line-of-sight analysis used by 'los2'. Hourly data of sun's azimuth and altitude is available on Meteonorm. In reality, sun is about 1 AU or 150 million km. However, rendering sun's position this far away would not be feasible for analysis. Hence diagonal distance from the centre of each DSM cell to the projection of solar position is assumed to be 75 m. The algorithm connects the projection of solar position and the centre of each DSM cell and checks if this line is intersected by any surface. Intersection would indicate that the line-of-sight of the centre of DSM cell from sunlight is obstructed. Hence the cell will be shaded. The opposite is true if there are no intersections. The first element to be initialized is the one on the right bottom corner of the area. Thus, an illumination profile for every sub-tile and every hour can be calculated sequentially.

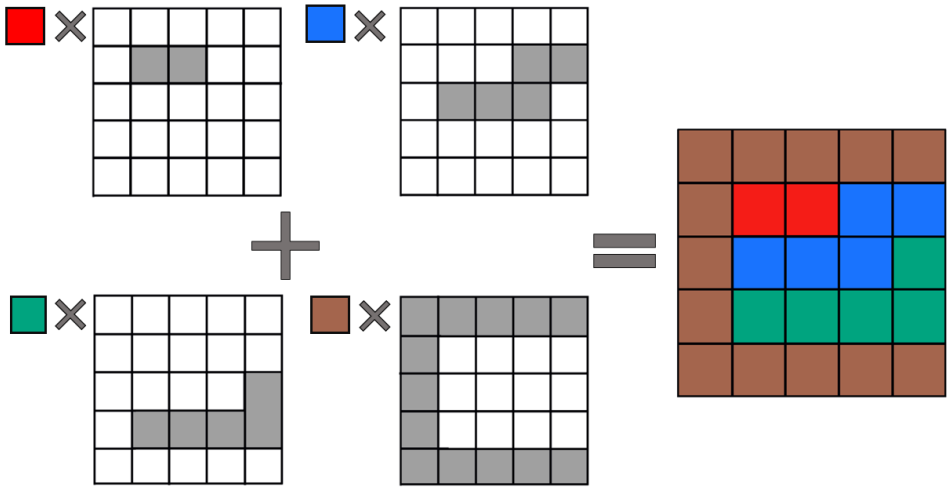

Figure 5.5: Image depicts the algorithm used for generating the matrix with reflectance values. There are four different materials, R_1, R_2, R_3, R_4 represented by four different colours (red, blue, green and brown). DSM files are combined with their respective reflectance values

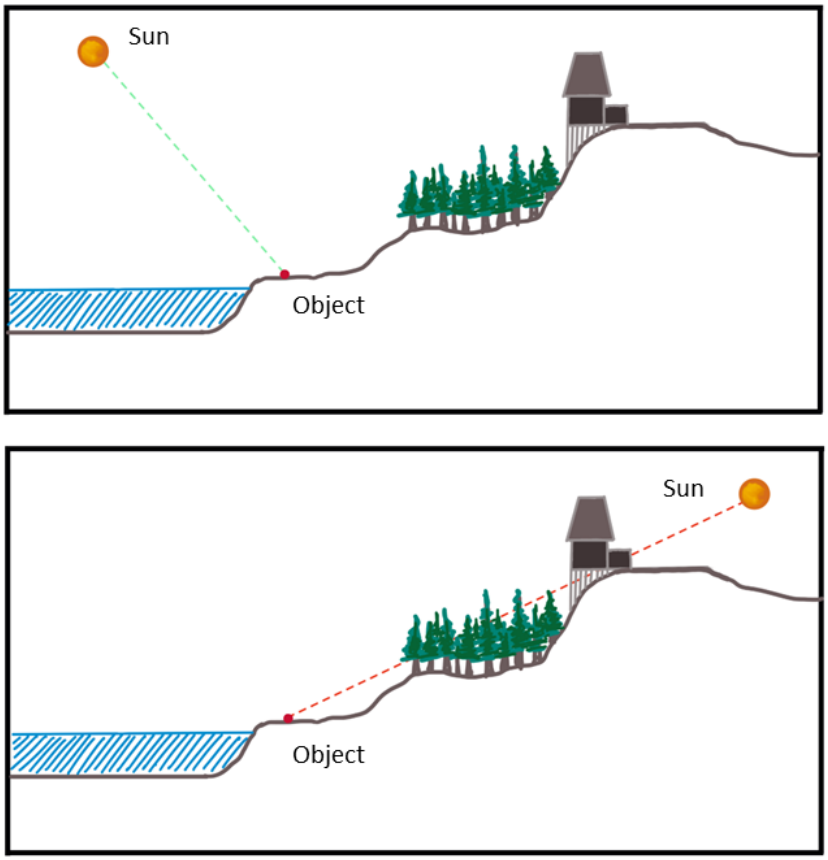

Figure 5.6: Line-of-sight assessment algorithm used by the 'los2' function in MATLAB depicted in a simplified version. The line-of-sight is clear early in the morning (top) whereas it is obstructed in the evening (bottom)

6

Constraints and Optimization

This chapter focuses on the constraints imposed on the algorithm, the development of MATLAB platform and ultimately, the results that were derived from this process. We will also comment on the methods used for optimizing the algorithm and the functional approach. The constraints generally arise from a range of factors like the spatial resolution of the LiDAR data, high spatial variations in a location, technological advancements or lack thereof, spectral resolution and range of the reflectivity data, and temporal coverage of irradiance data. However, there are a few constraints that find their origin in the basics of geometric spectral albedo model.

6.1. Constraints

6.1.1. LiDAR data inconsistency

The first and foremost constraint is imposed due to the spatial resolution of the LiDAR data. As discussed earlier, AHN1 dataset was recorded 18 years ago. Due to the limitations of the technological advancements at the time, the spatial resolution of this data is well below the current resolution available. This implies that due to fewer recorded LiDAR data points, more gaps had to be filled using interpolation of data. Even with interpolation, there are a lot of gaps in the data because the area does not have enough points to support interpolation. This can be observed in Figure 6.1 from the data points (white space) and gaps (streaked black lines). Thus, the data loses some amount of credibility. This is especially true for AHN1 dataset.

AHN1 is the oldest, so it is least consistent point clouds density. Images depict the loss of data with cell size from $0.5\,m$ to $2.5\,m$. Compared with AHN3, which has $\approx$ 1 billion points, AHN1 dataset only has $\approx$ 18 million points. Thus, even at cell size of $5\,m \times 5\,m$, the data still has gaps and the resolution of objects is very poor which is indicated in Figure 6.2. This is the reason for unusually low roughness values for AHN1 dataset. Eventually, the albedo value range and variation is affected by the low credibility of AHN1 data.

6.1.2. Identifying materials and assigning reflectivity values

This constraint arises from the limitation to classify the LiDAR points into multiple material classes. As discussed earlier, AHN 1 and AHN2 datasets are not directly classified into material classes such as buildings, vegetation and water resources. However, AHN1 and AHN2 datasets by default can be classified into ground points. To classify the data further, LiDAR point clouds is imported in ArcGIS pro where custom filter were used to create and classify the DSM into building, vegetation points. Finally, places where no data was recorded, were associated to water resources. Unlike, AHN1 and AHN2, newer datasets are directly classified into multiple classes. Even so, AHN3 and AHN4 datasets are limited to the four material classes mentioned before. Moreover, further classification of building points into specific materials such as concrete, shingles, pavement, metallic surface etc. or ground points into grass, soil, road asphalt etc. is still not possible for these datasets.

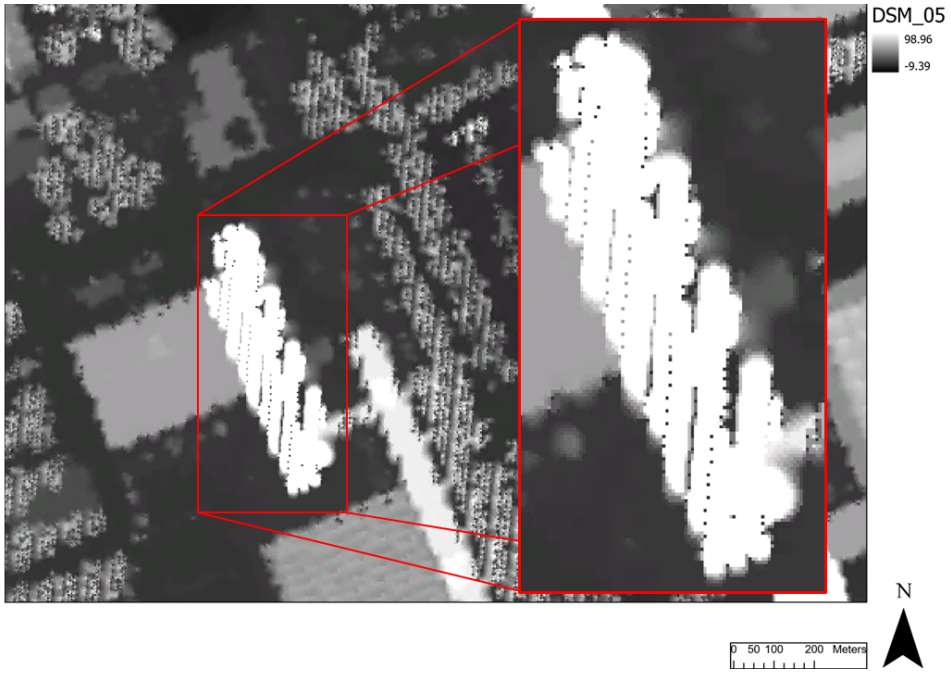

Figure 6.1: DSM created for AHN1 dataset with a cell size of $5\,m \times 5\,m$ with zoomed in view of the high-rise building of EEMCS

Figure 6.2: DSM created for AHN1 dataset with a cell size of $5\,m \times 5\,m$

6.1.3. View factor algebra

As discussed before, view factor is used to denote the contribution of reflected irradiation from a differential area element dA in the total reflected irradiation received by the albedometer. This constraint arises from the definition of view factor algebra used in this analysis and how it influences albedo. The area viewed by the albedometer is the function of the height at which it is mounted away from the surface of area A. To begin the analysis consider an area A with dimension of $500\,m \times 500\,m$ .Assume that area A has points with a maximum height > 65 m and a minimum altitude of 0 m. The albedometer will be placed at somewhere between the 65 to 70 m. This increases the area viewed by the albedometer

from an area of $500\,m \times 500\,m$ to an area of $\approx 795\,m \times 795\,m$ (using the simplified view factor algebra developed by [49]). With the inclusion on this extra area, if the maximum height is increased to 80 m, the height of albedometer now needs to be more than 80 m. This forces the algorithm in a loop until the maximum height of any point is lower than the albedometer and albedometer focuses on the same total area. In this way, the spatial resolution of the albedo map is a function of height of albedometer above the ground surface. By convention, albedometer is mounted at an height of 1.7 to 2 m. Thus, the minimum area for which albedo can be calculated using this algorithm is $22.7\,m \times 22.7\,m$.

Apart from that, the aforementioned logic, would result in unequal distribution of sub-tiles in terms of their sizes. Not only that, the distribution of sub-tiles might not be consistent for between different AHN dataset. Thus, It was decided that the height of the albedometer will be held constant for the area of Delft, to ensure even distribution of sub-tiles into squares of equal sizes.

6.1.4. Temporal coverage and Spectral resolution

The frequency of the irradiance parameters available from Meteonorm also influences the frequency at which albedo can be calculated for a given area. Conventionally, irradiance data is available as hourly values. Usually, this is not a problem as it is sufficient to analyze hourly albedo values. The spectral dependence of albedo is due to reflectivity and irradiation. The spectral matching process explained in subsection 4.1.1, combines the spectral resolution and range of reflectivity data for different materials with the spectral irradiation. Albedo calculation is possible for this combined resolution and range of both reflectivity values and irradiation.

6.1.5. Functional approach on MATLAB

A constraint was also imposed due to considerable time required to run the program for every AHN dataset for all the hourly values in a year. As discussed earlier, albedo is calculated for all 4 AHN datsets, each containing 40 sub-tiles, each sub-tile contains 625000 DSM cells. This step is repeated for all hourly values. After removing the night hourly values from the total hourly values of 8760, the total day-time hourly values left were 4560. Even if the MATLAB platform is able to calculate albedo for one sub-tile and for one hour in 1 minute, the total time taken for albedo calculation for 40 sub-tiles and 4560 hourly values is 126 days. However, currently, the MATLAB program calculates albedo for sub-tile and for one hour in $\approx$ 2 to 3 minutes. Hence, it was decided to compromise on the temporal resolution of the analysis and only select specific spread evenly in the year for this analysis. As discussed in the previous chapter,a custom-built function was used to select hourly values for specific days in a year (Solstice and Equinox days).

Some constraints are imposed by the computational capability of MATLAB. As MATLAB stores data in matrices, bigger the matrix dimensions, the higher is the memory used by MATLAB to store and access it. Thus, huge arrays such as for the probability factor, view factor, or illumination profile take up excessive amounts of RAM and sometimes are straight up impossible for MATLAB to initialize. This is why, the algorithm calculates intermediate parameters for every sub-tile and then repeats the calculation for all hourly values. This necessarily requires the use of loops which ultimately adds to the computation time.

6.1.6. Function for Illumination profile

To calculate which DSM cells in the sub-tile are illuminated and shaded for any given hourly value, custom version of viewshed analysis was implemented. In this analysis, 'los2' function was used as to evaluate the illumination profile. This function evaluates the line-of-sight of each DSM cell to determine if it is illuminated or shaded. This single element approach means that it takes longer for the custom-built function to compute the illumination profile of entire sub-tile for one hour. This is essentially the most time-consuming step in the entire algorithm. Apart from that, the algorithm used for the line-of-sight assessment generates the geographical layout of the area to visualize the DSM cell and the solar position for each instance 'los2' is used. This is a very heavy computational task as it generates bigger arrays that occupy RAM.

Initially, generating the illumination profile of one sub-tile for one hour required about 50-60 minutes. It was possible to change the behaviour of 'los2' function such that it can compute the illumination profile of a string of DSM cells at once. This improved the computation time for the illumination profile significantly.

6.2. Optimization

Optimization of any platform is possible on many different levels. This includes smarter methods of data storage, use of faster and smarter coding practices, use of functions, lack of loops, parallel computing etc.

The most basic method of optimizing the MATLAB program is to store data smartly. It is more efficient to generate and store data as a 3D matrix containing multiple sets of 2D arrays directly, than to generate individual set of 2D array and store them independently. Data that is used at multiple instances but is computationally heavy to import and store, is only imported once. It is then stored as different variables to be used by other functions. The DSM data and the geographical information associated with the DSM, is imported together. The elevation data is stored separately and used by functions for calculating view factor, roughness and probability factor. The GIS data is stored separately and used for line-of-sight assessment. For example, view factor is calculated for every DSM cell of every sub-tile. If view factor is calculated for each sub-tile and stored as a separated variable for each hour, it would clutter the workspace. Instead, calculating and storing the view factor for all sub-tiles and storing it as a 3D array is more efficient and more convenient.

It is also advised to pre-allocate the memory for matrices that change size during computation. If the memory for the final size of the array is already reserved, MATLAB requires less computational power overall. Using matrix indexing instead of loops also improves the performance of the platform. This way bigger arrays that change size during computation can be avoided altogether. As opposed to loops, indexing makes use of the parallel computing which improves the computational time of the task, for example, view factor for the entire area of Delft can be computed and stored in a single step using matrix indexing.

Apart from that, parallel computing toolbox from MATLAB was used to reduce the computation speeds where ever loops were inevitable. One of the most computationally intensive task is illumination profile generation. The illumination profile is calculated for every cell of every sub-tile and for every hour. This equates to more than 34 billion operations. As discussed in the previous section, by changing the behavior of los2 to process a row of cells instead, the computation time of the task could be cut in half. Using parallel computing for the rest of the calculation improved the performance of the task significantly. To reduce this computational load and delay, the data generated and stored after using the los2 function was reduced. This was done by removing all the auxiliary variables being generated while using los2. Ultimately, the computation time for generating illumination profile of was reduced from 50-60 minutes to $\approx$ 2 to 2.5 minutes.

7

Results and Discussion

Albedo estimation using the geometric spectral albedo model is influenced by the geometrical arrangement of surfaces, their spectral reflectivity and the composition of irradiation incident on the surface at any given time. These factors individually influence some aspects of the albedo estimation. In most real-life situations, however, these parameters do not change individually; for example, the creation of a building replaces the material of the area from soil to concrete (more accurately, a mixture of different man-made surfaces). However, it is not only the reflectivity that has changed. The geometry of the surface is also affected by the addition of a building. At the same time, shading pattern created by this structure also influences the albedo of the area. Hence albedo of an area has changed, it is likely due to a combination of one or more parameters. Before analyzing the change in albedo for Delft, it is beneficial to study the behaviour and distribution of the parameters that affect the albedo. At first, the temporal coverage of the analysis will be discussed. After that, view factor distribution, roughness, probability distribution, illumination profile, reflectance profile, and chance factors values will be discussed. Finally, albedo maps and albedo variation for all AHN datasets will be discussed and salient observations will be noted.

7.1. Intermediate parameters

AHN3 dataset was readily available from the beginning of the project and it was recorded with a consistent point cloud density. The results discussed in this section are generated for 24th sub-tile in AHN3 dataset. Figure 7.1 depicts the LiDAR point cloud for the 24th sub-tile. Notably, EEMCS is the one of the only tall objects with a height of $\approx$ 100 m. Observing Figure 7.2, it is evident that highest concentration of view factor is localized to the central region of the sub-tile indicated by the bright central spot surrounded by the near uniform blue region. Figure 7.3 represents the zoomed in view of the central region of the sub-tile. Though, the high-rise building of the EEMCS department is tall and occupies a higher view factor than its surrounding area, the building is farther away from the centre of the sub-tile. Thus, its view factor is small compared to the central region. This is consistent with the view factor algebra used for this analysis.

After view factor calculation, the probability distribution for this sub-tile is calculated. Figure 7.4 represents the distribution of probability that each DSM cell is illuminated by the sun and visible from the albedometer. As this probability is a combination of individual probabilities of being illuminated and being visible from the albedometer, higher contribution of one of these probabilities results in a higher overall probability. Evidently, the central region of this sub-tile has an overall higher probability concentration. As seen earlier, the central region of this area doesn't have high average elevation. However, it has a higher probability of being visible from the albedometer because of its close proximity with the sub-tile centre. It can also be noted that, despite of its higher elevation, the high-rise building has lower $P_{ill+vis}$ than its surrounding region as it is has lower probability of being illuminated by the sun at that particular hour. Figure 7.5, on the other hand, represents the probability that the DSM cell is visible from the albedometer. Since this probability is calculated only considering the viewing angle, the distribution of P_{vis} resembles the view factor distribution. The roughness of the 24th sub-tile was calculated as 13.9224. This value was used to calculate both probability distributions.

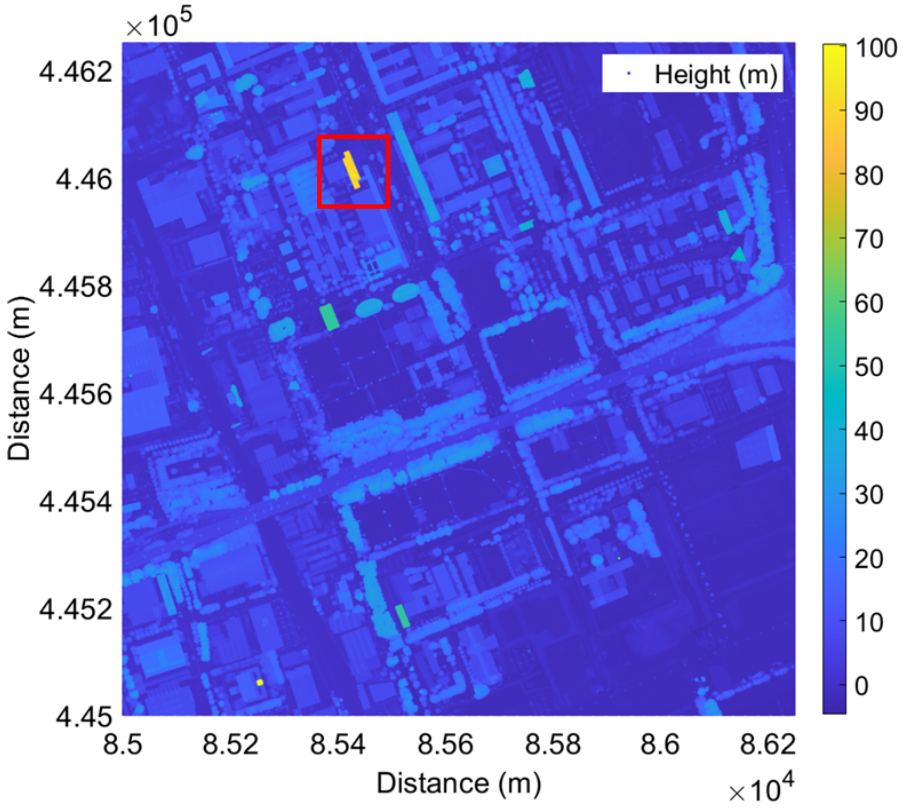

Figure 7.1: Point cloud visualization for the 24th sub-tile in AHN3 dataset. EEMCS high rise building is highlighted in red frame.

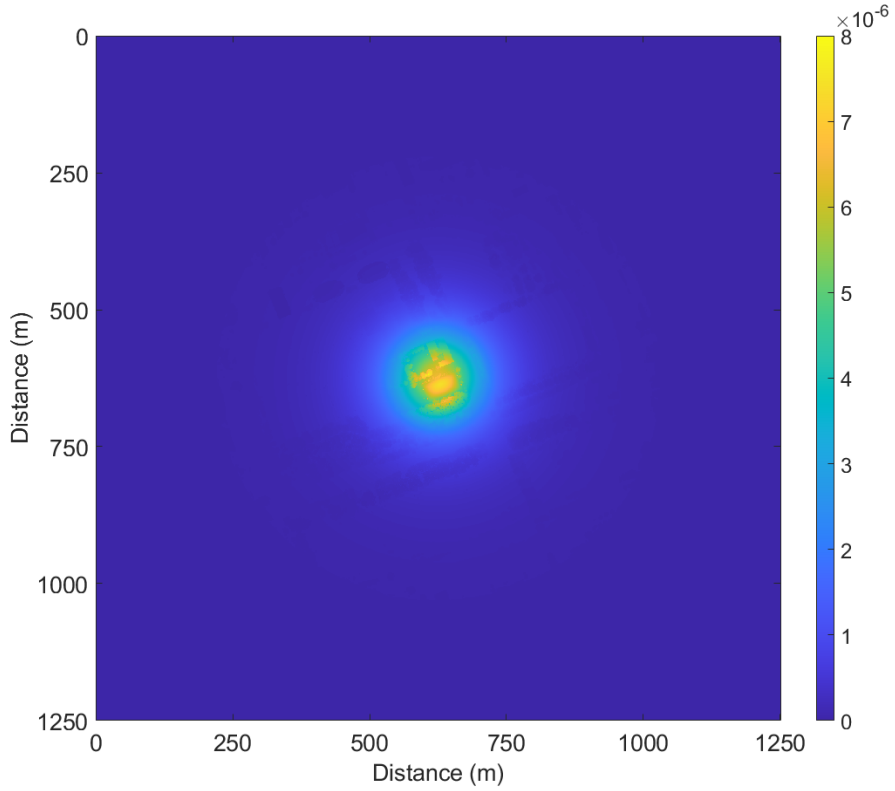

Figure 7.2: View factor distribution for the 24th sub-tile. These values were calculated for height of albedometer at 110m and the roughness of the sub-tile is 13.9224

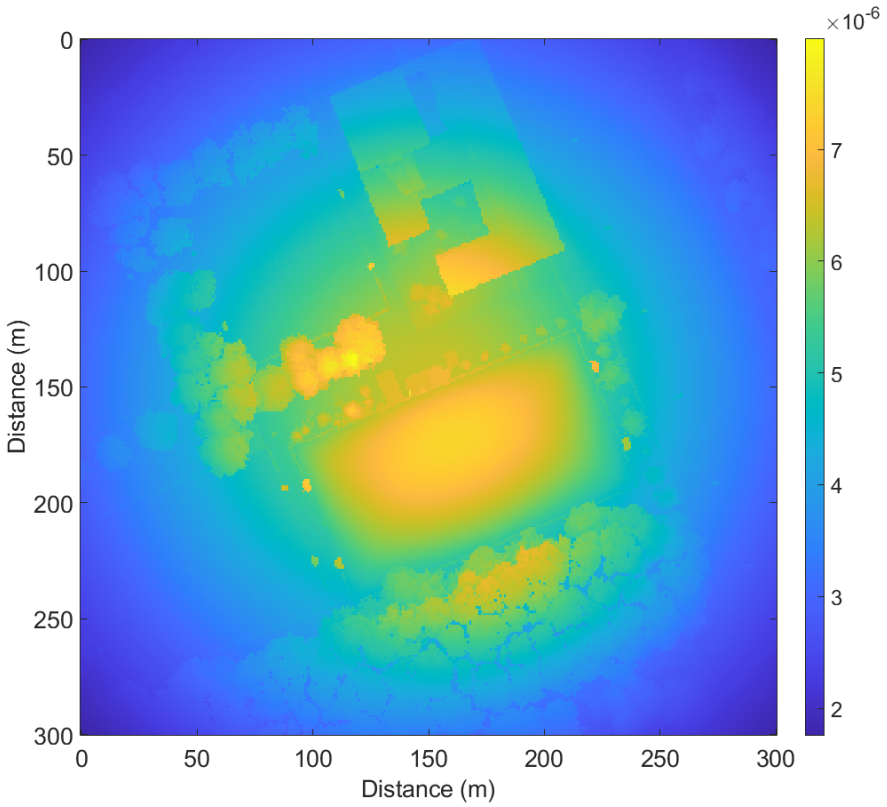

Figure 7.3: Zoomed-in version of view factor distribution for the 24th sub-tile

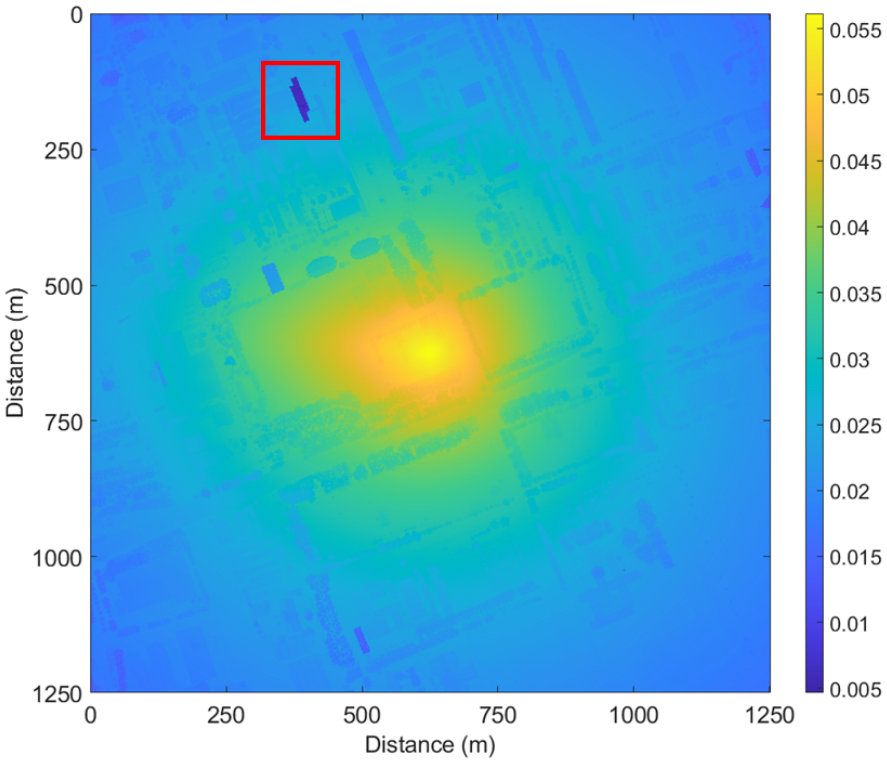

Figure 7.4: $P_{ill+vis}$ distribution for the 24th sub-tile. This distribution is generated for 21st of January 12 PM

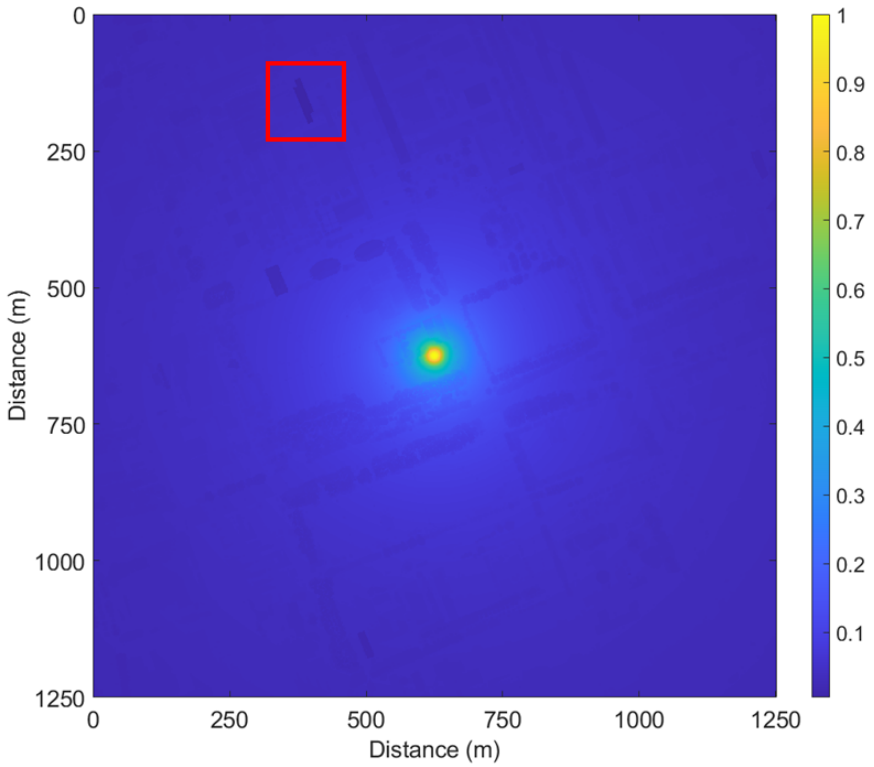

Figure 7.5: P_{vis} distribution for the 24th sub-tile. This distribution is generated for 21st of January 12 PM

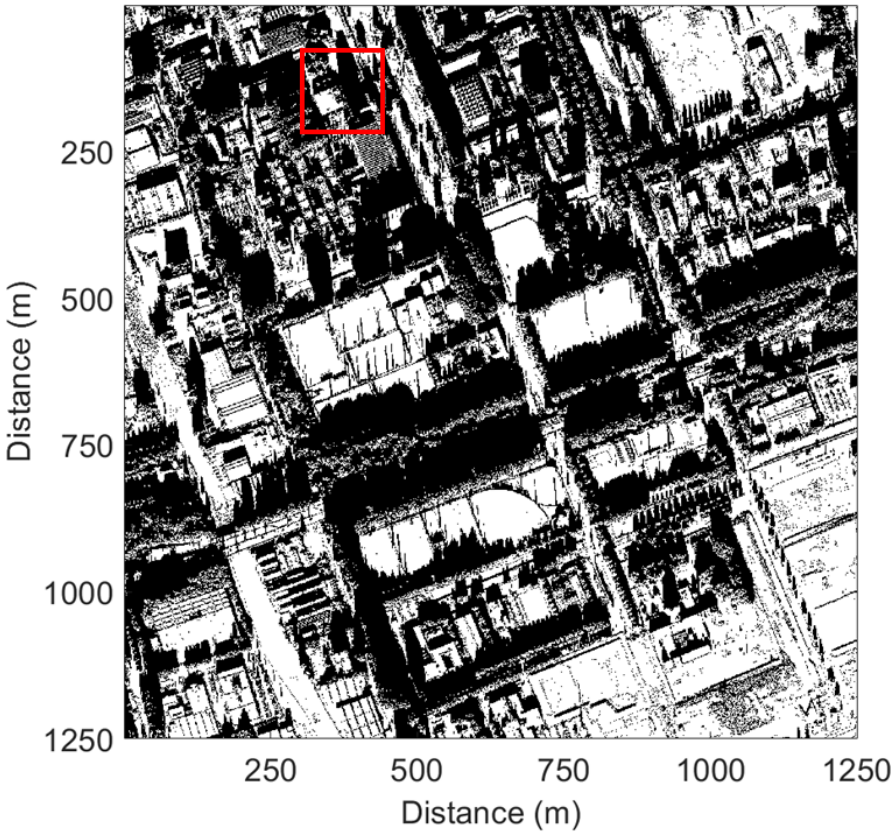

Figure 7.6: Illumination profile for the 24th sub-tile. This distribution is generated for 21st of January 12 PM

Figure 7.6 depicts the illumination profile for the 24th sub-tile. The darker areas of the image represent shaded areas and the white spots indicate that the particular DSM cell is illuminated. Then , view factors, probability factors and the illumination profile are combined to calculate the chance factor C and C'. Chance factor C is calculated as 0.0427 and factor C' is calculated as 0.1246.

7.2. Albedo Maps

Albedo is calculated for each sub-tile, for every hourly value in the year and for all AHN datasets. At first, all hourly albedo values in a year are averaged to calculate yearly average albedo for each sub-tile. Table D.1 shows the average albedo values for all AHN datasets. Then, hourly albedo is normalized with hourly GHI value to calculate irradiance normalized yearly albedo. Table D.3 shows the average irradiance normalized albedo values for all AHN datasets. Yearly average albedo for each sub-tile is plotted to generate a gridded albedomap for the area encompassing Delft. Figure 7.7, Figure 7.8, Figure 7.9, Figure 7.10 represent the four albedomaps generated for AHN1, AHN2, AHN3 and AHN4 datasets respectively. Comparing the albedomaps from AHN1 dataset to AHN4 dataset, it is observed that AHN1 dataset shows considerably higher albedo than AHN2, AHN3 and AHN4 datasets. The maximum albedo recorded for AHN1 was 0.269 for the 34th sub-tile while 0.245 was the minimum recorded albedo for the 19th sub-tile. The maximum albedo recorded was 0.153 for 14th sub-tile for AHN2, was 0.159 for the 14th sub-tile for AHN3 and was 0.164 for the 31st sub-tile for AHN4 datasets respectively. the minimum albedo was 0.076 for 26th sub-tile for AHN2, was 0.087 for the 26th sub-tile for AHN3 and was 0.085 for the 27th sub-tile for AHN4 datasets respectively. As, AHN1 dataset has low fidelity even at low resolution, the albedo results obtained based on this dataset also have lower fidelity. Thus, it was decided to not consider AHN1 results directly for the comparative analysis.

With the urban landscape of changing steadily for the past two decades, change in average albedo values for all the sub-tile can be noted from Figure 7.7, Figure 7.8, Figure 7.9, Figure 7.10. Change in albedo values is influenced by a combination of variations in geometry, materials and incident irradiance. Currently, the resolution of albedomap $1250\,m \times 1250\,m$. This resolution is governed by the size of the sub-tile. As the height of the albedometer influenced the view factor algebra which in turn drives the size of the sub-tiles. To improve the resolution of the albedomap generated, the height of the view factor needs to be lower.

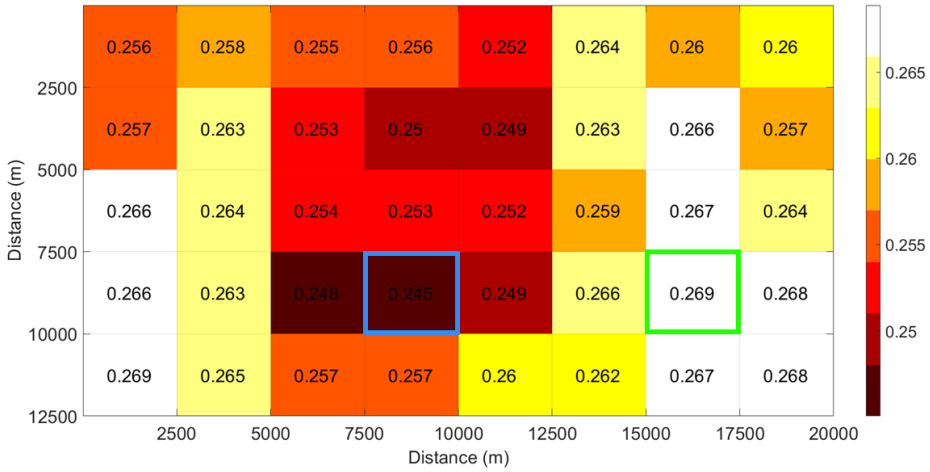

Figure 7.7: AHN1 average yearly albedo map for Delft. Green and Blue frames indicate maxima and minima respectively.

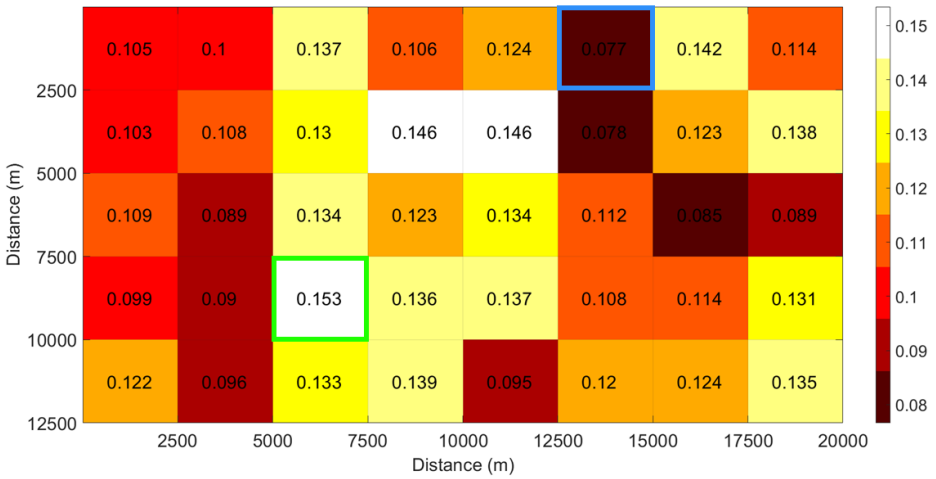

Figure 7.8: AHN2 average yearly albedo map for Delft. Green and Blue frames indicate maxima and minima respectively.

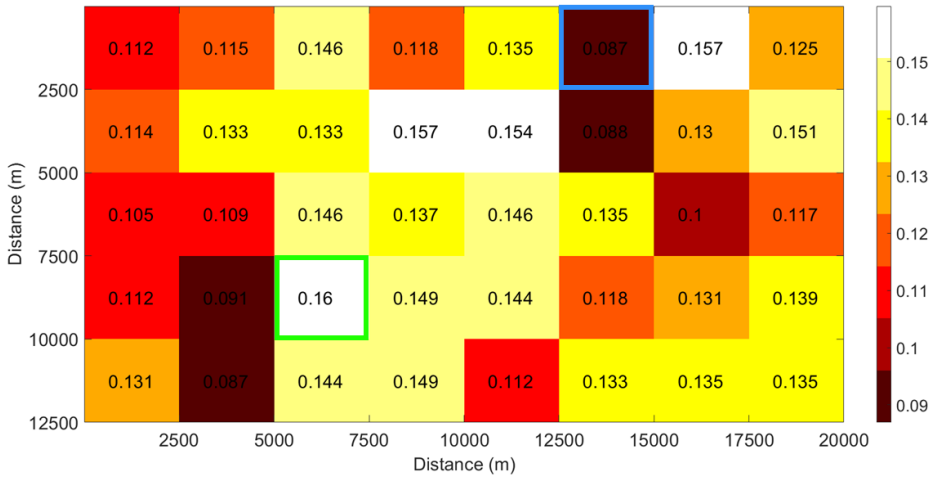

Figure 7.9: AHN3 average yearly albedo map for Delft. Green and Blue frames indicate maxima and minima respectively.

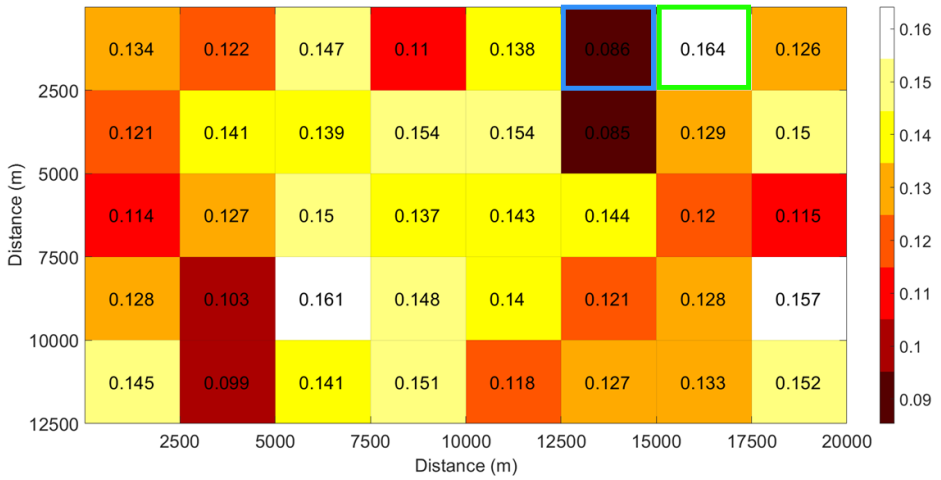

Figure 7.10: AHN4 average yearly albedo map for Delft. Green and Blue frames indicate maxima and minima respectively.

Albedomap generated based on AHN3 is superimposed on the geographical map of Delft obtained from Google Earth Pro and it is depicted in Figure 7.11.

Figure 7.11: Albedomap of yearly average albedo superimposed on the geographical map of Delft. Albedomap is generated for AHN3

7.3. Roughness vs albedo

As urban morphology changes with location and through the course of time, a suitable parameter is needed to quantify this change in morphology. One way to represent the 'urban fabric' is to create a reflectance profile of the investigated area where each index contains the reflectance value corresponding to its material. However, the reflectance profile does not reveal enough information about the geometry of surfaces. Apart from that, the reflectance profile of the same area can change between seasons and it also fluctuates during the day with the changing amount of incident irradiation. Hence, the reflectance profile is not a fair metric for quantifying urban areas.

The geometry of the area, specifically, the roughness 'r' can be used as a metric to quantify urban morphology, as geometry of an area shows gradual change within a span of a few years of urban development. Hence the values are much less susceptible to abrupt changes. Specifically, change in roughness 'r' of the area is an indicator of any change in the geometry of the area. Figure 7.12, Figure 7.13 and Figure 7.14 can be referred to compare the average albedo with the roughness of different sub-tiles. It is generally observed that a lower roughness value corresponds with higher average albedo value for the represented sub-tile. A lower roughness value indicates that the area does not have high spatial variations such as open fields. farmlands etc. Hence roughness can be used as a tool for planning urban areas and strategically developing the area such that its roughness does not increase too much, causing drop in albedo.

7.4. Reflectance vs albedo

In one of the previous iterations of building algorithm and the MATLAB platform, it was decided to calculate reflectance value of materials only using the reference AM1.5 spectrum modelled using SMARTS2. However, solar irradiation is not uniformly received throughout the planet and air mass through which the irradiation passes is also fluctuating. Thus, spectral GHI hourly data for a year for the geographical co-ordinates encompassing the Netherlands were retrieved. This data was then normalized with the hourly GHI data from Meteonorm as expressed in Equation 4.1. The spectral GHI data is then used instead of reference AM1.5 spectrum to calculate reflectance values from spectral reflectivity. Figure 7.15 and Figure 7.16 represent the comparison between the spectral GHI data used and albedo values ob-

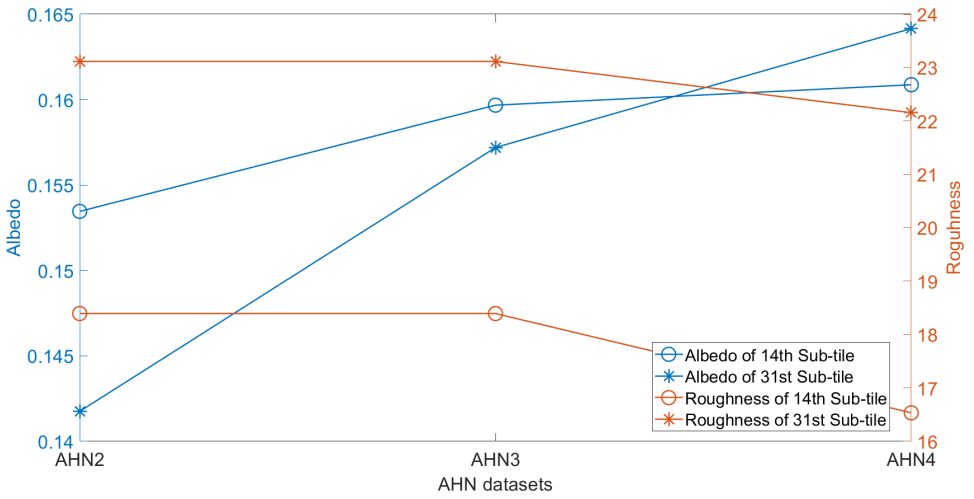

Figure 7.12: Albedo vs Roughness plot for 14th and 31st sub-tile. These two sub-tiles recorded the maximum albedo values for AHN2, AHN3 and AHN4 datasets.

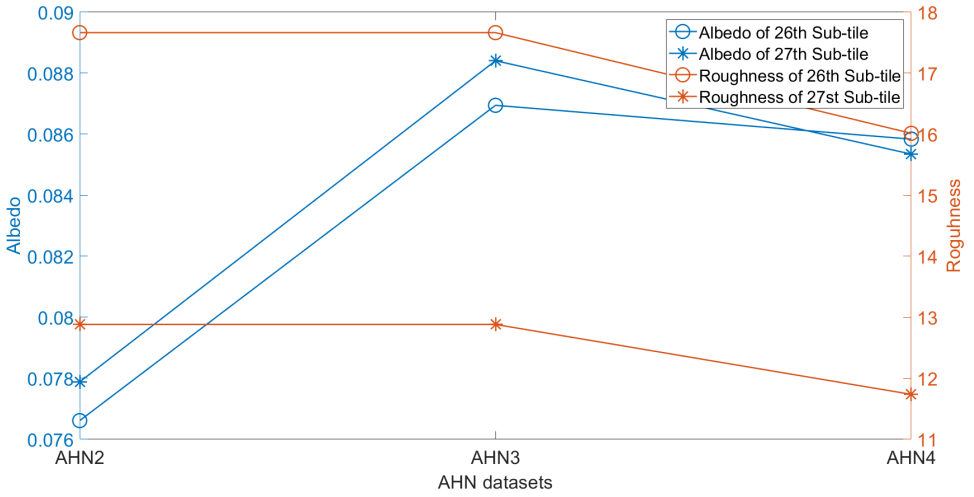

Figure 7.13: Albedo vs Roughness plot for 26th and 27th sub-tile. These two sub-tiles recorded the minimum albedo values for AHN2, AHN3 and AHN4 datasets.

tained in an earlier iteration vs the final iteration. As spectral GHI has reduced in the final iteration, range of reflectance values has also dropped. The reflectance values for concrete, soil, vegetation and water the previous iteration were 0.274, 0.28, 0.319 and 0.026 respectively. The reflectance values for concrete, soil, vegetation and water dropped to 0.265, 0.275, 0.30, 0.025 in the final iteration. It can be observed that the range of albedo values has changed; however, albedo values follow the same variation pattern throughout the year. In both scenarios, dataset selected is AHN3 which indicates that the geometry has not changed between the two scenarios. Thus, it can be inferred that the range of albedo values is influenced by the range of reflectance values. On the other hand, it can also be inferred that variation pattern of albedo is influenced by the geometry of the area. As incident irradiation influences the albedo and the reflectance of materials, it contributes to both the range of albedo values and its variation pattern. Hence the change in albedo for Delft was a holistic combination of change in geometry and reflectance values. The inclusion of more nuanced material classes such as pavements, roads, grass, roofing material etc. can improve the accuracy of albedo values and bring the albedo estimation scenario closer to the reality.

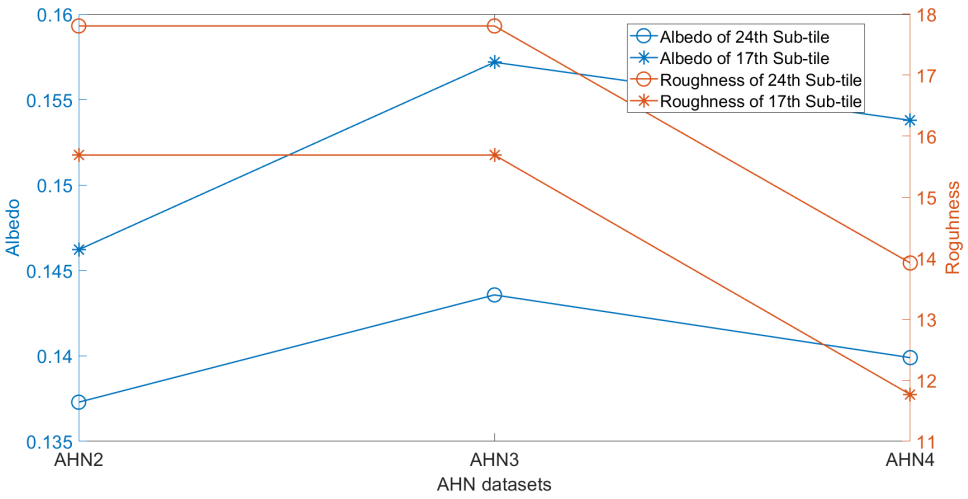

Figure 7.14: Albedo vs Roughness plot for 24th and 17th sub-tile. 24th sub-tile encompasses part of the TU campus and 17th sub-tile encompasses the Delft city centre

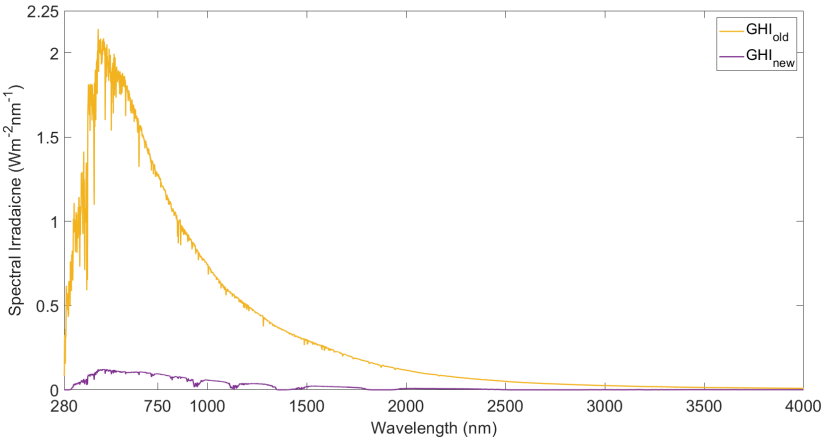

Figure 7.15: Comparison of spectral GHI data used in two different scenarios for reflectance calculation. The spectral GHI data depicted as GHI_{new} is calculated for 21st January at 12:00 PM

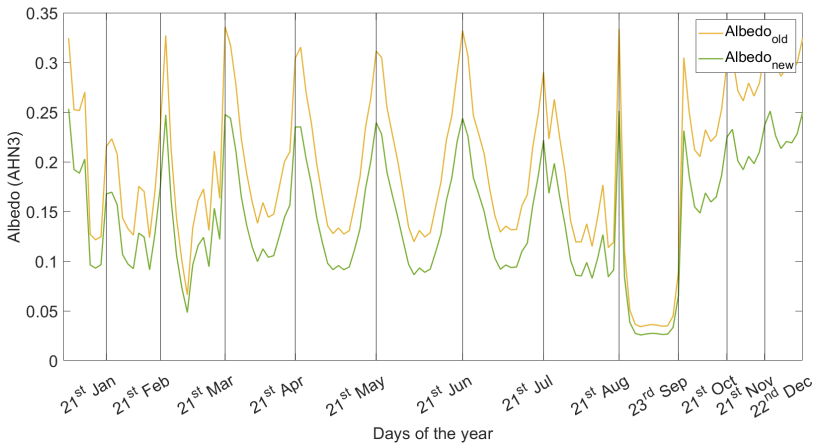

Figure 7.16: Comparison of albedo values obtained from two different scenarios

7.5. Albedo vs Solar altitude

As discussed in section 2.1, albedo depends varies inversely with the solar altitude. Figure 7.17 also depicts similar relation between albedo and solar altitude.

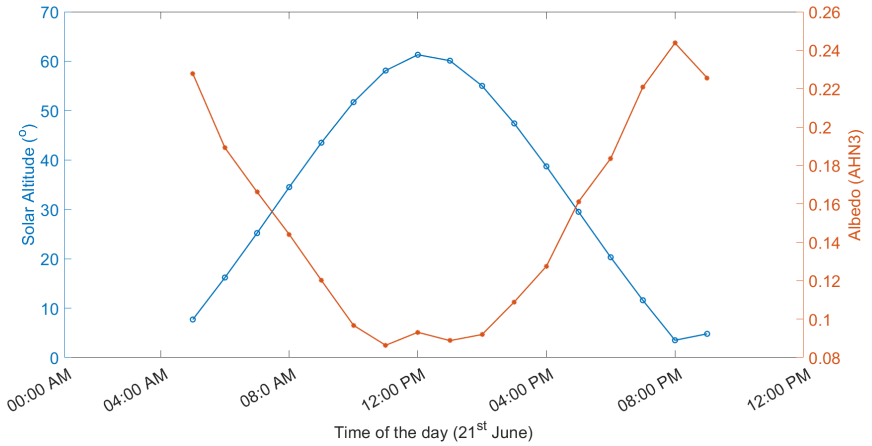

Figure 7.17: Albedo variation vs solar altitude variation for the 24th sub-tile in AHN3 dataset on 21st of June

8

Future outlook

After discussing the results in the previous chapter, three major areas of modifications/improvements are suggested in this chapter. These include improvement in the resolution of albedomap, automatic material allocation, improvement in albedo accuracy and finally, improvement in computation speed.

8.1. Variable height of albedometer

Currently, view factor calculation considers constant height of albedometer throughout the area of Delft for all the datasets. As height of the albedometer drives the size of the sub-tile and the resolution of the albedomap, resolution of albedomap is same throughout the area encompassing Delft. Currently, the albedomap depicted as discrete albedo values for each sub-tile in the Figure 7.8 to Figure 7.10. Areas within each other's proximity should logically have similar albedo values. But, it can be observed that, albedo values undergo sudden changes between neighbouring sub-tiles. This can be observed for the 9^{th} sub-tile with albedo of 0.09 and 14^{th} sub-tile with albedo of 0.154. This issue can be addressed by improving the resolution of the albedomap so that a more continuous albedomap for Delft can be generated.

The algorithm for implementing variable albedometer height includes optimization for segmenting DSM data into variably sized sub-tiles. Alternately, the view factor algebra can also be modified by making the shape and dimensions of the sub-tile flexible, for example; currently, the sub-tiles are squares. If the sub-tiles can also be formed as rectangles, it can change the sub-tile distribution for the area. This might require additional computational resources and time. In such a case, the height of the albedometer can be kept constant for some parts of the area, while some parts can utilize variable albedometer height.

8.2. Automatic material allocation

Currently, identification of surfaces with different materials and the division of DSM into the respective material classes is performed using MATLAB functions and GIS softwares like ArcGIS pro. The process is limited by the quality of the LiDAR data and the versatility of the GIS software. However, it is possible to automatically divide the LiDAR data into more nuanced material classes such as roads, pavements, roofing, grass, metallic surfaces, glass etc. Authors in [53] have implemented automatic detection algorithm for roads and authors in [54] have implemented automatic detection of building roofs using LiDAR data. Alternatively, aerial imagery can be used with AI based detection algorithms to detect surfaces with different material.

8.3. Improvement in computational speed

One of the most computationally intensive part of the algorithm is the illumination profile generation. Instead of generating an illumination profile when required by the algorithm, it can be calculated beforehand and the illumination profile on an area can be retrieved directly. An alternative methodology can be implemented to plot and visualize the skyline profile for every DSM cell beforehand. Then solar position can be superimposed on this skyline profile to check if the line-of-sight is blocked for the DSM

cell. After repeating this process for every hourly value in the year, a dataset of illumination profiles for every DSM cell and every hourly values is created.

Apart from that, use of MATLAB essentially comes with limitations of its own. MATLAB can process the data sequentially either by reserving the RAM as storage memory or by running loops to reduce use of RAM. Use of matrix indexing has limitations as bigger arrays can not be created due to limited RAM of most computational devices. On the other hand, use of loops does not require too much RAM, but loops are slower as they don't make use of parallel processing. GPU accelerated parallel computing can be implemented to counter the limitations of MATLAB. Alternatively, the platform can be moved to Python for faster processing.

9

Conclusion

The objective of this research was to analyse the change in albedo over the course of two decades of urban development in Delft. To accomplish this, a software platform was developed on MATLAB based on the GSA model. Open source LiDAR data in the Netherlands was used to measure and quantify urban development in Delft. Along with this, Irradiance data from Meteonorm and NREL and Spectral reflectivity data from ASTER library were used to calculate and plot albedo values for a different version of the LiDAR dataset available. Finally, albedo results were discussed, and recommendations about possible modifications and improvements were provided. Some conclusive remarks will be given about the effectiveness of the platform and the possible use cases of this platform.

The albedo results generated from the platform were found to comply with the previous observations and interpretations of albedo estimation. The roughness of the area was rightfully selected as the parameter to quantify modern urban morphology. The relation between the range of albedo and the range of reflectance values was correctly established as well. The platform is able to estimate albedo values for the area of Delft with a spatial resolution of $1250\ m \times 1250\ m$, a temporal resolution of 1 hour and the temporal coverage of 1 day per month. Though the temporal coverage of the platform is not considerably wide, the spatial resolution of the platform is significant when compared to the other satellite-based albedo retrieval methods. The highest possible resolution local albedo estimation of the platform is $22.7\ m \times 22.7\ m$ considering an albedometer height of 1.7-2 m. The platform was successfully implemented to plot gridded albedomaps over the area encompassing Delft.

After the successful implementation of this platform for the area of Delft, this platform can be deployed for albedo estimation of the rest of the Netherlands. The availability of LiDAR data or lack thereof for the given location limits its implementation everywhere in the world. A scenario is envisioned for this platform, which can be used by urban developers, planners and PV system engineers to estimate the local albedo of the area. Planners can also feed the platform with a custom-generated point cloud of planned urban development to analyse its implications on albedo. Though it seems ambitious at this point in time, the recommendations provided will help the platform get closer to this goal.

Bibliography

[1] United Nations Conference for Trade and Development. *UNCTAD HANDBOOK OF STATISTICS*. 2021. URL: https://hbs.unctad.org/total-and-urban-population/.

[2] Hannah Ritchie and Max Roser. “Urbanization”. In: *Our World in Data* (2018). URL: https://ourworldindata.org/urbanization.

[3] *Then vs now: The dramatic change in the skyline of 10 worldwide major cities*. July 2021. URL: https://www.arch2o.com/vs-now-dramatic-change-skyline-10-worldwide-major-cities/.

[4] Kasha Patel. *Urban growth of New Delhi*. Sept. 2018. URL: https://earthobservatory.nasa.gov/images/92813/urban-growth-of-new-delhi.

[5] Lauren Dauphin. *Urban growth of New Delhi*. Sept. 2018. URL: https://earthobservatory.nasa.gov/images/92813/urban-growth-of-new-delhi.

[6] UNEP. *Cities and climate change*. URL: https://www.unep.org/explore-topics/resource-efficiency/what-we-do/cities/cities-and-climate-change#:~:text=At%5C%20the%5C%20same%5C%20time%5C%2C%5C%20cities,being%5C%20among%5C%20the%5C%20largest%5C%20contributors..

[7] Daniel Moran et al. “Carbon footprints of 13 000 cities”. In: *Environmental Research Letters* 13.6 (June 2018), p. 064041. DOI: 10.1088/1748-9326/aac72a. URL: https://doi.org/10.1088/1748-9326/aac72a.

[8] Sabiha Sultana and A.N.V. Satyanarayana. “Urban heat island intensity during winter over metropolitan cities of India using remote-sensing techniques: impact of urbanization”. In: *International Journal of Remote Sensing* 39.20 (2018), pp. 6692–6730. DOI: 10.1080/01431161.2018.1466072. eprint: https://doi.org/10.1080/01431161.2018.1466072. URL: https://doi.org/10.1080/01431161.2018.1466072.

[9] *Albedometers*. URL: https://www.kippzonen.com/ProductGroup/10/Albedometers.

[10] ISO. *Solar energy-Pyranometers-Recommended practice for use(ISO/TR9901)*. Aug. 2021.

[11] Dennis L. Hartmann. “Chapter 2 - The Global Energy Balance”. In: *Global Physical Climatology (Second Edition)*. Ed. by Dennis L. Hartmann. Second Edition. Boston: Elsevier, 2016, pp. 25–48. ISBN: 978-0-12-328531-7. DOI: https://doi.org/10.1016/B978-0-12-328531-7.00002-5. URL: https://www.sciencedirect.com/science/article/pii/B9780123285317000025.

[12] Wolfgang Lucht, Crystal Barker Schaaf, and Alan H Strahler. “An algorithm for the retrieval of albedo from space using semiempirical BRDF models”. In: *IEEE Transactions on Geoscience and Remote sensing* 38.2 (2000), pp. 977–998.

[13] Crystal B Schaaf et al. “First operational BRDF, albedo nadir reflectance products from MODIS”. In: *Remote sensing of Environment* 83.1-2 (2002), pp. 135–148.

[14] UCAR. *Center for Science Education*. URL: https://scied.ucar.edu/learning-zone/how-climate-works/albedo-and-climate.

[15] *Albedo measurements*. URL: http://www.climatedata.info/forcing/albedo/.

[16] Hashem Akbari, H Damon Matthews, and Donny Seto. “The long-term effect of increasing the albedo of urban areas”. In: *Environmental Research Letters* 7.2 (2012), p. 024004.

[17] Hashem Akbari, Surabi Menon, and Arthur Rosenfeld. “Global cooling: Increasing world-wide urban albedos to offset CO 2”. In: *Climatic Change* 94 (3-4 June 2009), pp. 275–286. ISSN: 01650009. DOI: 10.1007/s10584-008-9515-9.

[18] Ivan Muñoz, Pablo Campra, and Amadeo R Fernández-Alba. “Including CO 2-emission equivalence of changes in land surface albedo in life cycle assessment. Methodology and case study on greenhouse agriculture”. In: *International Journal Life Cycle Assessment* 15 (June 2010), pp. 672–681. DOI: 10.1007/s11367-010-0202-5.

[19] S. B. Idso et al. “The Dependence of Bare Soil Albedo on Soil Water Content”. In: *Journal of Applied Meteorology* 14.1 (1975), pp. 109–113. ISSN: 0021-8952. DOI: 10.1175/1520-0450(1975)014<0109:tdobsa>2.0.co;2.

[20] Keith L. Bristow. “On solving the surface energy balance equation for surface temperature”. In: *Agricultural and Forest Meteorology* 39.1 (1987), pp. 49–54. ISSN: 0168-1923. DOI: https://doi.org/10.1016/0168-1923(87)90015-3. URL: https://www.sciencedirect.com/science/article/pii/0168192387900153.

[21] Hesan Ziar et al. “A comprehensive albedo model for solar energy applications: Geometric spectral albedo”. In: *Applied Energy* 255 (Dec. 2019). ISSN: 03062619. DOI: 10.1016/j.apenergy.2019.113867.

[22] Arno Smets et al. *Solar Energy: The physics and engineering of photovoltaic conversion, technologies and systems*. English. UIT Cambridge Limited, 2016. ISBN: 978-1-906860-32-5.

[23] Copernicus. July 2022. URL: https://cds.climate.copernicus.eu/cdsapp#!/dataset/satellite-albedo?tab=overview.

[24] TEMIS. July 2022. URL: https://www.temis.nl/surface/albedo/.

[25] LG Tilstra et al. “Surface reflectivity climatologies from UV to NIR determined from Earth observations by GOME-2 and SCIAMACHY”. In: *Journal of Geophysical Research: Atmospheres* 122.7 (2017), pp. 4084–4111.

[26] NEO. 2022. URL: https://neo.gsfc.nasa.gov/view.php?datasetId=MCD43C3_M_BSA.

[27] Ying Qu et al. “Direct-estimation algorithm for mapping daily land-surface broadband albedo from MODIS data”. In: *IEEE Transactions on Geoscience and Remote Sensing* 52.2 (2013), pp. 907–919.

[28] Shunlin Liang, Alan H Strahler, and Charles Walthall. “Retrieval of land surface albedo from satellite observations: A simulation study”. In: *Journal of Applied meteorology* 38.6 (1999), pp. 712–725.

[29] Benjamin Y.H. Liu and Richard C. Jordan. “The long-term average performance of flat-plate solar-energy collectors: With design data for the U.S., its outlying possessions and Canada”. In: *Solar Energy* 7.2 (1963), pp. 53–74. ISSN: 0038-092X. DOI: https://doi.org/10.1016/0038-092X(63)90006-9. URL: https://www.sciencedirect.com/science/article/pii/0038092X63900069.

[30] Pierre Ineichen, Richard Perez, and Robert Seals. “The importance of correct albedo determination for adequately modeling energy received by tilted surfaces”. In: *Solar Energy* 39.4 (1987), pp. 301–305. ISSN: 0038-092X. DOI: https://doi.org/10.1016/S0038-092X(87)80016-6. URL: https://www.sciencedirect.com/science/article/pii/%5C%5CS0038092X87800166.

[31] B.E. Psiloglou and H.D. Kambezidis. “Estimation of the ground albedo for the Athens area, Greece”. In: *Journal of Atmospheric and Solar-Terrestrial Physics* 71.8 (2009), pp. 943–954. ISSN: 1364-6826. DOI: https://doi.org/10.1016/j.jastp.2009.03.017. URL: https://www.sciencedirect.com/science/article/pii/S1364682609000662.

[32] Y Kotak et al. “Investigating the impact of ground albedo on the performance of PV systems”. In: *Proceedings of the CIBSE Technical Symposium, London, UK*. 2015, pp. 16–17.

[33] Pierre Ineichen, Olivier Guisan, and Richard Perez. “Ground-reflected radiation and albedo”. In: *Solar Energy* 44.4 (1990), pp. 207–214. ISSN: 0038-092X. DOI: https://doi.org/10.1016/0038-092X(90)90149-7. URL: https://www.sciencedirect.com/science/article/pii/0038092X90901497.

[34] Christian Gueymard. “Mathematically integrable parameterization of clear-sky beam and global irradiances and its use in daily irradiation applications”. In: *Solar Energy* 50 (5 1993). ISSN: 0038092X. DOI: 10.1016/0038-092X(93)90059-W.

[35] John E. Hay. “Calculating solar radiation for inclined surfaces: Practical approaches”. In: *Renewable Energy* 3 (4-5 1993). ISSN: 09601481. DOI: 10.1016/0960-1481(93)90104-O.

[36] Matthew Lave et al. “Evaluation of global horizontal irradiance to plane-of-array irradiance models at locations across the United States”. In: *IEEE Journal of Photovoltaics* 5 (2 2015). ISSN: 21563381. DOI: 10.1109/JPHOTOV.2015.2392938.

[37] Lawrence C. Nkemdirim. “A Note on the Albedo of Surfaces”. In: *Journal of Applied Meteorology* 11 (5 1972). ISSN: 0021-8952. DOI: 10.1175/1520-0450(1972)011<0867:anotao>2.0.co;2.

[38] Christian Gueymard. “An anisotropic solar irradiance model for tilted surfaces and its comparison with selected engineering algorithms”. In: *Solar Energy* 38 (5 1987). ISSN: 0038092X. DOI: 10.1016/0038-092X(87)90009-0.

[39] Ralph C. Temps and K. L. Coulson. “Solar radiation incident upon slopes of different orientations”. In: *Solar Energy* 19 (2 1977). ISSN: 0038092X. DOI: 10.1016/0038-092X(77)90056-1.

[40] University of Rochester. *Understanding view factors*. 2013. URL: http://www2.me.rochester.edu/courses/ME204/nx_help/index.html#uid:id632026.

[41] U Gross, K Spindler, and E Hahne. “Shapefactor-equations for radiation heat transfer between plane rectangular surfaces of arbitrary position and size with parallel boundaries”. In: *Letters in heat and mass transfer* 8.3 (1981), pp. 219–227.

[42] E S Gadelmawla et al. “Roughness parameters”. In: *Journal of Materials Processing Technology* 123 (Jan. 2002), pp. 133–145.

[43] Bram Van Ginneken, Marigo Stavridi, and Jan J Koenderink. “Diffuse and specular reflectance from rough surfaces”. In: *Applied Optics* 37 (1 Jan. 1998), pp. 130–139.

[44] Nikita Marwaha and Elizabeth Duffy. *Everything you need to know about digital elevation models (Dems), Digital Surface Models (dsms), and Digital Terrain Models (dtms)*. Mar. 2021. URL: https://up42.com/blog/tech/everything-you-need-to-know-about-digital-elevation-models-dem-digital.

[45] *NELIDAR Specifications for Cape Cod*. URL: https://www.nrcs.usda.gov/wps/portal/nrcs/detail/ma/technical/?cid=nrcs144p2_013976.

[46] Demetrios Gatziolis and Hans-Erik Andersen. “A guide to LIDAR data acquisition and processing for the forests of the Pacific Northwest.” In: *Gen. Tech. Rep. PNW-GTR-768. Portland, OR: US Department of Agriculture, Forest Service, Pacific Northwest Research Station. 32 p* 768 (2008).

[47] AHN Ahn. *Het Verhaal van Ahn*. Dec. 2020. URL: https://www.ahn.nl/het-verhaal-van-ahn.

[48] Jeroen Leusink. *AHN4 in drie jaar! … en daarna?* Apr. 2019. URL: https://www.ahn.nl/_flysystem/media/ahn4_in_drie_jaar._en_daarna_-_jeroen_leusink_hwh.pdf.

[49] John R. Howell. *Section C factors from finite areas to finite areas*. 2010. URL: https://web.engr.uky.edu/rtl/Catalog/sectionc/C-12.html.

[50] Christian A Gueymard. “Parameterized transmittance model for direct beam and circumsolar spectral irradiance”. In: *Solar Energy* 71.5 (2001), pp. 325–346.

[51] Christian A Gueymard. “The sun’s total and spectral irradiance for solar energy applications and solar radiation models”. In: *Solar energy* 76.4 (2004), pp. 423–453.

[52] ASTM. “(ASTM) G-173 Reference Air Mass 1.5 Spectra”. In: (Jan. 2003). URL: https://www.nrel.gov/grid/solar-resource/spectra-am1.5.html.

[53] Simon Clode, Peter J Kootsookos, and Franz Rottensteiner. “The automatic extraction of roads from LIDAR data”. In: ISPRS. 2004.

[54] Mohammad Awrangjeb and Clive S Fraser. “Automatic segmentation of raw LiDAR data for extraction of building roofs”. In: *Remote Sensing* 6.5 (2014), pp. 3716–3751.

A

LiDAR Data

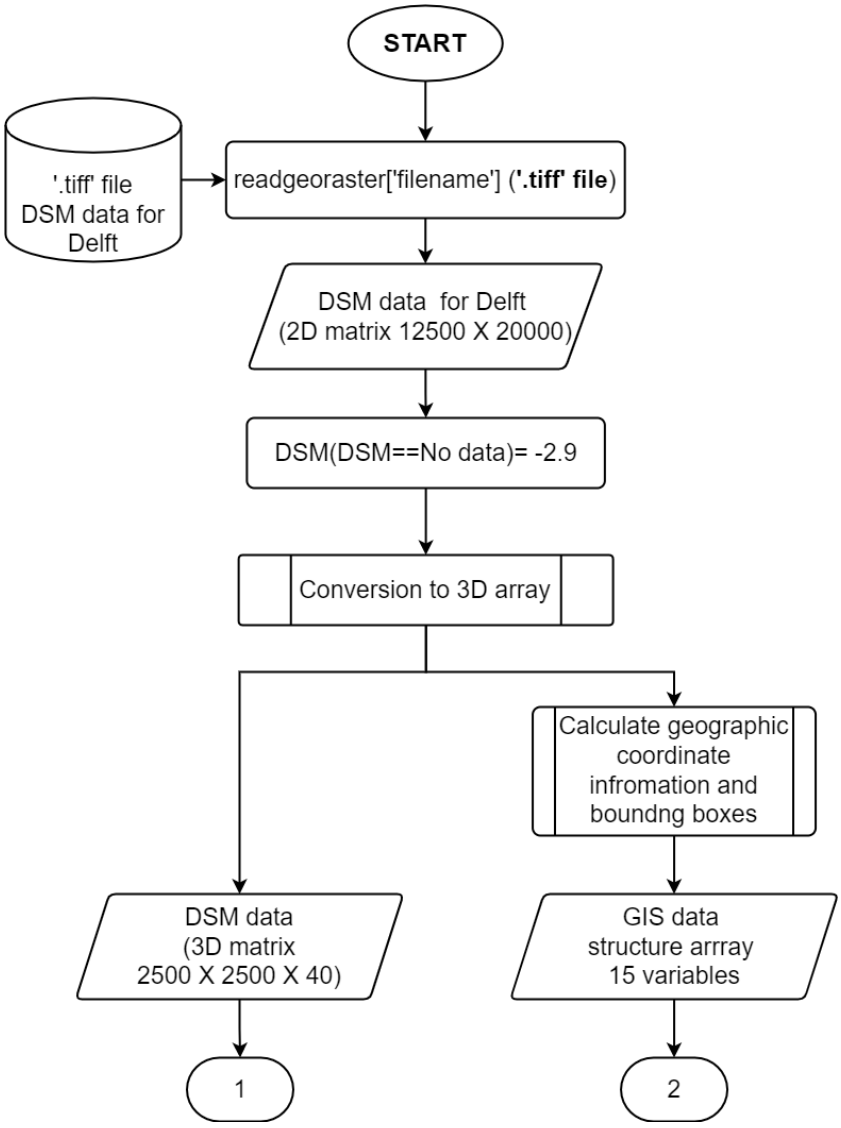

Figure A.1: LiDAR data acquisition

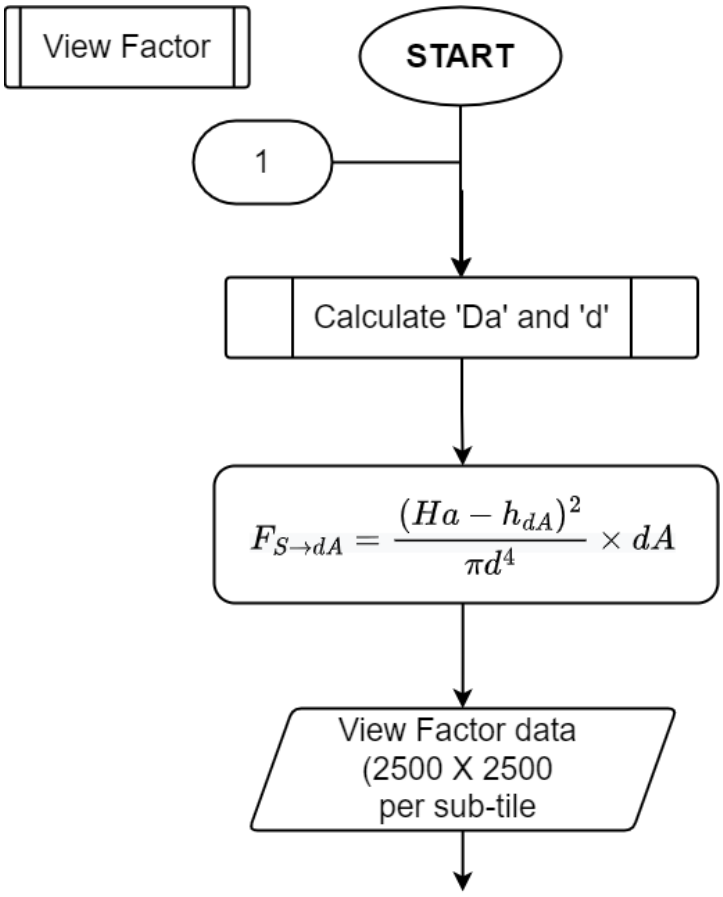

Figure A.2: View Factor sub-routine

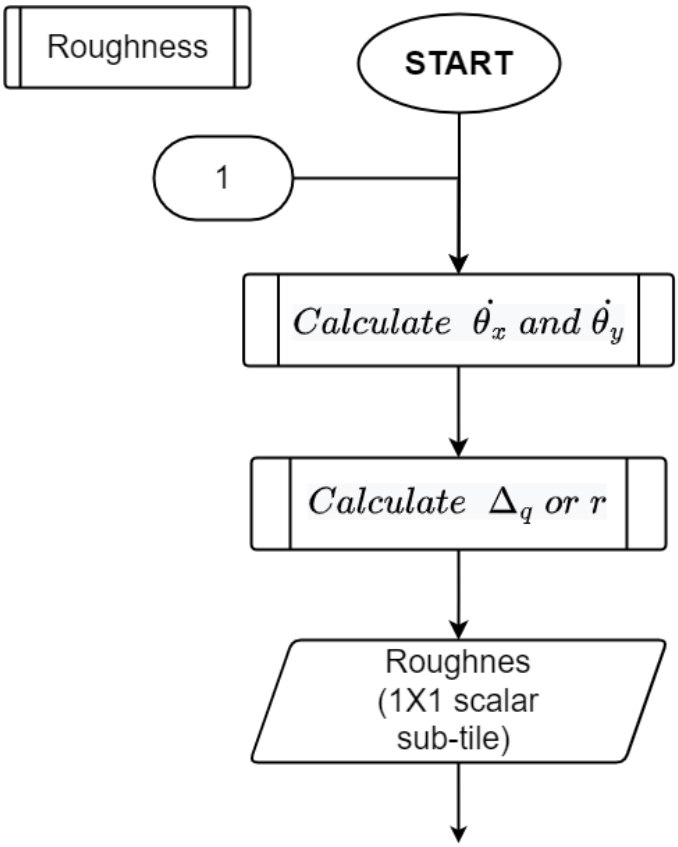

Figure A.3: Roughness sub-routine

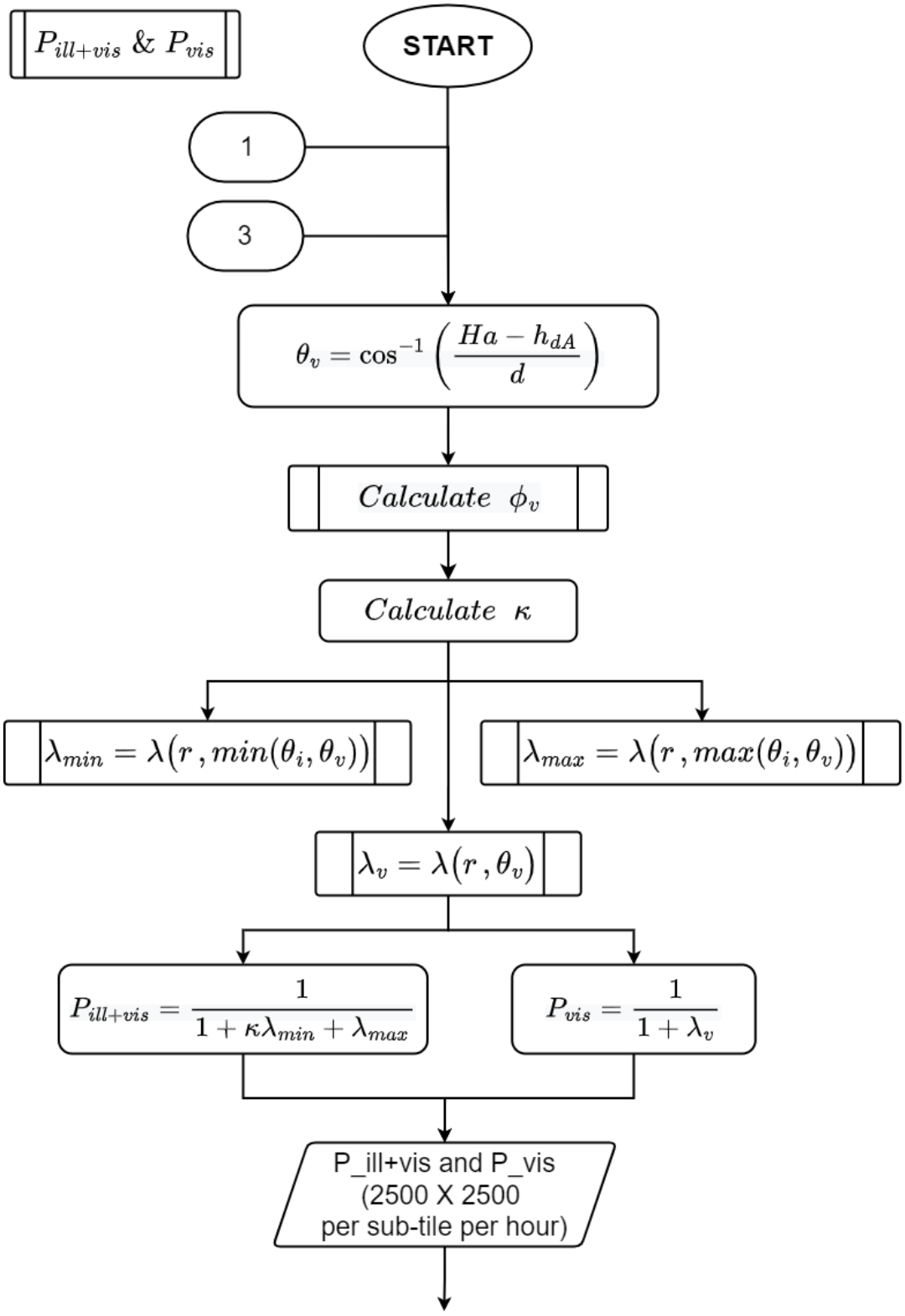

Figure A.4: Probability factor sub-routine

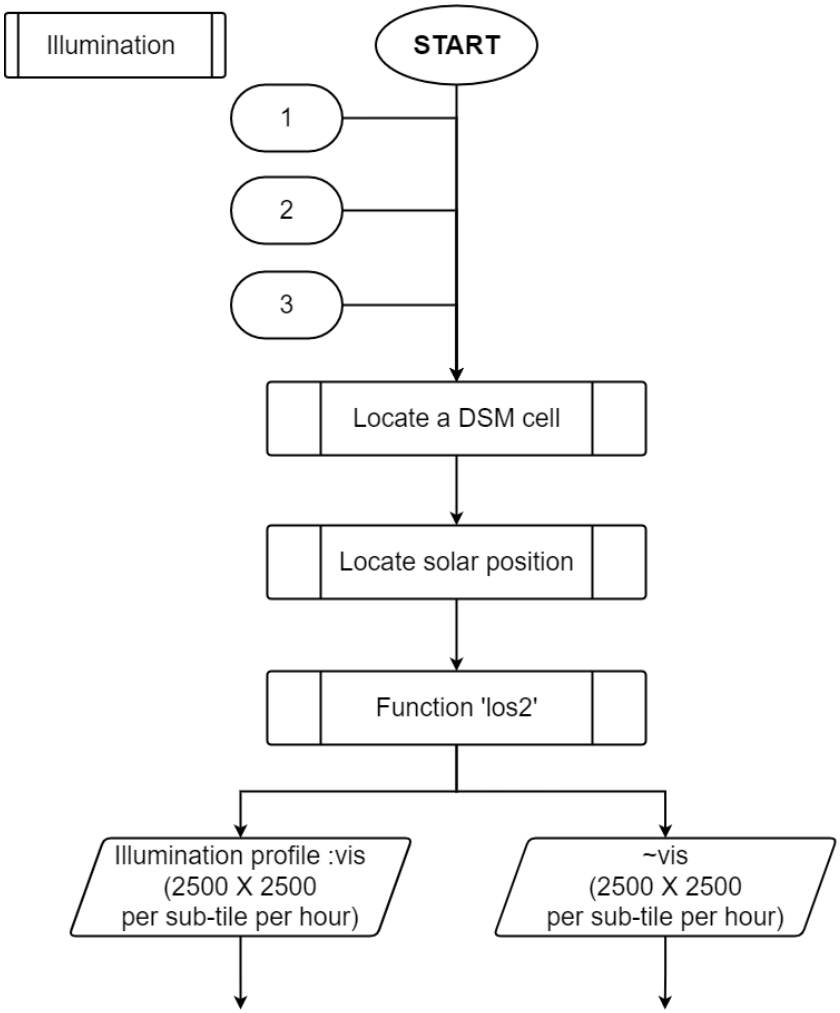

Figure A.5: Illumination profile sub-routine

B

Reflectance Data

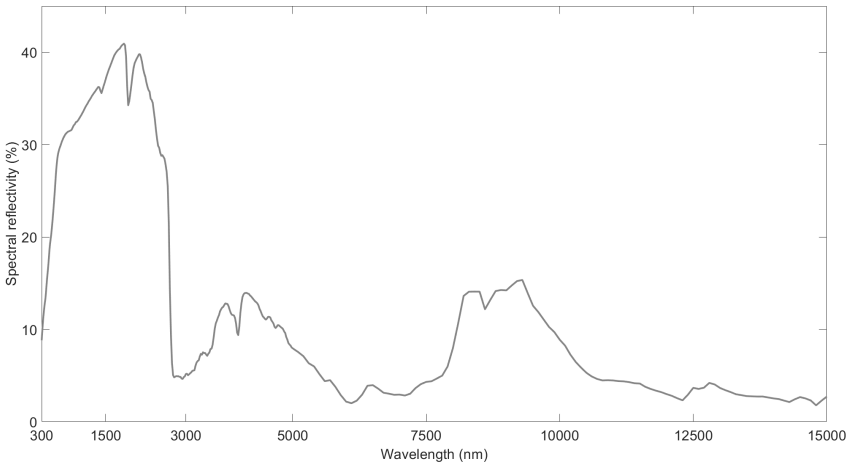

Figure B.1: Spectral reflectivity in (%) vs the wavelength (nm) for concrete

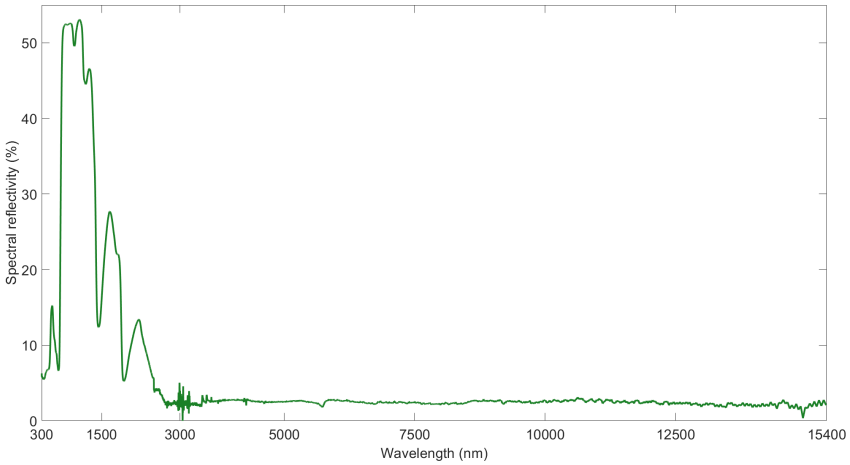

Figure B.2: Spectral reflectivity in (%) vs the wavelength (nm) for *pinus strobus*

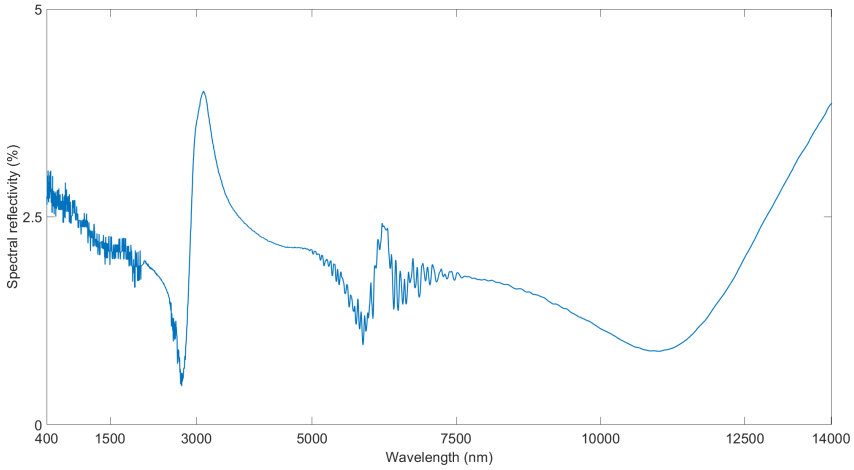

Figure B.3: Spectral reflectivity in (%) vs the wavelength (nm) for tap water

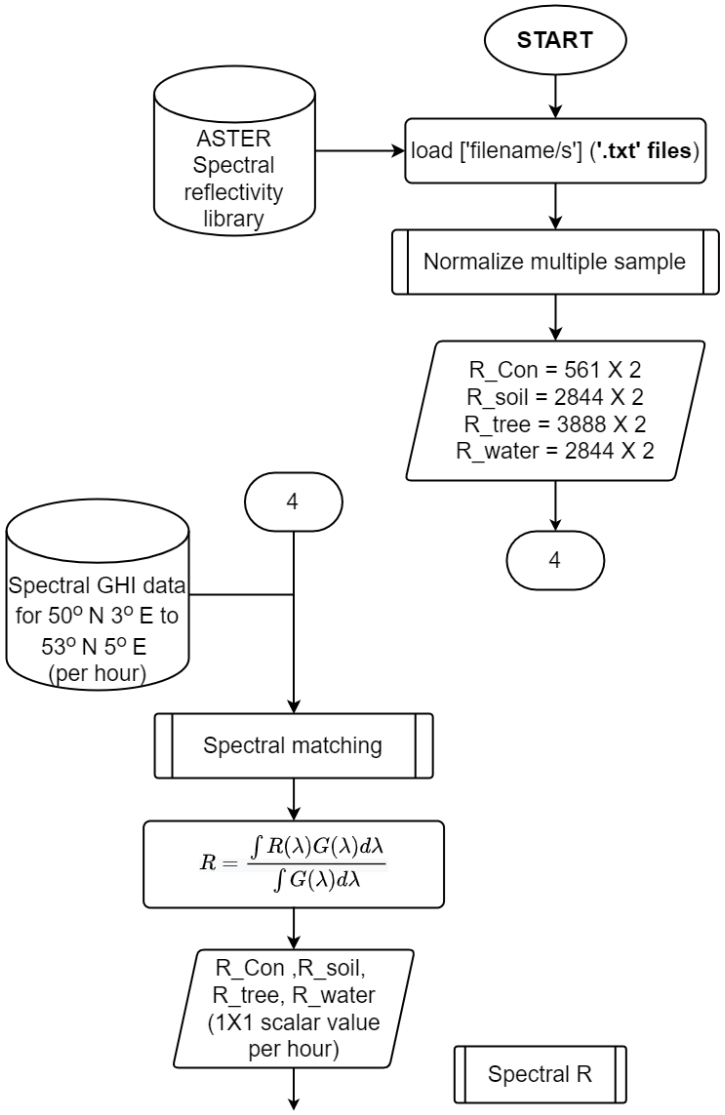

Figure B.4: Reflectivity data acquisition

C

Meteorological Data

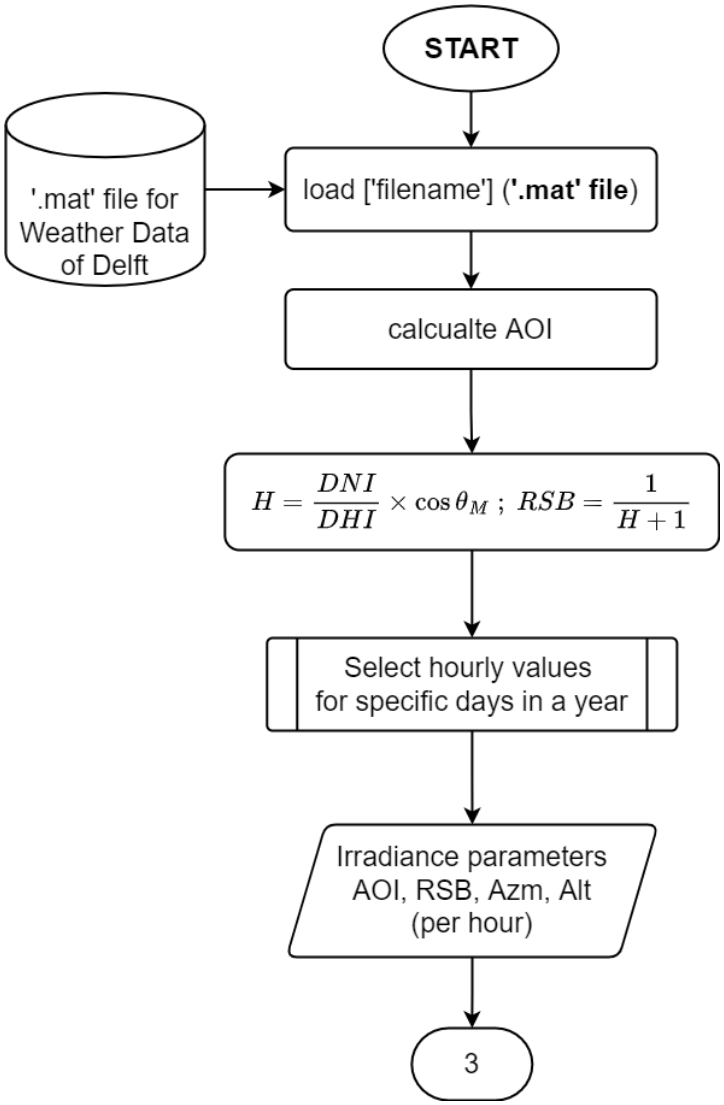

Figure C.1: Irradiation data acquisition

D

Albedo Calculation and Results

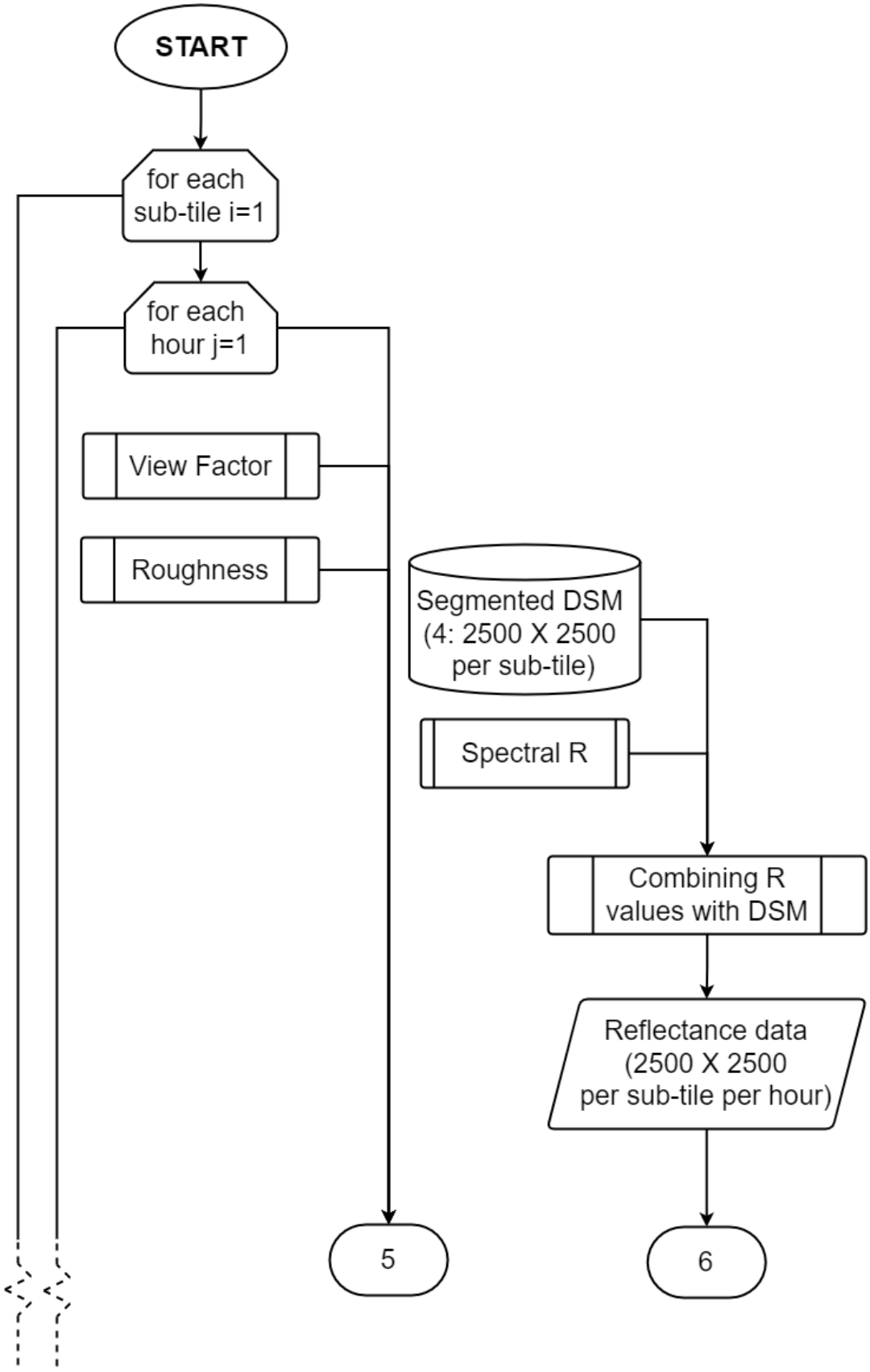

Figure D.1: Flowchart for Albedo calculation (page 1)

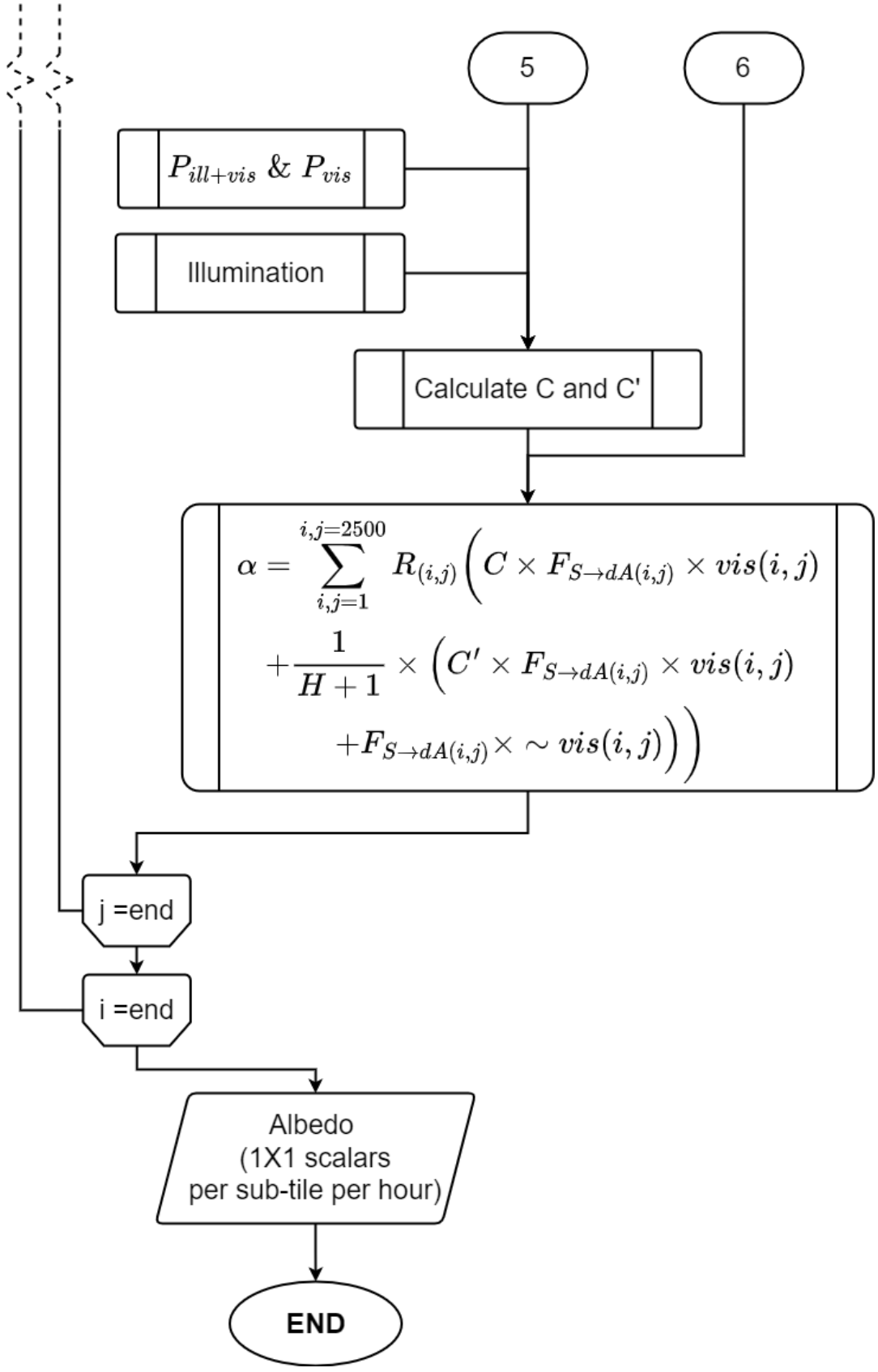

Figure D.2: Flowchart for Albedo calculation (page 2)

Sub-tile	AHN1	AHN2	AHN3	AHN4
1	0.256	0.106	0.113	0.134
2	0.257	0.103	0.115	0.121
3	0.267	0.11	0.106	0.115
4	0.267	0.1	0.113	0.128
5	0.269	0.122	0.132	0.146
6	0.258	0.1	0.115	0.123
7	0.264	0.108	0.133	0.142
8	0.264	0.089	0.109	0.127
9	0.264	0.09	0.091	0.104
10	0.266	0.096	0.088	0.1
11	0.255	0.138	0.147	0.147
12	0.254	0.131	0.134	0.139
13	0.254	0.135	0.147	0.151
14	0.248	0.154	0.16	0.161
15	0.257	0.133	0.144	0.141
16	0.257	0.106	0.118	0.111
17	0.251	0.147	0.158	0.154
18	0.253	0.124	0.138	0.137
19	0.246	0.136	0.15	0.148
20	0.257	0.14	0.149	0.151
21	0.253	0.125	0.136	0.138
22	0.25	0.146	0.155	0.154
23	0.253	0.134	0.146	0.144
24	0.25	0.138	0.144	0.14
25	0.26	0.095	0.112	0.118
26	0.265	0.077	0.087	0.086
27	0.264	0.078	0.089	0.086
28	0.26	0.113	0.136	0.144
29	0.266	0.109	0.119	0.122
30	0.262	0.12	0.134	0.127
31	0.26	0.142	0.158	0.165
32	0.267	0.124	0.131	0.13
33	0.267	0.086	0.101	0.12
34	0.269	0.114	0.132	0.128
35	0.267	0.124	0.135	0.134
36	0.261	0.114	0.126	0.126
37	0.258	0.139	0.151	0.15
38	0.264	0.09	0.117	0.115
39	0.268	0.132	0.139	0.157
40	0.269	0.136	0.136	0.152

Table D.1: Average yearly albedo values for every sub-tile and every AHN dataset

Sub-tile	AHN1	AHN2	AHN3	AHN4
1	0.258	12.641	11.017	11.112
2	0.263	16.244	15.236	10.844
3	0.096	8.712	14.394	8.956
4	0.098	6.373	5.681	4.247
5	0.054	3.979	3.772	3.026
6	0.286	14.628	13.122	13.273
7	0.144	9.074	6.079	6.883
8	0.164	8.496	8.57	7.365

Sub-tile	AHN1	AHN2	AHN3	AHN4
9	0.171	10.652	16.205	10.947
10	0.129	8.118	12.403	10.312
11	0.247	15.206	11.375	13.057
12	0.264	13.828	11.147	10.685
13	0.274	17.03	13.427	14.042
14	0.33	18.394	16.534	16.246
15	0.24	13.118	10.661	11.109
16	0.246	11.64	10.061	10.54
17	0.292	15.692	11.769	13.296
18	0.261	14.743	10.629	12.125
19	0.347	19.259	15.108	18.059
20	0.247	13.785	11.817	11.445
21	0.297	18.428	15.763	15.413
22	0.275	18.123	15.456	15.532
23	0.284	17.293	12.321	14.819
24	0.296	17.807	13.923	15.211
25	0.188	13.318	12.959	13.437
26	0.177	17.665	16.015	14.108
27	0.148	12.883	11.738	11.632
28	0.172	9.728	8.189	8.56
29	0.134	9.688	8.004	8.313
30	0.145	10.62	9.192	10.48
31	0.212	23.115	22.155	21.541
32	0.102	8.833	8.737	7.982
33	0.054	9.11	7.785	4.936
34	0.076	5.59	5.025	4.865
35	0.099	8.041	6.891	5.717
36	0.188	12.203	11.682	11.218
37	0.185	10.523	8.493	8.786
38	0.119	8.944	7.034	6.788
39	0.055	3.817	3.722	2.645
40	0.055	3.637	4.173	2.865

Table D.2: Roughness 'r' values for every sub-tile and every AHN dataset

Sub-tile	AHN1	AHN2	AHN3	AHN4
1	0.255	0.08	0.085	0.098
2	0.255	0.076	0.085	0.091
3	0.266	0.088	0.081	0.091
4	0.264	0.087	0.098	0.115
5	0.268	0.112	0.12	0.135
6	0.256	0.073	0.084	0.089
7	0.263	0.083	0.106	0.109
8	0.264	0.075	0.086	0.1
9	0.263	0.072	0.068	0.081
10	0.265	0.079	0.068	0.078
11	0.251	0.1	0.109	0.108
12	0.25	0.094	0.098	0.102
13	0.251	0.096	0.106	0.109
14	0.24	0.112	0.116	0.118
15	0.255	0.097	0.107	0.104
16	0.255	0.08	0.09	0.084

Sub-tile	AHN1	AHN2	AHN3	AHN4
17	0.246	0.105	0.116	0.112
18	0.25	0.088	0.101	0.1
19	0.24	0.098	0.109	0.107
20	0.255	0.102	0.11	0.111
21	0.249	0.091	0.099	0.101
22	0.245	0.107	0.113	0.113
23	0.249	0.095	0.106	0.104
24	0.245	0.099	0.105	0.102
25	0.259	0.069	0.082	0.085
26	0.264	0.06	0.067	0.068
27	0.263	0.062	0.07	0.069
28	0.258	0.084	0.103	0.109
29	0.266	0.082	0.091	0.093
30	0.26	0.091	0.102	0.097
31	0.258	0.106	0.116	0.121
32	0.266	0.098	0.102	0.1
33	0.266	0.074	0.085	0.105
34	0.268	0.098	0.111	0.111
35	0.266	0.099	0.108	0.11
36	0.26	0.086	0.095	0.094
37	0.255	0.102	0.113	0.112
38	0.263	0.075	0.094	0.095
39	0.267	0.118	0.124	0.146
40	0.268	0.122	0.118	0.14

Table D.3: Average yearly irradiance weighted albedo for every sub-tile and every AHN dataset